Lifetime and Efficiency of Blue Phosphorescent Organic Light-Emitting Diodes

by

Jae Sang Lee

A dissertation submitted in partial fulfillment
of the requirements for the degree of
Doctor of Philosophy
(Electrical and Computer Engineering)
in the University of Michigan
2017

Doctoral Committee:

Professor Stephen R. Forrest, Chair
Professor Pallab K. Bhattacharya
Professor L. Jay Guo
Associate Professor Max Shtein

Jae Sang Lee

jsanglee@umich.edu

ORCID iD: 0000-0003-1167-1398

ACKNOWLEDGEMENTS

I owe thanks to many people: this thesis that would have not been possible without their support. First of all, I should acknowledge my advisor, Professor Stephen Forrest. Over the past five years, he challenged my thinking and played a significant role in shaping me as a "Ph.D. student." I was deeply inspired by his endeavor to such high quality scientific work and profound understanding in science. He also taught me a life lesson to love what I am doing and to challenge for big things while not falling into the confirmation bias. I appreciate his education and patience with me, which completely changed my attitude towards work, as well as a life. Thank you very much.

Secondly, I acknowledge my mentors, Yifan Zhang and Michael Slootsky, who helped me to learn the basic experimental setup and data analysis skills, especially, that of blue OLEDs Yifan offered to work with me on what became the foundation of my thesis. Kyusang Lee provided me a critical solution to my first project and offered me an opportunity to learn the ray-tracing simulation. Caleb Coburn is with whom I always discussed physics of OLEDs; he also helped me with device modeling. I appreciate Changyeong Jeong who endeavored to assist me in making the best, long-lived OLEDs for my final project. Eva Ruff provided me with administrative support so that I could concentrate on research without any difficulties, and her career advice motivated me to work hard and to pursue the degree. I also enjoyed working with and spending time on group discussion, sports and many enjoyable parties with OCM group members including Cedric Rolin, Jeramy Zimmerman, Olga Griffith, Greg McGraw, Brian

Lassiter, Kyle Renshaw, Xiaoran Tong, Xin Xiao, Anurag Panda, Xiao Liu, Xiaozhou Che, Yue Qu, Dejiu Fan, Quinn Burligame, Jongchan Kim, Joosung Moon, Byungjun Lee, Kan Ding, Boning Qu, Charles Filipiak and many others that I forgot to mention.

In addition, I acknowledge Professor Mark Thompson and his group members at the University of Southern California who I worked with on multiple projects. Specifically, Hsiao-Fan Chen and Thilini Batagoda synthesized and provided me with deep-blue emitting materials that made most parts of my thesis possible. Also, Drs. Julie Brown and Mike Hack at Universal Display Corporation constantly offered me their best quality materials so I could make a progress in my projects. I thank Profs. Pallab Bhattacharya, L. Jay Guo and Max Shtein for serving on my graduation committee.

Last, but not least, I thank my parents for their love, care, and sacrifices. Also, I thank my Sister's family who welcomed me into their home during the holidays so I could feel at home. Without support from my family, this thesis certainly would not exist and therefore, my thesis is dedicated to them.

Jae Sang Lee

Ann Arbor

January, 2017

TABLE OF CONTENTS

LIST OF FIGURES

LIST OF TABLES

LIST OF APPENDICES

ABSTRACT

Organic light-emitting diodes (OLEDs) are poised to realize high performance for innovative display and lighting applications in the future. However, the development of suitable blue OLEDs remains a challenge which has impeded the progress of large-scale OLED commercialization for more than a decade. Blue devices are critical components for red-green-blue displays and white lighting, but to date suffer from short operational lifetimes as well as a lack of efficient deep blue emitting materials. This thesis aims at understanding the physical background of these issues and providing potential solutions.

OLEDs produce photons via radiative recombination of electron-hole bound pairs, called excitons. Fluorescent OLEDs depend on emission from the singlet excitons achieving an electron-to-light conversion, or internal quantum efficiency (IQE), from 25% up to 62.5%. On the other hand, phosphorescent OLEDs (PHOLEDs) exploit the emission from triplet excitons, attaining nearly 100% IQE. In OLED-based products, red and green PHOLEDs are universally used due to their high efficiency and long operational lifetime, while fluorescent OLEDs are still used for the blue emitting component despite their low performance. Thus, the development of long-lived and high efficiency blue PHOLEDs is a key to the success of the technology.

In the first part of this thesis, we investigate the nonradiative loss mechanism dominant in deep blue emitting phosphorescent materials. We identify the metal-centered ligand-field states (^{3}MC states) as a major source of efficiency loss and a probability of thermal population to these states increases with the emission energy of the emitter. Thus, we develop tris-cyclometalated

Iridium (III) complexes using N-heterocyclic carbene (NHC) ligands that render the energy of the ^{3}MC states inaccessibly high while keeping a wide energy gap for deep blue emission. The NHC-ligand based Ir(III) complex can thereby minimize the nonradiative loss and achieve high IQE in deep blue. In PHOLEDs, the NHC-Ir(III) complexes are used as the emitters, as well as hole transporting and electron blocking components. This multiple use enables a very high brightness operation of deep blue PHOLEDs, potentially suitable for demanding display applications.

In the second part of this thesis, we focus on understanding and solving the short lifetime of blue PHOLEDs. We identify the intrinsic mechanism of the device degradation is the bimolecular annihilation between the excited states in the emission layer (EML) that generates the energetically "hot" excited state. If such a hot excited state dissipates its energy on the EML molecule, the resulting chemical bond dissociation and its products permanently deteriorate device performance. The frequency of this failure process increases with the energy of the excited state, particularly severe in blue PHOLEDs compared to red and green emitting devices. Thus, we propose two solutions to this problem: (i) reducing the probability of the bimolecular annihilation via distributing the excited state density and (ii) bypassing the dissociative reaction via thermalizing the hot excited states on the ancillary dopant in the PHOLED EML. The stability of the blue PHOLED employing both strategies is cumulatively improved and a theory is proposed to explain such lifetime enhancement.

Chapter 1 Past, present and future of OLEDs

The most distinctive advantage of organic semiconductors may be tunability of their optical and electrical properties that can be suited to a wide range of practical applications, such as light emitting devices, photovoltaic cells, and field-effect transistors. Among these applications, organic light emitting diodes (OLED) have been the most widespread and successful organic semiconductor-based electronics and will be the main topic throughout this dissertation. In this chapter, we introduce a basic property of organic semiconductors and define important terminologies that are frequently used in this dissertation. Then, a brief history and the basic working principles of OLEDs will be discussed. Future applications enabled by OLEDs will follow.

1.1. Basic properties and definitions in organic semiconductors

Organic semiconductors generally refer to the pi-bonded molecular or polymeric semiconductors whose building blocks are composed of carbon and hydrogen atoms. While this definition applies to a general class of the organic semiconductors, their composition can also include heteroatoms such as nitrogen, oxygen, sulfur and some transition metals such as iridium (III) and platinum (IV). The combination of these atomic constituents determines the property of the comprising molecule that can obtain high absorption, efficient luminescence, and/or high mobility characteristics suited to organic photovoltaics (OPVs) [1], OLEDs [2] and/or organic

FET (OFET) [3]. **Figure 1.1** shows examples of the standard small molecules and their corresponding applications.

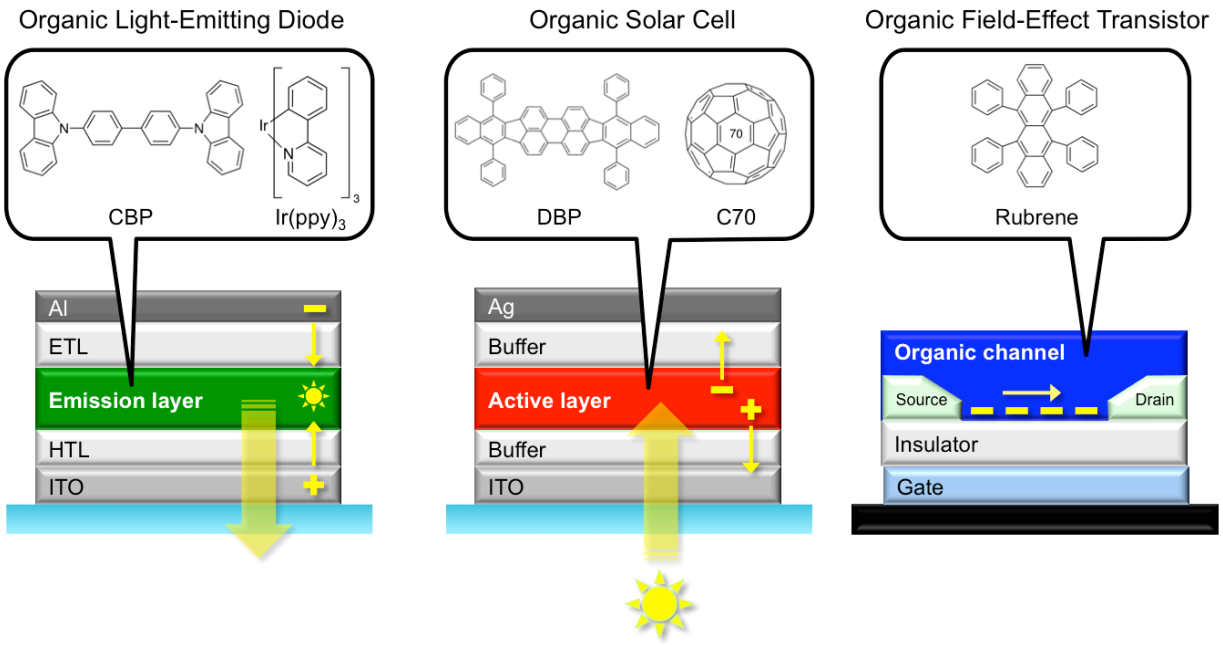

Figure 1.1 Examples of represantative small molecules used in organic optoelectronic devices. (a) organic light-emitting diodes (OLEDs), (b) organic photovoltaics (OPVs), and (c) organic field-effect transistors (OFETs). Here, CBP and Ir(*ppy*)$_3$ are used as the host and the light emitting dopant, respectively, in the emission layer of OLEDs. DBP and C70 are used as the donor and the acceptor, respectively, in the active layer of OPVs. The Rubrene crystal is used as the semiconducting channel for OFETs. Note that C70 does not fall into a category of organic semiconductors defined in the text, since C70 consists only of carbon atoms.

Fundamental characteristics of organic semiconductors can be understood by comparison with conventional inorganic semiconductors. We should first discuss the basic building blocks and the structures of both types, which play a critical role in determining their distinctive band structures and optoelectronic characteristics. The crystalline inorganic semiconductor has a highly ordered structure with a well-defined lattice whose constituent basis is the one or a few

atoms such as Si, Ge and GaAs. These atoms are held together by a strong covalent bond and thus, inorganic semiconductors are generally hard, brittle, and have a high melting temperature [4] (>1,000^{o}C), with a few exceptions such as HgCdTe [5]. On the other hand, the basis of the organic semiconductor is rather a large and electrically neutral molecule. In the bulk, these molecules are bound by the electrostatic van der Waals (vdW) force that is based on weak induced dipole–induced dipole interactions [6]. The weak vdW intermolecular interaction results in rather a random or amorphous arrangement of the organic molecules in most cases, although ordered structures can be found in some molecular crystals [7]. Therefore, organic semiconductors are generally soft, light and have a low melting temperature (<300^{o}C).

The electrical properties of semiconductors such as electronic band structure and charge conduction are mainly determined by interactions of their building blocks. In crystalline inorganic semiconductors, a periodic potential is created across the highly ordered lattice comprised of the covalently or ionic–bonded atoms. Thus, by plugging the wave function for the electron based on the Bloch's theorem and the periodic potential as a perturbation term into Schrodinger's equation, the band structure of the semiconductor (i.e. an E–k dispersion relationship) can be derived [4]. In the semiconductor band structure there exists an energetically forbidden zone (i.e. referred to as the band gap, E_g) between the continuous bands of the available electronic states, or a density of states (DOS), with the width of >4 eV [8]. The electronic state continuum below the band gap is called a valence band and the one above the band gap is referred to as the conduction band as shown in **Figure 1.2**. Since the Fermi level in intrinsic semiconductors lies in the band gap, the valence bands are, in general, filled with electrons whereas the conduction bands are partly filled or vacant of electrons depending on the temperature. When the electronic states in the conduction band are occupied by the electrons

from the filled states in the valence band via electrical, optical or thermal excitation, the semiconductor can conduct electrical current.

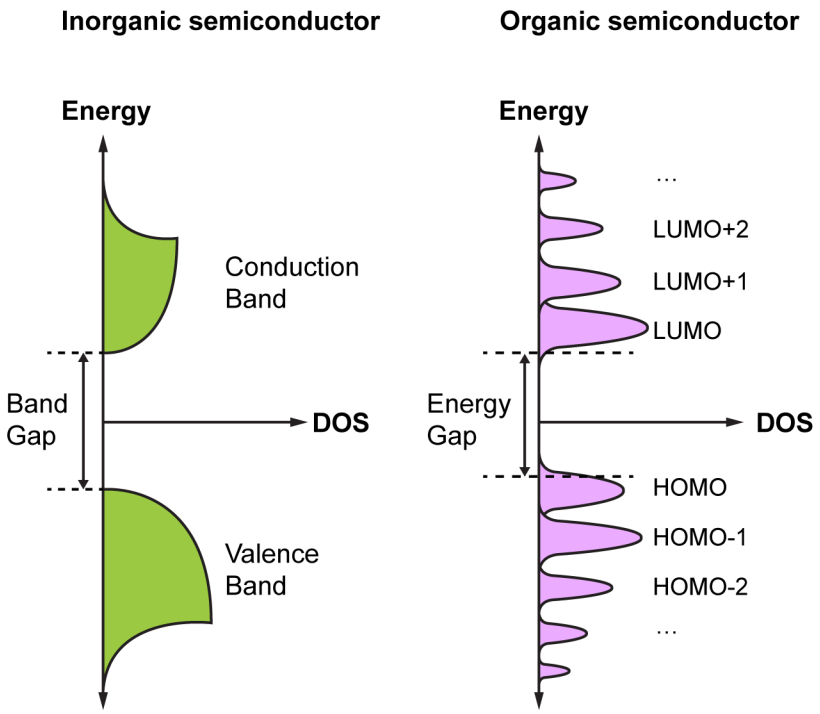

Figure 1.2 Density of states (DOS) diagram of inorganic and organic semiconductors. The energy gap in the organic semiconductor is vaguely defined due to tail states of the highest occupied molecular orbital (HOMO) and the lowest unoccupied molecular orbital (LUMO). The DOS of HOMOs and LUMOs follows the Gaussian distribution. Note that to analytically estimate the tail states, an exponential DOS can be assumed.

On the other hand, organic semiconductors consist of randomly oriented molecules loosely bound by a relatively weak vdW force. Thus, the band theory developed for crystalline semiconductors cannot be explicitly applied to the organic counterparts due to their random energetic nature. Instead of forming a continuous band, the available electronic states of organic semiconductors exist as discrete orbitals with a relatively narrow bandwidth of ≤100 meV (see **Fig. 1.2**). This energetic distribution is determined by the collective polarization effects among

randomly oriented molecules. The molecules in the solid or liquid phase are polarized by the surrounding molecules, and the vdW-based energetic interaction scales with $1/r^6$, where r is the intermolecular distance [9]. Since r is random in the amorphous organic semiconductor, the density of the molecular orbitals is assumed to follow a Gaussian distribution.

Among the orbitals filled with the electrons, the one that has the highest energy is called the highest occupied molecular orbital (HOMO), corresponding to the valence band edge (E_v) of inorganic semiconductors. Likewise, the one that has the lowest energy among the empty orbitals is called the lowest unoccupied molecular orbital (LUMO), corresponding to the conduction band edge (E_c) of the inorganic counterpart. The orbitals below the HOMO and above the LUMO are denoted as HOMO-1, HOMO-2,... and LUMO+1, LUMO+2,..., respectively, in energetic order. The frontier molecular orbitals of organic semiconductors refer to both the HOMO and LUMO and a forbidden zone, vacant of the available electronic states between the frontier orbitals, is defined as an energy gap (c.f. a band gap for the inorganic semiconductor). The frontier orbitals play a major role in determining the optical and electrical properties of an organic semiconductor such as absorption and emission as well as charge transport, similar to the conduction and valence band edges of the inorganic counterpart.

Due to the weak electronic coupling between molecules, charge carrier transport in amorphous organic semiconductors is limited by incoherent and phonon-assisted hopping between molecules with a mobility of $\mu << 0.1$ cm^2/Vs [10]. This is compared with the mobility of an inorganic semiconductor (e.g. $\mu > 1{,}000$ cm^2/Vs for the electron in the Si) characterized by the coherent band transport as described in **Fig. 1.3**. In some highly ordered and defect-free molecular crystals, however, the band transport characteristics are limited to $\mu \sim 0.1$–1 cm^2/Vs [11]. At room temperature, the intrinsic carrier concentration in the organic semiconductor, or

the density of thermally generated free charges given as $n_i \propto \exp\left(-E_g/2kT\right)$, is nearly negligible due to its wide energy gap of E_g = 3–5 (eV), as opposed to that of inorganic semiconductors of E_g = 1–2 (eV) (e.g. Si or GaAs have E_g = 1.11 and 1.43 (eV), respectively). Accordingly, organic semiconductors are intrinsically insulators and their charge conduction relies on injected charges from the electrodes or by an intentional conductive doping. The insulating nature of organic semiconductors with extremely low charge carrier mobility is the main reason state-of-the-art organic optoelectronic devices, including OLEDs, are based on a thin-film structure (<1 um) to eliminate the need of very large operating voltages, as well as to facilitate charge transport.

When an electron is added to or removed from the neutral molecule either by charge injection or exciton dissociation, it becomes an anion or cation, respectively. This *charged* molecule undergoes not only a geometric shape change due to redistribution of the comprising electrons, but also affects the intermolecular distance to the surrounding molecules due to the change in its polarization. The charged molecule along with this resultant "lattice distortion" is deemed a quantum quasi-particle called a polaron. Throughout this dissertation, holes and electrons in OLEDs actually refer to hole polarons and electron polarons, respectively, and charge transport, in most cases, refers to intermolecular polaron hopping (see **§2.2.1**).

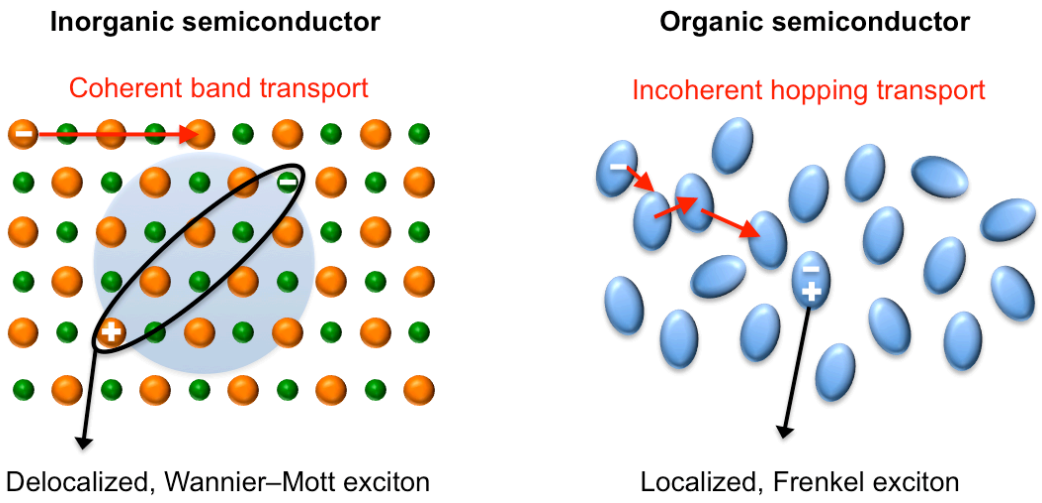

Figure 1.3 Structures of inorganic and organic semiconductors. Types of excitons and charge transport mechanisms are described.

The distinctive optical characteristics of organic semiconductors arise from its low dielectric constant of $\varepsilon_r \sim 3$, as opposed to that of inorganic analogs where $\varepsilon_r \sim 11$. As organic semiconductors absorb light of an energy equal to or larger than their energy gaps, the electron in the HOMO is promoted to the LUMO or higher energy orbitals, leaving a hole in the HOMO. Then, these electrons and holes are strongly attracted to one another by Coulomb force due to the weak dielectric screening with a binding energy of $E_{BE} = e^2 \big/ 4\pi\varepsilon_r\varepsilon_0 \left(a_0^*\right)^2 = 0.1 - 1$ (eV) [12]. Here, e is the elementary charge, ε_0 is the vacuum permittivity, and a_0^* is the effective Bohr radius of the exciton. Thus, this strongly bound electron-hole pair tends to be localized on a single molecule which is called a Frenkel exciton. This is in contrast to a Wannier-Mott exciton of inorganic semiconductors which is loosely bound by a weak $E_{BE} << 0.1$ eV due to large ε_r and therefore is delocalized across the lattice (see **Fig. 1.3**). In general, Wannier-Mott excitons are observed at very low temperatures in inorganic semiconductors [13] with a few exceptions such as GaN [14]. Frenkel excitons, or simply referred to as excitons hereafter, can be transferred

between molecular sites during their natural lifetime or before they are dissociated at a heterointerface (see **§2.2.7**). The excitonic energy transfer process dictates the performance of organic optoelectronic devices including OLEDs and OPV. The more details about the excitons will be discussed in **Chapter 2**.

Since the organic semiconductor is a low dielectric medium, it has a correspondingly low refractive index of n = 1.8 ~ 2.0 following the relationship $n \cong \sqrt{\varepsilon_r}$ at optical frequencies, compared to that of inorganic semiconductors where n > 3.0. Ref. [15] provides an overview of theories relating the energy gap *vs*. the refractive index which, roughly speaking, have an inverse relationship with each other. Therefore, light produced within OLEDs, for example, can be more efficiently extracted through a glass substrate (n ~ 1.5) to air (n ~ 1), compared to inorganic light emitting diodes made up of high refractive index materials. Combined with the large energy gap characteristics, highly efficient and transparent OLEDs can be realized (see **§1.4**).

The amorphous characteristics of organic semiconductors is advantageous in choosing substrates. Unlike inorganic semiconductors such as Si or GaAs that require lattice-matched, brittle and bulky substrates, organic semiconductors can be grown on any medium as long as the surface is atomically smooth (i.e. an average surface roughness < 1–2 nm). Combined with its small Young's modulus (10–20 GPa [16, p. 3] vs. 130–180 GPa for a silicon single crystal [17]), relatively soft organic semiconductors grown on the highly elastic substrates can enable flexible, curved, or stretchable electronics (see **§1.4**).

1.2. Growth technology of organic semiconductors

The growth technology of organic semiconductors is mainly determined by their material types. The amorphous molecular thin films, mainly used in OLED or OPV applications, are deposited by vacuum thermal evaporation (VTE). In the vacuum chamber, the powder of organic molecules is loaded in and heated by the resistive thermal crucible at the sublimation temperature, which then undergoes a transition from a solid either directly or via the liquid to gas phase. The pressure of the chamber is maintained low enough ($<10^{-6}$ Torr) so that the vapor of the sublimed molecules travels a long mean free path straight toward the target without colliding into the background gaseous molecules. Subsequently, the vaporized organic molecules that reach the cooled target are condensed into a solid, i.e. the deposition process, forming the thin film. The sublimable organic molecules, generally referred to as small molecules, consist of thermally stable, small and rigid molecular moieties. All the organic materials used in the OLEDs of this dissertation are small molecules deposited by VTE. On the other hand, a polymer is a large molecule that consists of many repeating units and side chains. Due to the weak bond nature of polymers, these materials in general cannot be processed by thermal evaporation. Therefore, most polymers are dissolved in solutions to disentangle the complex units [18] and subsequently are deposited using spin-coating.

While VTE has been widely adopted in large-scale OLED manufacturing, the major drawback of this process is low material utilization efficiency. To overcome this issue, organic vapor phase deposition (OVPD) has been proposed as an alternative to the VTE [19].

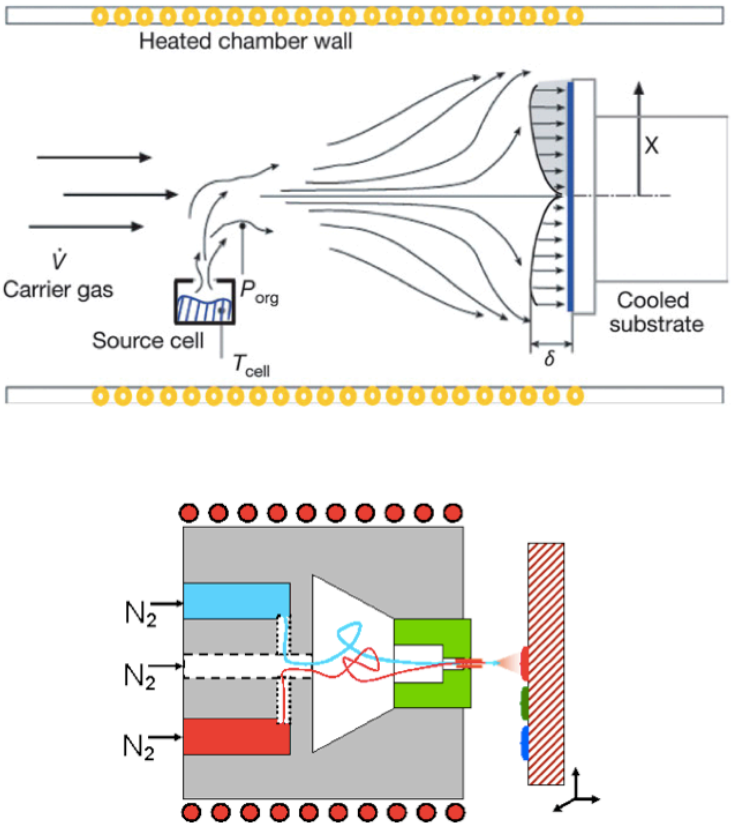

Figure 1.4 Schematic of organic vapor phase deposition and organic vapor jet printing. Images are obtained from Ref. [20] and Princeton University, respectively.

As shown in **Figure 1.4**, OVPD uses an inert carrier gas such as nitrogen or argon to transport vaporized organic molecules to the cooled substrate, where they are condensed into a thin film. The pressure inside the OVPD chamber is maintained at 0.1 – 10 torr and the wall of the chamber is heated at a higher temperature than that of the source crucible at the sublimation temperature to prevent undesirable condensation or re-evaporation of the materials on the wall. Thus, OVPD can achieve high material utilization efficiency. The interesting feature of OVPD is that it can control the morphology of molecular thin films by varying growth conditions such as gas pressure. Based on this approach, OVPD-grown, ultra thick poly-crystalline layers are used as an active layer of OPVs, enabling high efficiency and long lifetime [21], [22]. Also, OVPD-

grown OLEDs showed comparable performance relative to that of VTE-grown counterparts [23]. These examples show the potential of OVPD as large-scale manufacturing process technology of organic optoelectronic devices.

Since conventional lithographic technologies are damaging to organic materials, both OVPD and VTE require shadow masks to define the shape and size of the organic thin film devices. For patterning 30–50 μm sized features such as pixels in modern OLED displays, a fine metal mask (FMM) with a thickness of 30–200 um has been widely used. Although FMM is a conceptually simple technique, it is hard to scale up to the large-sized substrates due to sagging of the mask, is challenging to pattern the feature size below a few tens of microns due to shadowing effect, and causes a large waste of materials. Thus, organic vapor jet printing (OVJP) has been proposed as an alternative to overcome such problems [24]. The working principle of OVJP is similar to that of OVPD in that both techniques use the inert carrier gas to transport the organic vapor to the substrate. The main difference is that a jet of organic vapor is shot through a small-size nozzle in OVJP (<10 μm diameter, see **Fig. 1.3**), which enables small-area deposition dependant on gas pressure and distance of the nozzle to the substrate [25], [26]. Thus, both deposition and patterning are simultaneously performed by OVJP, potentially eliminating the need of the shadow mask. By using an array of multiple OVJP nozzles, a highly efficient and large-scale deposition process is possible.

1.3. A brief history of OLEDs

The electroluminescence in organic materials was first observed in 1963 by applying a direct current voltage of ~400 V to 10–20 μm thick anthracene and tetracene-doped anthracene crystals [27]. Then, the first organic electroluminescent device, or OLED, was demonstrated by Tang and VanSlyke in 1987 [2], which was operated at a practical operating voltage of 5–10 V by virtue of a thin film structure (the total thickness of ~1 μm). This first-generation OLED was comprised of small molecule-based hole-transport (HTL) and electron-transport layers (ETL), sandwiched between a semi-transparent indium-tin-oxide (ITO) anode and a reflective Mg:Ag cathode. Here, tris(8-hydroxyquinolinato)aluminum (Alq_3) served as the ETL, as well as the emissive layer (EML) where radiative recombination of the excitons mainly occurs as shown in **Figure 1.5**.

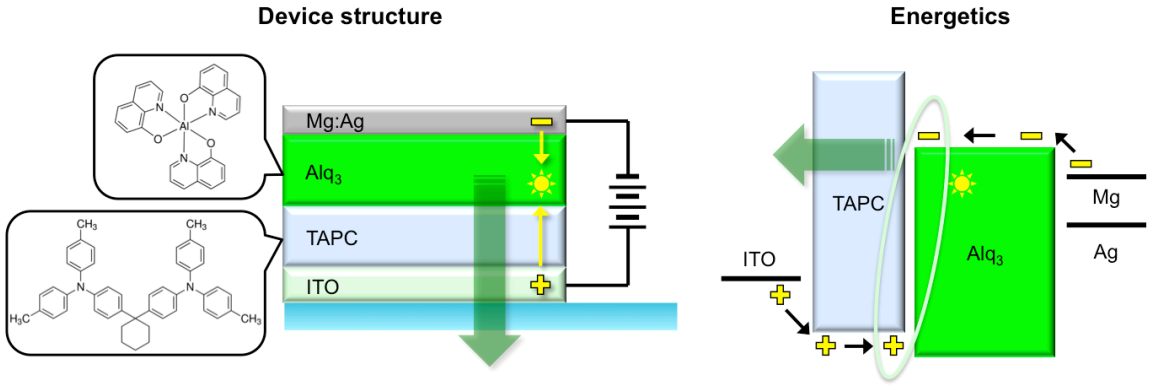

Figure 1.5 Device structure and energetics of the first generation OLED.

This multi-layered, green emitting OLED achieved a remarkably high external quantum efficiency (EQE) of ~1%. Soon after, Tang *et al*. demonstrated a doping technique by co-evaporating Alq_3 that was used as a host matrix and a small volume (<1 mole%) of the fluorescent dopant, either 4-(dicyanomethylene)-2-methyl-6-(4-dimethylaminostyryl)-4H-pyran

(DCM) or Coumarine 540 [28]. By allowing Förster energy transfer from Alq_3 to fluorescent dopant (see **§2.2.7**), this OLED exhibited emission from the dopant with a further boosted EQE of 2.5% compared to an undoped green emitting device. These advanced concepts incorporating multi-layered structures and color/efficiency control by the host-guest system have been widely adopted in state-of-the-art OLEDs.

In the EML, injected hole and electron polarons with random spin recombine to form two types of excitons, i.e. singlet and triplet excitons with a ratio of 1:3 based on their spin statistics [29] (see **§2.2.4**). The first generation OLED is referred to as a fluorescent OLED based on the radiative recombination of singlet excitons. Since only a quarter of the generated excitons (i.e. singlets) participates in the emission while the rest of the excitons (i.e. triplets) nonradiatively decay in the form of heat, the internal quantum efficiency is limited to IQE = 25% for the fluorescent OLEDs. In 1999, Baldo *et al*. [30] found a mechanism that utilizes the triplet excitons to luminescence by an efficient singlet-triplet mixing via enhanced spin orbit coupling in heavy metal-based, light-emitting organic complexes (see **§2.2.6**). Specifically, all the singlet excitons can rapidly intersystem cross to the triplet excitons and triplet excitons perturbed by, and thus, having the character of singlet excitons radiatively recombine on the organometallic complexes. The devices exploiting such a mechanism are called electrophosphorescent OLEDs (PHOLED). PHOLEDs can achieve 100% IQE by having all the generated excitons to participate in the emission [31]. Eventually, the development of the highly efficient PHOLEDs has been the seminal step towards commercialization of the OLED technology. The operating principle and design concept of phosphorescent emitters and devices will be discussed in greater detail in **Chapter 2**.

While red and green PHOLEDs are nearly universally used in commercial products due to their superior efficiency and long lifetime, the blue emitting component still relies on fluorescent OLEDs due to the lack of long-lived, high efficiency blue PHOLEDs. Recent blue fluorescent OLEDs can attain IQE up to the theoretical limit of 62.5%, by combining prompt and delayed fluorescence [32]. Prompt fluorescence arises from the radiative recombination of initially generated singlet excitons whose natural decay time is below a few tens of nanoseconds. On the other hand, delayed fluorescence arises from the singlet excitons additionally generated by annihilation between the long-lived triplet states whose natural decay time is several hundreds of microseconds. Therefore, the delayed fluorescence is a slower process that follows after prompt fluorescence.

The high efficiency of a modern fluorescent OLED is beneficial in reduction of its operating current level to obtain the desired luminance, thereby slowing down the device degradation process that generally scales with the density of the excited states [33]. Even so, the lifetime of recent blue fluorescent OLEDs is insufficiently short compared to the state-of-the-art red and green PHOLEDs. To overcome the efficiency limit of fluorescent devices, thermally assisted delayed fluorescence (TADF) OLEDs have been actively studied that can achieve an IQE up to 100% [34], comparable to PHOLEDs. This is enabled by efficient upconversion from the triplet to the singlet excitons by reducing the energy gap between these two states. Although high efficiency red, green and blue TADF OLEDs have been reported [35], [36], the lifetime of green TADF remains insufficiently low [37], and those of red and blue are even much less. The lifetime issue of OLEDs will be discussed in greater detail in **Chapter 5** and **Chapter 6**.

1.4. Success and innovation enabled by OLEDs

OLEDs enable high efficiency and attractive display and lighting applications. Advantages of the OLED as a screen light source such as high resolution, wide color gamut and low power consumption have been successfully demonstrated by their use in the displays of smart phones and televisions as shown in **Figure 1.6**.

Figure 1.6 Personal electronics enabled by OLED. Images of Samsung Galaxy smartphone, LG OLED television and Apple smart watch are included.

The distinctive advantage of OLED displays compared to liquid crystal displays (LCDs) is that the latter requires multiple components including the backlight unit (usually white light emitting diodes), two polarizers, as well as color filters to produce the desired color and luminance, while the former only need OLED sub-pixels. Thus, OLED displays that only require the OLED pixels and a TFT backplane can enable ultra-thin and light weight electronics. Since OLED pixels can produce a *deep black* color by turning off the devices while operating a certain portion of them only where the image is required, the OLED can not only reduce power consumption, but also attain a theoretically infinite contrast ratio (defined as the ratio of highest luminance to the lowest value). This is compared to the contrast ratio of the state-of-the-art LCD

of 1600:1, indicating that an OLED can produce a broader range between bright and dark conditions. Further, since the response speed of the OLED is very fast with turn–on and –off times of 1–2 μs [38], [39], OLEDs are suited to gaming or virtual/augmented reality applications and high-speed video contents without motion blur issue that LCD has typically suffered from due to its slow response times (several milliseconds) [40]. Also, the OLED is a Lambertian light source, indicating that the device luminance is invariant with viewing angle. Thus, the emission of optically optimized OLEDs has nearly negligible angle– and wavelength–dependence, enabling its adoption in the large-area television screens.

Figure 1.7 Future applications enabled by OLEDs. For example, virtual/augmented reality gears, transparent and flexible displays are shown. Images are obtained from Random42, Samsung, and Electronic Products.

OLED materials, typically having a small Young's modulus, can be deposited on flexible substrates to realize wearable or curved display electronics. For example, the OLED-based Apple smart watches and Samsung Galaxy smartphones have a partially curved portion of the screen near the side edges as shown in **Fig. 1.6**. Combined with the flexible and mechanically stable encapsulation barriers for the plastic-based devices, the rollable, free-form, and wearable displays have also been demonstrated (see **Fig. 1.7**). Finally, by utilizing the highly transparent characteristics of the organic molecules (i.e. negligible absorption coefficient in the visible),

OLEDs can be integrated with windows in the house, office and automobiles, or stand alone to be used as see-through and head-up displays. As such, the OLED is believed to open up a $20 billion market by 2020 by virtue of various innovative applications along with early success in personal electronics.

Chapter 2 Optoelectronic properties of OLED materials and devices

The performance of the OLED is determined by the properties of the comprising materials, and the electrical and optical processes that occur during device operation. In this chapter, we introduce the basic structure and operating principle of the OLED, as well as important metrics to evaluate the device performance. Then, we briefly review physics of the electrical and optical processes of the organic semiconductors that is relevant to the OLED operation. Finally, we discuss the design schemes and fundamental properties of blue phosphorescent organometallic complexes.

2.1. An introduction to OLEDs

2.1.1. Structure and operating principle of OLEDs

The standard structure of the OLED consists of several functional layers including the EML that are sandwiched between two electrodes, i.e. a semi-transparent ITO anode and reflective Al or Ag cathodes. The organic materials are chosen such that the energy differences from the work functions of the electrodes and are minimized. Thus, the need of high electric field to overcome the potential barrier for charges is eliminated, (see **§2.2.1**) and the electrical loss induced by the charge accumulation at the junctions between layers is reduced.

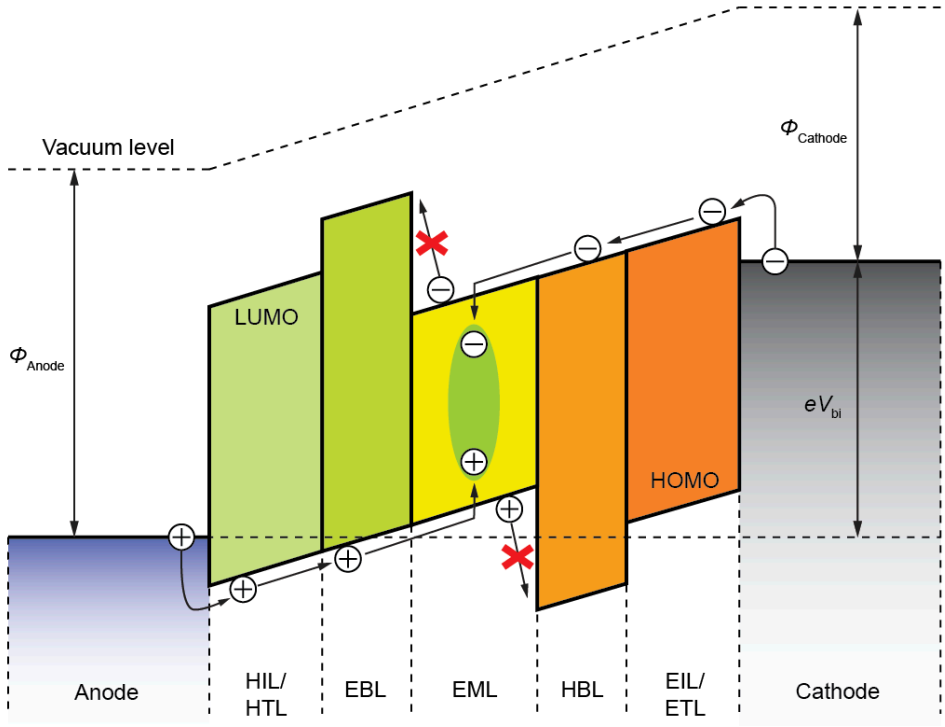

Figure 2.1 Device structure and energetics of the standard OLED. Here, Φ_{Anode} and $\Phi_{Cathode}$ are work functions of the anode and cathode, respectively, with respect to the vacuum level. $eV_{bi} = \Phi_{Anode} - \Phi_{Cathode}$ is the built-in potential of the diode.

Figure 2.1 shows the standard OLED structure and its energetics. The organic molecules deposited adjacent to the electrodes are called the hole injection (HIL) and electron injection layer (EIL) that are used for facilitating the charge injection into a stack of the organic layers. Subsequently, the injected charges are transported through the hole transport (HTL) and electron transport layers (ETL) towards the EML where they recombine to form the excitons. Since most organic materials including those used in the EML have asymmetric hole and electron mobilities, hole blocking (HBL) and electron blocking layers (EBL) are employed that confine charges within the EML by imposing the high potential barrier and thus stimulate exciton formation [41], [42]. To accomplish such functions, the HBL and EBL should have energetically more stable HOMO and shallow LUMO energies with respect to the vacuum level, respectively, compared to

that of the EML molecules. In addition, there are other important requirements for the blocking layers: (i) the HBL and EBL should efficiently conduct electrons and holes, respectively, while blocking the opposite charges, and (ii) should have at least equal or larger energy of the exciton states than that of the EML so that the excitons do not leak out of the EML. Above-mentioned requirements to achieve high-efficiency OLEDs are sometimes fulfilled by the single, multifunctional layer with the good charge injection and transport characteristics, as well as exciton and charge blocking capability [43].

The PHOLED EML generally employs a host–guest system where the phosphorescent emitter is doped into the host matrix at a concentration ranging from 2 to 20 vol%, depending on the device structure and the material characteristics. The host matrix should have at least equal or larger energy gap than that of the dopant to ensure exothermic energy transfer of the excitons from the host to the dopant (see **§2.2.7**) [44]. In order to attain the high luminescent quantum efficiency of the phosphorescent emitter in the host matrix, a low doping concentration (<2 vol %) is desirable to minimize the nonradiative loss induced by the concentration quenching [45]. However in most PHOLED EMLs the unipolar host materials preferentially conduct one type of the charge carriers while the opposite charges are trapped by or are transported via hopping between the phosphorescent dopants that are generally slower [2]. Thus, the dopant concentration of >5 vol % is required to ensure balanced charge transport in the EML and high efficiency [41]. To satisfy such conflicting conditions, a "co-host" EML structure has been demonstrated that mixes the hole-transport and electron-transport-type hosts for balanced charge transport [46]. Or, the host with bipolar charge transport characteristics has been employed [47]. For such systems, only a small concentration of the phosphorescent dopant (<2 vol %) is

sufficient for achieving very high efficiency [48]. A detailed discussion of the state-of-the-art structures for blue PHOLEDs will be given in **Chapter 4**.

2.1.2. Colorimetry

The normal human eye has three cone cells for sensing visible light, i.e. that differentiate the "chromaticity" and "luminance" (roughly accepted as brightness, see below for the definition) of the electromagnetic wave at a certain wavelength range between λ = 380 nm and 780 nm (i.e. the visible spectrum).

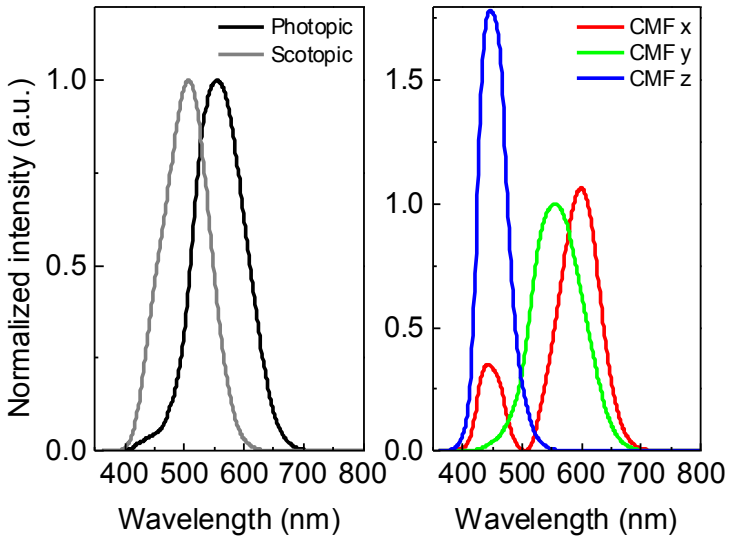

Figure 2.2 Luminosity function and CIE color matching functions. (a) Luminosity functions that represent a spectral sensitivity of human eye perception of the luminance under bright (photopic) and dark conditions (scotopic). (b) Color matching functions yielding CIE tristimulus values, *X*, *Y*, and *Z*.

The luminosity functions including the photopic and scotopic responses quantify the spectral sensitivity of the human eye to the luminance of the light under bright and dark conditions, respectively, as shown in **Figure 2.2**. The photopic response indicates that the light

within the green spectral regime (500–570 nm) is perceived brighter than red and blue colors with a peak at λ = 555 nm. However, under low light level typically during night time, the cone cells cannot perceive the light and instead, the rod cells become functional that have the high sensitivity near the greenish-blue region ($\lambda \sim$ 500 nm) and negligible sensitivity to red light ($\lambda >$ 600 nm).

Another factor determining color perception is the chromaticity. Commonly, the chromaticity of the light source detected by the spectral response of the three cone cells is quantified using the Commission Internationale de l'Eclairage (CIE) 1931 (x, y) chromaticity diagram. The x and y chromaticity coordinates are calculated using three CIE tristimulus values X, Y, and Z as

$$x = \frac{X}{X+Y+Z}, \quad y = \frac{Y}{X+Y+Z} \tag{2.1}$$

where Y is the luminance of the light source and the combination of X and Z contains all possible chromaticity information at luminance Y. X, Y, and Z can be calculated using the color matching functions (CMF) $\bar{x}, \bar{y}$ and $\bar{z}$ as

$$\begin{aligned} X &= \int_{380nm}^{780nm} I(\lambda)\bar{x}(\lambda)d\lambda, \\ Y &= \int_{380nm}^{780nm} I(\lambda)\bar{y}(\lambda)d\lambda, \\ Z &= \int_{380nm}^{780nm} I(\lambda)\bar{z}(\lambda)d\lambda. \end{aligned} \tag{2.2}$$

The CMF shown in **Fig. 2.2 (b)** represent the standardized spectral response of the three light cells yielding the tristimulus (i.e. X,Y, and Z) values. $I(\lambda)$ is the spectral radiance of the light source. The radiance is defined as the radiant power that is emitted by a surface within the unit solid angle per unit projected area (W sr^{-1} m^{-2}).

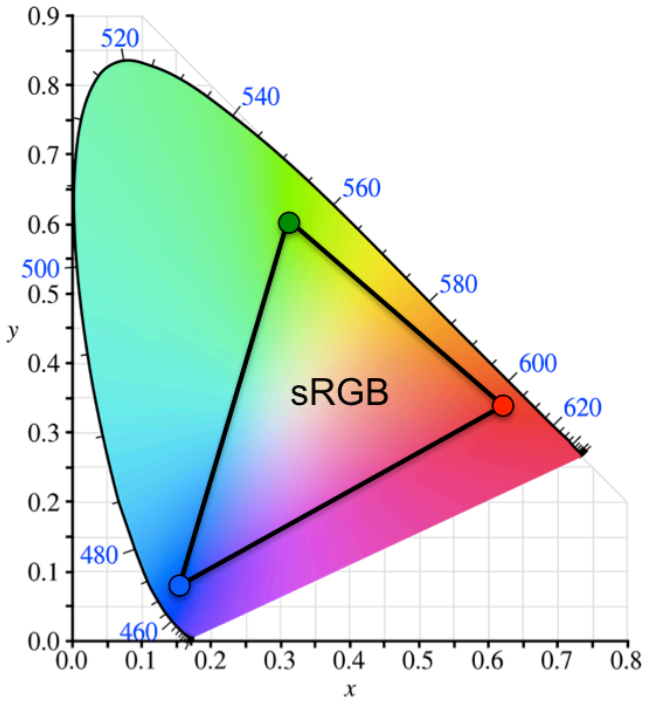

Figure 2.3 CIE 1931 *xy* chromaticity diagram. In the diagram, the standard red-green-blue (sRGB) color gamut is included.

Figure 2.3 shows the CIE 1931 color space diagram called the gamut of human vision, that collectively displays the chromatic information of the visible light by using the CIE (*x*, *y*) coordinates (**Eq. (2.1)**). The curved boundary represents monochromatic light, while the straight boundary is referred to as the line of purples. If three light sources with different chromaticity are mixed at a certain ratio, any chromaticity within the triangular gamut formed by their (*x, y*) coordinates can be produced. For example, **Figure 2.3** includes the standard RGB color space (sRGB) widely adopted in the screens of personal electronics. The triangular sRGB gamut is formed with the three vertices of the coordinates, (0.64, 0.33), (0.30, 0.60), and (0.15, 0.06), corresponding to primary red, green, and blue colors, respectively. In OLED-based displays, high performance red and green PHOLEDs whose colors are close to the required chromaticity

have been adopted, while the blue PHOLED counterpart is still under development. Thus, blue fluorescent OLEDs are used (see **§ 2.1.3** for the current technology status of the OLED).

2.1.3. Characterization of the OLED performance

The external quantum efficiency (EQE) of the OLED is an important metric for evaluating performance. The EQE is defined as the ratio of the number of extracted photons out of the device towards the viewer to the total number of injected electrons,

$$EQE = \frac{\#\text{ of extracted photons}}{\#\text{ of injected electrons}} = \frac{\#\text{ of generated photons}}{\#\text{ of injected electrons}} \cdot \frac{\#\text{ of extracted photons}}{\#\text{ of generated electrons}} \\ = \eta_{IQE} \cdot \eta_{IQE} = \left(\gamma_{CB} \cdot \chi_{ex} \cdot \eta_{QE}^{*}\right) \cdot \eta_{OC} \quad (2.3)$$

Here, η_{IQE} denotes the internal quantum efficiency (IQE), the ratio of the total number of generated photons within the OLED EML to that of the injected electrons, and is determined by the three factors (see below). η_{oc} is the outcoupling efficiency, the ratio of the extracted vs. generated photons. In general, most generated photons within the OLED EML are lost via optical coupling to the waveguide, substrate and surface plasmon modes [49]. For this reason, the outcoupling efficiency (η_{oc}), is typically limited to ~20 % without any light extraction techniques [49].

η_{IQE} is comprised of the charge balance factor, γ, the fraction of the radiative excitons, χ_{ex}, and the photoluminescence quantum yield, $\eta_{QE}{}^{*}$. γ in the modern OLED is near unity, because most injected charges are confined within the EML by the blocking layers (see **§2.1.1**) that subsequently participate in the exciton formation. Fluorescent OLEDs based on the singlet emission can attain χ_{ex} = 25 % considering the spin statistics of the singlet to triplet formation rate of 1:3 and the transition selection rule (see **§2.2.5**) [29]. However, some modern fluorescent OLEDs can obtain higher χ_{ex} by up to 62.5% [50] or even 100% [51] employing delayed

fluorescence by the triplet-triplet fusion or triplet-to-singlet upconversion, respectively, that manipulate the spin selection rule. χ_{ex} for the PHOLEDs is 100 %, because all the generated excitons including both triplets that are originally formed upon the electron-hole recombination (see **§2.2.4)** and that are transferred from the singlets via intersystem crossing, participate in radiative recombination, enabled by the strong spin-orbit coupling perturbation (see **§2.2.6**). η_{QE}^{*} = $k_r^* / k_r^* + k_{nr}$, where k_r^* and k_{nr} are the radiative and nonradiative decay rates of the excitons, respectively. Note that k_r^* is modulated by microcavity conditions created within the multi-layered device structure (i.e. via the Purcell effect) [49]. k_{nr} includes phonon-mediated nonradiative relaxation processes, as well as the efficiency loss mechanisms such as triplet-triplet (TTA) or triplet-polaron annihilation (TPA) that are dependent on the operation conditions (see **§2.2.7**). These annihilation processes are similar to Auger-recombination in conventional inorganic semiconductors in that the excited triplet state (donor) transfers its energy to the another excited state (acceptor) within an interaction radius, and nonradiatively relaxes to the ground state. The other states that gain extra energy via the annihilation become "hot" excited states that occupy higher energy electronic manifolds, most of which are rapidly thermalized to the lowest excited state. Both TTA and TPA in the PHOLEDs are responsible for the efficiency loss, especially at high brightness that requires a large density of the excitons and polarons [52]. Furthermore, it has been reported that hot excited states generated by the bimolecular annihilations are the main source of the molecular dissociation in the EML and the ensuing degradation of the operational lifetime of the PHOLED [33]. PHOLED lifetime related to TTA and TPA will be discussed in **Chapters 5** and **6**.

The important photometric quantities used in displays include the luminance and the current efficiency. For the lighting, the luminous efficacy as well as the luminance are generally

used. The luminance measures the luminous intensity per unit area of multipoint or area light sources with the SI unit of candela per square meter (cd/m^2). Here, the luminous intensity is a standard measure of the human eye response (i.e. a luminosity function, **Fig. 2.2 (a)**) to the power of wavelength-dependent light in a particular direction per unit solid angle. The strict definition of 1 cd is the unit luminous intensity of a light source emitting monochromatic radiation of frequency 540×10^{12} Hz that has a radiant intensity of 1/683 Watt per unit solid angle in a given direction.

Table 2.1 Luminance characteristics of sub-pixels in the commercial OLED product. Maximum screen luminance and pixel luminance of the red, green, and blue sub-pixels and their combination (i.e. white) are shown. Note that the cell brightness is attenuated by the polarizer and other display components.

Pixels	Max screen luminance (cd/m^2)	Max sub-pixel luminance (cd/m^2)
White	435	3,500
Red	110	3,300
Green	311	6,400
Blue	27	650

* Data presented by Prof. Ching W. Tang at the 11th International Conference of Electroluminescence and Optoelectronic Devices, Raleigh, North Carolina, USA (Oct, 2016).

Table 2.1 shows the maximum luminance of red, green and blue sub-pixels along with their mixture (i.e. white light) in a commercial OLED display. The typical luminance of a personal electronic display screen (e.g. laptop, computer monitor, and television) ranges from 100 to 500 cd/m^2, while the luminaire requires much higher luminance from >3,000 up to 10,000 cd/m^2, depending on the place and time of their usage.

The luminous efficacy is the ratio of the luminous flux to the consumed electrical power with units of lumens per Watt (lm/W). Here, the luminous flux is the total emitted luminous power of the light source with the unit of lm. That is, 1 lm (= 1 cd × 1 sr) is the flux of the light source uniformly emitting 1 cd of the luminous intensity in all directions within the unit solid angle of 1 steradian or sr. For example, if the OLED uniformly produces 1 cd of light in forward-viewing directions (i.e. a half-sphere), the luminous flux of the device becomes 6.3 lm (≈ 1 cd × 2π sr).

Table 2.2 Representative commercial PHOLED performance at L_0 = 1,000 cd/m^2

Color	CIE	Current efficiency (cd/A)	Operational lifetime (hr)	
			T95	T50
Deep red	(0.69, 0.31)	17	14,000	250,000
Red	(0.69, 0.34)	24	25,000	600,000
Red	(0.64, 0.36)	30	50,000	900,000
Green-Yellow	(0.46, 0.53)	72	70,000	1,400,000
Green	(0.34, 0.62)	78	18,000	400,000
Light blue	(0.18, 0.42)	47	600	20,000

Source: Universal Display Corporation (http://www.oled.com)

The recent OLED applications use the current efficiency, i.e. the luminous intensity per injected current to the device with the units of cd/A, as an indicator of the device performance. Including the operational lifetime, **Table 2.2** shows the figures-of-merit of commercial PHOLEDs as an example. Here, T95 indicates the elapsed time measured from the initial luminance of L_0 = 1,000 cd/m^2 to a reduction by 5% from its initial value under the constant current operation. T95 is typically quoted as the lifetime for display applications, because only 3–5 % reduction of the luminance can be readily recognized by the human eye. Thus, for the

practical use of personal electronics, T95 > 10,000 hr (i.e. approximately 10 years for the 2–3 hours use on a daily basis) for red, green and blue or white sub-pixels is required. **Table 2.2** shows that T95 of deep red, red, green-yellow and green PHOLEDs are well above the required lifetime standard. Interestingly, green-yellow or green PHOLEDs achieve greater current efficiency than that of other color devices. Assuming the PHOLEDs have similar EQE, the reason is a result that the human eye is most sensitive to the emission of wavelengths between 500 and 600 nm (see **Fig. 2.2**). Note that T95 of the light blue PHOLED is 600 hr with CIE of (0.18, 0.42), which is insufficiently short for the practical use. Deeper blue PHOLEDs that barely meet the display color standard, i.e. CIE of (0.15, 0.06), have even shorter lifetimes (see **Chapter 6**).

Table 2.3 Representative commercial fluorescent OLED performance at L_0 = 1,000 cd/m^2

Color	CIE	Current efficiency (cd/A)	Operational lifetime T50 (hr)
Red	(0.67, 0.33)	11	160,000
Green	(0.29, 0.64)	37	200,000
Blue	(0.14, 0.12)	9.9	11,000

Source: Idemitsu Kosan (http://www.idemitsu.com)

Table 2.3 shows the summarized performance of commercial fluorescent OLEDs. Compared to PHOLEDs (**Table 2.2**), red and green fluorescent OLEDs have at least two times smaller current efficiency and operational lifetime than their PHOLED counterparts. This is why the OLED–based products have universally adopted red and green PHOLEDs. However, the deep blue fluorescent OLED can attain a relatively longer lifetime than its PHOLED counterpart and thereby has been employed in commercial products, although greater improvement is still

required. The discussion on the operational lifetime of OLEDs, including intrinsic degradation mechanisms and potential solutions, will be provided in **Chapters 5** and **6**.

2.2. Optical and electrical characteristics of OLEDs

2.2.1. Charge injection

As briefly discussed in **§1.1**, undoped organic semiconductors are nearly insulators with negligible intrinsic carrier concentration (<10^5 cm^{-3}) due to their relatively large energy gap (>2 eV), i.e. $n_i \propto \exp\left(-E_g/2kT\right)$. Therefore, the electrical operation of organic optoelectronic devices should primarily depend on the externally injected or dissociated charges upon optical excitation. For example, the current flow in the OLED is determined by the charge injection efficiency from the electrodes, and by the bulk transport characteristics through the available electronic sites of the comprising organic layers.

To understand the charge injection process, we first introduce the mechanism and formula developed for a conventional, metal–inorganic semiconductor junction. Charge injection can be described by two mechanisms, electron tunneling and thermionic emission. The charge injection efficiency for both mechanisms is mainly determined by the energy level difference or the injection barrier, Δ, between the Fermi energy of the metal electrode (i.e. its work function) and the transport level of the semiconductor (i.e. the valence band or the LUMO for the inorganic and organic semiconductors, respectively).

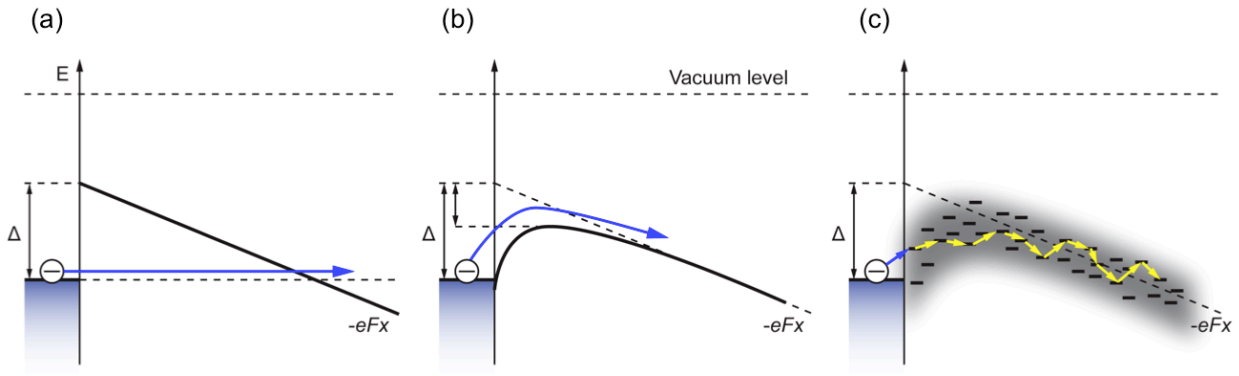

Figure 2.4 Charge injection mechanisms. (a) Tunneling, (b) thermionic emission, and (c) intermolecular polaron hopping are introduced. The image is reproduced from Ref. [6].

Fowler and Nordheim [53] formulated the electrical current such that the electrons emitted from the flat metal surface with an applied electric field of F tunnel into the triangular potential barrier of the *vacuum* of Δ, viz.,

$$J = AF^2 \exp\left(-\frac{4\sqrt{2m}\cdot\Delta^{3/2}}{3\hbar eF}\right), \tag{2.4}$$

where A is the injection coefficient, $\hbar$ is Planck constant and m is the electron mass (**Fig. 2.4 (a)**). However, this tunneling mechanism cannot apply to a organic semiconductor/metal interface due to the presence of the image charge contributing to the barrier reduction, and the unrealistically long tunneling distance derived for electrons in organic semiconductors (~10 nm) [6].

The thermionic emission mechanism was first formulated by Richardson [54] and then revised by Schottky [55] by taking into consideration injection barrier lowering by the image charge. This mechanism describes the charge injection process from the metal to the transport level of the semiconductor such that electrons overcome the injection barrier by gaining energy via thermal excitation (see **Fig. 2.4 (b)**). With an applied electric field, F, the injection current density by such process is given as

$$J = BT^2 \exp\left(-\frac{\Delta - \sqrt{qF/4\pi\varepsilon_r\varepsilon_0}}{kT} \right), \tag{2.5}$$

where A^* is the modified Richardson coefficient, T is the temperature and k_B is the Boltzmann constant. Here, $\sqrt{eF/4\pi\varepsilon_r\varepsilon_0}$ is the maximum barrier reduction induced by the image charge. Note that an image charge is formed in the metal at an equal distance from the interface to the real charge in the semiconductor with the opposite polarity.

Tunneling and thermionic injection processes are often unsuitable for explaining charge injection at the metal/organic semiconductor interface, which is not strictly dependent on the injection barrier (i.e. Δ). This is because of the energetically distributed transport sites in the disordered organic layers and therefore, charge injection becomes a stochastic process. The disorder of the organic semiconductor results from the comprising, randomly oriented molecules with a permanent dipole moment and their weak van der Waals interactions. Assuming a simple cubic lattice with the lattice constant a, the distribution of the energetic sites is Gaussian with a standard deviation σ_B [56]:

$$\sigma_B = \frac{2.35qp}{4\pi\varepsilon_r\varepsilon_0 a} \tag{2.6}$$

where p is the permanent dipole moment of the organic molecules. Accordingly, Gartstein and Conwell [57] proposed a random, intermolecular polaron hopping mechanism to explain the charge injection process for the disordered molecular system (see **Fig. 2.4 (c)**). Polaron hopping is thermally activated between two adjacent sites assisted by the phonon coupling, and thereby is a function of temperature, as well as electric field. Thus, the polaron hopping rate is given by:

$$R(E) \propto \exp\left(-\frac{E + |E|}{2kT} \right) \frac{\left(2E_b / \hbar\omega_0\right)^{|E|/\hbar\omega_0}}{\left(|E|/\hbar\omega_0\right)!} \tag{2.7}$$

at low temperatures (typically, $kT<<\hbar\omega_0$). Here, E is the activation energy for hopping between two electronic sites, E_b is the polaron binding energy, and ω_0 is frequency of the optical phonon mode. In the high temperature regime, the hopping rate becomes:

$$\begin{aligned} &\mathrm{R}(E) \propto \exp(-E/kT), && E>0 \\ &R(E) \propto 1, && E \le 0 \end{aligned} . \tag{2.8}$$

Here, the hopping rate at high temperature resembles the Marcus electron transfer rate [58] with the reorganization energy of $\lambda_{reorg} = 2E_b$. On the other hand, the low temperature rate can be simplified to:

$$R(E) \propto \left(\frac{1}{E_b kT}\right)^{1/2} \exp\left(-\frac{E_b}{2kT}\left(1+\frac{E}{2E_b}\right)^2\right) \tag{2.9}$$

in the limit of $E<<\hbar\omega_0$, indicating the one-step phonon process.

Baldo and Forrest [59] formulated the injected current density assuming either the Marcus-type (**Eq. 2.7**) or Miller-Abrahams-type (**Eq. 2.9**) hopping mechanism along with a thin, dipolar interfacial layer that is formed at the metal/organic interface. Their interface dipole leads to (i) the lowering of the injection barrier and (ii) the broadening of the energetic distribution of the "intermediate" interfacial states. Thus, the current density is limited by polaron hopping from the interfacial dipolar states to the adjacent organic sites. Based on this understanding, the injection-limited current from the various electrodes into Alq_3 (i.e. the standard OLED ETL material) was analyzed over a wide temperature range [59]. Although significant theoretical and experimental works including those introduced here have been done to understand the charge injection mechanism at the metal/organic interface, this process still leaves a considerable amount of complications. The interested reader is referred to Ref. [6], [10].

2.2.2. Charge transport

When the excess charges are supplied from the electrode into the organic semiconductor, the current flow is affected by space charge formed in the bulk. To satisfy such condition, the metal/organic semiconductor junction should be Ohmic with a low injection barrier to facilitate the electron flow in both directions and thus the current is not limited by the injection (see **§2.2.1**). Mott and Gurney formulated the unipolar space charge-limited (SCL) current for a trap-free insulating solid with ohmic contacts. Their formula was modified from Child's law:

$$J = \frac{9}{8}\varepsilon_r\varepsilon_0\mu\frac{E^2}{d} = \frac{9}{8}\varepsilon_r\varepsilon_0\mu\frac{V^2}{d^3} \tag{2.10}$$

where ε_r is the relative permittivity, ε_0 is the vacuum permittivity, μ is the mobility of the charge carrier in the solid, d is the thickness of the solid that charges traverse through from the injecting to the non-injecting electrode, and V is the applied voltage. Note that the SCL current density is proportional to V^2/d^3 so that it is useful for extracting μ in single-carrier-transport devices [60]. While the SCL current formula can be applied to the trap-free organic semiconductor, it does not sufficiently explain the current flow through the organic semiconductors that have the energetically distributed traps.

The energetics and a concentration of traps, and the applied electric field determine the trapping and thermally activated de-trapping characteristics of the traps. For the analytical derivation of the current density of the organic semiconductor having the traps, an exponential distribution of the density of traps is generally assumed as

$$n_t\left(E_t\right) = \frac{N_t}{kT_c}\exp\left(-\frac{E_t}{kT_c}\right) \tag{2.11}$$

where E_t is the energetic depth of the trap with respect to the LUMO or HOMO for the electron and hole traps, respectively, N_t is the total density of the traps, and T_c is the

characteristic temperature determining the distribution width. Accordingly, the trapped charge limited (TCL) current is derived as [61]

$$J_{TCL} = q\mu N_c \left(\frac{\varepsilon_r \varepsilon_0}{q n_t (E_t)} \right)^l \left(\frac{l}{l+1} \right)^l \left(\frac{2l+1}{l+1} \right)^{l+1} \frac{V^{l+1}}{d^{2l+1}} \tag{2.12}$$

where N_c is the total available density of transport sites and $l = T_c/T$. This formula can be applied to molecular thin films with typically $4 < l < 11$ [62]. This high power dependence on the applied voltage for the TCL current is attributed to the increased effective mobility. This is because the required detrapping energy is reduced as the deep energy traps are filled with the applied field. However, as all the traps are filled, they become the space charge and accordingly, the current density transits from the TCL to the SCL regime with a quadratic power dependence. This is typically observed at a high level of current densities (>10 mA/cm^2) or a high applied voltage [63].

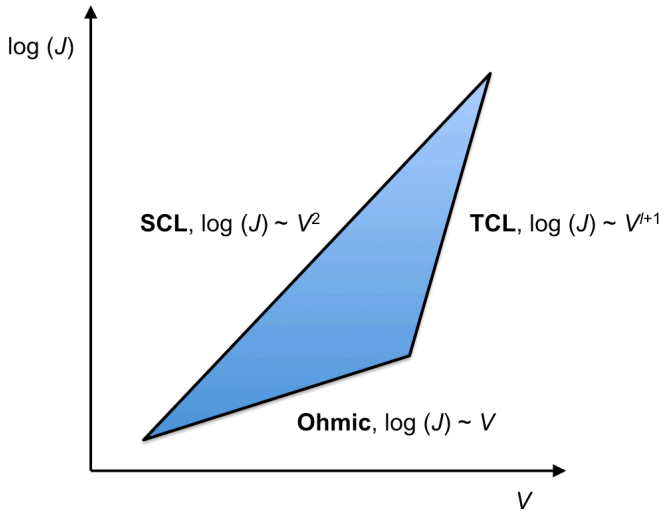

Figure 2.5 Power dendence of ohmic, space-charge limited, and trapped-charge limited current on applied voltage.

Interestingly, Lampert [64] reported that the *J–V* characteristics of disordered solids with distributed trap states are confined within the triangular region formed by SCL ($J \propto V^2$), TCL ($J \propto V^{l+1}$) and ohmic current ($J \propto V$) characteristics as shown in **Fig. 2.5**, which has been commonly observed in the organic semiconductors [62], [63], [65].

2.2.3. Charge recombination

Electrons and holes injected into the OLED undergo either the Langevin-type or trap-assisted recombination. The former occurs when electrons and holes are in proximity within their Coulomb capture radius, $r = e^2/\left(4\pi\varepsilon_r\varepsilon_0 k_B T\right)$, and thereby recombine with the rate as given by

$$R = \frac{e\left(\mu_h + \mu_e\right)}{\varepsilon_r\varepsilon_0} np = \gamma np \tag{2.13}$$

where γ is the Langevin recombination coefficient, and n and p are the electron and hole densities, respectively. The recombined electrons and holes then contribute to the formation of the bound excited states (i.e. excitons) that determine the optical characteristics of the device. When the traps are present near the charge transport sites, either holes or electrons are captured depending on the relative energetic positions of the traps, and the trapped charges then can recombine. This type of recombination is referred as the trap-assisted Shockley-Read-Hall (SRH) recombination [66] and since most traps in the organic semiconductors have deep energy levels within the forbidden gap, such recombination is in general nonradiative and undesirable. The SRH recombination rate for electron traps is given by

$$k_{SRH} = \frac{C_n C_p N_t}{C_n(n+n_1) + C_p(p+p_1)} \tag{2.14}$$

where C_n is the capture rate of the electron in the LUMO by the empty traps, C_p is the capture rate of the hole in the HOMO by the filled traps, N_t is the density of the electron traps, and n_1 and

p_1 are determined by the trap energies. It is reported that Langevin recombination contributes to the electroluminescent operation of OLEDs, while the SRH recombination leads to the loss of the device efficiency [67]. Along with those present within the as-grown device, traps are additionally generated during continuous operation of OLEDs due to the dissociation of molecular components. Such traps permanently degrade the device performance either via the SRH-type recombination direct exciton quenching [33].

2.2.4. Excitons

Upon the recombination of the electron on the LUMO and the hole on the HOMO of the organic molecule, an excited state bound by the Coulombic force is formed, resulting ina Frenkel exciton, see **§1.2**. The wavefunction of the molecular state including the excitons can be expressed as

$$\Psi_{total} = \psi_{spatial}\left(\{r_i\},\{R_i\}\right)\cdot\sigma_{spin}\left(\alpha_k,\beta_k,...\right) \tag{2.15}$$

where ψ_{spatial} is a spatial wavefunction depending on positions of the electrons (r_i) and the nuclei (R_i) comprising the molecule, and σ_{spin} is a total spin wavefunction of many electrons (represented by the individual spin wavefunction of α, β, and so on). Here, $|\psi_{\text{spatial}}|^2$ gives the probability of finding electrons at particular positions with the stationary nuclei.

The organic semiconductor allows at most two electrons with antiparallel spins to fill the same molecular orbital, and thus the molecular excited or ground states are simply two-electrons systems. According to the Pauli exclusion principle, the wave function of the state (**Eq. (2.15)**) comprised of two fermions (e.g. electrons) should be anti-symmetric under the particle exchange. Therefore, there exists two types of molecular states, one with anti-symmetric ψ_{spatial} and symmetric σ_{spin}, and the other with symmetric ψ_{spatial} and anti-symmetric σ_{spin}.

As briefly discussed in **Chapter 1**, the electron transfer or the optical transition in the organic semiconductor involves either or both frontier orbitals (HOMO and LUMO). For example, upon optical excitation with an energy higher than the energy gap, one electron from the HOMO is excited to the LUMO or higher molecular orbitals (i.e. LUMO+1, LUMO+2 and so on) that subsequently relax to the LUMO, forming the exciton. Thus, the exciton is the molecular excited state with two unpaired electrons, one residing in the HOMO and the other in the LUMO. Since each electron in the exciton has a spin of ½, the exciton can have the total spin number of $S = 0$ or 1. The spin wavefunction of the $S = 0$ state is given by

$$\sigma_S = \frac{1}{\sqrt{2}}\left(\uparrow(1)\downarrow(2) - \downarrow(1)\uparrow(2)\right) \tag{2.16}$$

where ↑ and ↓ denote the spin-up ($m_s = 1/2$) and spin-down ($m_s = -1/2$) states, respectively, and 1 and 2 refer to the index of two electrons comprising the system. Then, σ_s is anti-symmetric under the particle exchange (i.e. $1 \leftrightarrow 2$) and such state is called the singlet state. Note that the ground state with all filled HOMOs and empty LUMOs is thus the singlet state. On the other hand, the $S = 1$ state, referred to as the triplet, has three spin wavefunctions as

$$\begin{aligned}
\sigma_{T_+} &= \uparrow(1)\uparrow(2), \\
\sigma_{T_0} &= \frac{1}{\sqrt{2}}\left(\uparrow(1)\downarrow(2) + \downarrow(1)\uparrow(2)\right), \\
\sigma_{T_-} &= \downarrow(1)\downarrow(2).
\end{aligned} \tag{2.17}$$

These σ_T states are symmetric under the particle exchange. Based on the degeneracy of the excitons (**Eq. (2.16)** and **(2.17)**), the singlet-triplet generation ratio is given as 1:3 upon recombination of the random spin electrically injected holes and electrons [29]. However, the optical excitation only generates the singlet (100 %) in the organic molecules due to spin selection rules (see **§2.2.5**).

According to **Eq. (2.15)**, the singlet and triplet excitons should have symmetric and anti-symmetric $\psi_{spatial}$, respectively. Let's denote the spatially symmetric excited state with the singlet character as:

$$\psi_+ = \frac{1}{\sqrt{2}}\left(\psi_H(1)\psi_L(2) + \psi_H(2)\psi_L(1)\right) \tag{2.18}$$

where, ψ_H and ψ_L are the spatial wavefunctions of the electrons occupying the HOMO and LUMO, respectively. Then, the spatially asymmetric excited state with triplet character is given by:

$$\psi_- = \frac{1}{\sqrt{2}}\left(\psi_H(1)\psi_L(2) - \psi_H(2)\psi_L(1)\right). \tag{2.19}$$

The energy in each case is:

$$\begin{aligned} E_+ &= \frac{q^2}{4\pi\varepsilon}\left\langle\psi_+\right|\frac{1}{r_{12}}\left|\psi_+\right\rangle = J + K, \\ E_- &= \frac{q^2}{4\pi\varepsilon}\left\langle\psi_-\right|\frac{1}{r_{12}}\left|\psi_-\right\rangle = J - K. \end{aligned} \tag{2.20}$$

where r_{12} is the distance between two electrons (1 and 2), and J and K are Coulomb and exchange integrals, respectively, given by:

$$\begin{aligned} J &= \frac{q^2}{4\pi\varepsilon}\left\langle\psi_H(1)\psi_L(2)\right|\frac{1}{r_{12}}\left|\psi_H(1)\psi_L(2)\right\rangle, \\ K &= \frac{q^2}{4\pi\varepsilon}\left\langle\psi_H(1)\psi_L(2)\right|\frac{1}{r_{12}}\left|\psi_H(2)\psi_L(1)\right\rangle. \end{aligned} \tag{2.21}$$

Thus, the singlet exciton is energetically higher than the triplet exciton by $2K$, the exchange interaction energy, which is determined by the overlap between HOMO and LUMO orbitals in the excited state configuration. The exchange energy, or the singlet-triplet gap ($\Delta_{ST} = 2K$), varies from 0.05 to 1 eV; for standard organic materials (0.7–1 eV) [68], phosphorescent

metallorganic complexes (0.2–0.3 eV) [69], and thermally-assisted delayed fluorescent molecules (0.05–0.2 eV) to achieve the efficient triplet-to-singlet upconversion [70].

2.2.5. Excitonic energy transitions

The rate of the optical transition, such as the light absorption leading to exciton generation in the OPV and the light emission via radiative recombination of the excitons in the OLED, is determined by the Fermi's golden rule, *viz*.,

$$\Gamma_{if} = \frac{2\pi}{\hbar}\left|\left\langle \Psi_i \left| e\vec{r} \right| \Psi_f \right\rangle\right|^2 \rho\left(E_f\right) \tag{2.22}$$

where Ψ_i and Ψ_f are wavefunctions of initial and final states participating in the transition, respectively, $e\boldsymbol{r}$ is the electric dipole operator used as the perturbing Hamiltonian and ρ is the joint density of the initial and final states of the wavefunctions. By plugging **Eq. (2.15)** into **Eq. (2.22)**, we get

$$\Gamma_{if} = \frac{2\pi}{\hbar}\left|\left\langle \phi_{e,i}(\vec{r}_i) \left| q\vec{r} \right| \phi_{e,f}(\vec{r}_f) \right\rangle\right|^2 \left|\left\langle \Phi_{N,i}(\vec{R}_i) \middle| \Phi_{N,f}(\vec{R}_f) \right\rangle\right|^2 \left|\left\langle \sigma_i(S_i) \middle| \sigma_f(S_f) \right\rangle\right|^2 \rho\left(E_f\right) \tag{2.23}$$

According to the Born-Oppenheimer approximation, ψ_{spatial} is decomposed into the electronic wavefunction, ϕ_e, and the nuclear wavefunction, Φ_N, that describes vibrational and rotational motions of the nuclei. That is, the electronic and nuclear motions are assumed to be independent because the electrons respond nearly instantaneously to the change of the nuclear positions due to their smaller masses. In the same vein, the electric dipole operator only operates on the electronic function because during the transition, the motion of the electron only slightly affects the nuclei of much heavy mass. Also, the total electron spin (σ) of the state is unaffected by the electronic transition.

Therefore, **Eq. (2.23)** gives the transition selection rule. First, the spatial electronic integral, $\left|\left\langle \phi_{e,i}(\vec{r}_i)\middle| q\vec{r} \middle|\phi_{e,f}(\vec{r}_f)\right\rangle\right|^2$, requires that the transition is only allowed between two states of the opposite parity under the spatial inversion (i.e. *gerade* from/to *ungerade* states, see **§2.3.2**), because the electric dipole operator has an odd parity. The second term $\left|\left\langle \Phi_{N,i}(\vec{R}_i)\middle|\Phi_{N,f}(\vec{R}_f)\right\rangle\right|^2$, referred to as the Franck-Condon factor, evaluates the overlap of the vibronational wavefunctions between initial and final states. That is, the electronic transition is likely to occur from the ground vibrational state to a higher energy electronic manifold (According to the Franck-Condon principle, see below). Finally, the term, $\left|\left\langle \sigma_i(S_i)\middle|\sigma_f(S_f)\right\rangle\right|^2$, dictates that the total spin number should be conserved between final and initial states that participate in the transition (i.e. triplet ↔ triplet or singlet ↔ singlet). Since the molecular ground state has singlet character, only the transition from the excited singlet state to the ground state is allowed, i.e. a rapid and radiative fluorescent process with the natural decay time of 1–10 ns [71]. In the same vein, only singlet excited states can be generated by the optical excitation. On the other hand, the transition from the excited triplet state to the ground state, also known as a phosphorescent process, is forbidden so that the triplet states are de-excited in the form of heat with extremely long decay time of 1–100 ms. However, the use of metallorganic complexes allows the radiative transition from the triplet states by introducing strong perturbations between singlet and triplet states [30] (see **§2.2.6**).

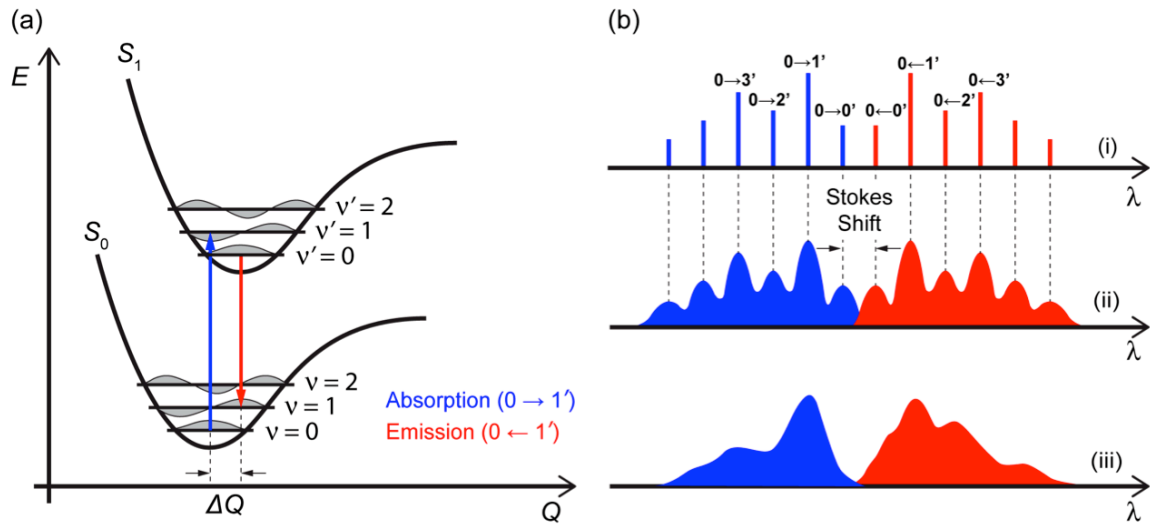

Figure 2.6 Franck-Condon principle diagram. (a) Optical transitions between lowest excited and ground states (b) corresponding to absorption and emission spectra for the molecule (i) in the gas phase and in the solid phase at (ii) low and (iii) high temperatures.

Several aspects of the optical transitions (i.e. absorption and fluorescence) can be explained using the Franck-Condon principle. Since the electron redistribution upon excitation and relaxation occurs much faster than any change in the position of the nuclei, and the momentum of the vibrational states (fs vs. ps), the optical transition is represented by the vertical line at a constant nuclear coordinate. Multiple, allowed vibronic transitions appear as spectral lines whose intensities are governed by the Franck-Condon factor. Note that sharp spectral lines are observed only in cold gases, which undergo the inhomogeneous broadening in the liquid or solid phase at room temperature because of the inter- and intra-molecular phonon coupling. Optical absorption occurs from the lowest vibrational level (v = 0) in the ground state to the multiple vibrational levels of the excited electronic manifolds as shown in **Figure 2.6 (a)**. According to Kasha's rule, the photon emission process originates from the single, lowest excited state, due to the rapid and efficient vibrational relaxation and internal conversion from the higher energy electronic manifold.

Note that electrons are redistributed in the molecular excited state, often leading to a shift of the equilibrium positions of the nuclei (ΔQ in **Fig. 2.6 (b)**) and the distortion of the electronic potential with respect to the ground state. This is common due to the occupation of the anti-bonding orbitals upon the excitation that weakens the bonds and distorts the molecule. Discrepancy breaks the mirror symmetry between absorption and fluorescent spectral shapes and results in the spectral gap between their lowest energy (0–0) transitions, referred to as the Stokes shift. This phenomena becomes more severe for organic molecules with less stiffness [72] and those in the polar media such as solvents, which will be discussed in greater detail in **Chapter 4**.

2.2.6. Principle of radiative phosphorescence

In phosphorescent emitters comprised of heavy metal atom center and coordinated organic ligands, there exists a strong perturbation due to spin-orbit coupling (SOC) that efficiently mixes the singlet and triplet states. The SOC perturbation breaks the spin-conservation requirement in the Fermi's golden rule, enhancing the transition rate from the excited triplet to the singlet ground state. The SOC is the quantum mechanical interaction between the spin of the electron and the magnetic field generated by the electron orbital, where strength is given by [73]:

$$\Delta H_{SOC} = \frac{\mu_B}{\hbar mec^2} \cdot \frac{\partial V(r)}{r\,\partial r} \cdot \left(\vec{L} \bullet \vec{S}\right) = -\frac{Z\mu_B}{4\pi\varepsilon_0 \hbar mec^2} \cdot \frac{1}{r^3} \cdot \left(\vec{L} \bullet \vec{S}\right) \tag{2.24}$$

where $\boldsymbol{L}$ and $\boldsymbol{S}$ denote angular and spin angular momentum vectors, respectively, $V(r) = \frac{Ze}{4\pi\varepsilon_0 r}$ is the potential of one electron in the hydrogenic system with the atomic number, Z, and μ_B is the Bohr magnetron. The expectation value of the LS coupling term can be rewritten using the eigenvalues of orbital (l), spin (s) and total angular momentum (j) as

$$\left\langle \vec{L} \bullet \vec{S} \right\rangle = \frac{1}{2}\left(\left\langle \vec{J} \right\rangle^2 - \left\langle \vec{L} \right\rangle^2 - \left\langle \vec{S} \right\rangle^2 \right) = \frac{\hbar^2}{2}\left[j(j+1) - l(l+1) - s(s+1) \right]. \tag{2.25}$$

The expectation value of $1/r^3$ calculated in the spherical coordinate is:

$$\left\langle \frac{1}{r^3} \right\rangle = \frac{2}{a^3 n^3 l(l+1)(2l+1)} \tag{2.26}$$

where $a = \frac{\hbar^2}{Zk_e me^2} n^2$ is the effective Bohr radius with the atomic number Z. Thus, the energy difference of the SOC perturbation between states is given by:

$$\left\langle \Delta H_{SOC} \right\rangle = -Z^4 \cdot \frac{\mu_B \hbar^2}{4\pi\varepsilon_0 mec^2 a_0^3} \cdot \frac{j(j+1) - l(l+1) - s(s+1)}{n^3 l(l+1)(2l+1)}. \tag{2.27}$$

Eq. (2.27) indicates that the magnitude of the SOC interaction is proportional to Z^4 and thus the effect increases for heavy metal atoms such as iridium or platinum, typically used in the phosphorescent organometallic complexes.

According to Fermi's golden rule (**Eq. (2.22)**), the rate of the phosphorescence is given by [6]:

$$\Gamma_{ph} \propto \sum_i \left| \frac{\left\langle {}^1\psi_i \middle| H_{SOC} \middle| {}^3\psi_1 \right\rangle}{E(T_1) - E(S_i)} \right|^2 \left\langle {}^1\psi_i \middle| e\vec{r} \middle| {}^1\psi_0 \right\rangle , \tag{2.28}$$

where $E(T_1)$ and $E(S_i)$ is the energy of the lowest excited triplet and i-th singlet manifold, respectively, ${}^3\psi_1$, ${}^1\psi_i$, and ${}^1\psi_0$ are wavefunctions of the lowest excited triplet, i-th and ground state singlet manifold, respectively, H_{SOC} is the Hamiltonian of the SOC perturbation. Thus, the strength of the phosphorescent transition is enhanced with decreasing energy gap between singlet and triplet states and the increased SOC interaction by using heavy metal atoms. Based on this understanding, iridium(III), platinum (II) and palladium (II)-based phosphorescent emitters with

fast natural decay time of the triplet state (1–10 μs) were introduced, resulting in very high efficiency PHOLEDs [31], [41], [69], [74], [75].

2.2.7. Energy transfer

The energy of excitons can be transferred between molecular sites depending on their distance, wavefunction overlap and etc., and thus, excitons are mobile in the solid. Energy transfer is divided into two types: dipole-interaction based long-range Förster transfer and charge exchange-based short-range Dexter transfer. Förster resonant energy transfer (FRET) requires the resonant interaction between the excited state dipole on the donor molecule and the ground state dipole on the acceptor molecule, and their spins must be conserved during the transfer. The latter requirement allows only the excited singlet–to–ground singlet FRET, while that from the triplet state is forbidden. However, if the triplets can be efficiently and radiatively relaxed on the donor molecules (i.e. phosphorescence), the triplet–to–singlet FRET is allowed, enabling phosphor sensitized fluorescence [76]. The rate of the FRET is given by:

$$k_{FRET} = \frac{1}{\tau_D}\left(\frac{R_0}{R_{DA}}\right)^6 \tag{2.29}$$

where τ_D is the natural decay lifetime of the excited state on the donor molecule, R_{DA} is the distance between donor and acceptor molecules, and R_0 is the Förster radius defined as [77]

$$R_0^6 = \frac{9000\ln 10}{128\pi^5 n^4 N}\cdot\kappa^2\Phi_D\int_0^\infty \frac{f_D(\nu)\sigma_A(\nu)}{\nu^4}d\nu\,. \tag{2.30}$$

Here, n is the refractive index of the medium, N is the Avogadro's number, κ is the orientation factor, ν is the wavenumber, $f_D(\nu)$ is the spectral distribution of the fluorescence from the donor molecule, and $\sigma_A(\nu)$ is the molar absorption coefficient of the acceptor molecule. **Eq. (2.29)** indicates that when $R_{DA} = R_0$, the rates of the FRET and the natural decay of the excitons

on the donor molecules become equal. To enhance FRET, the Förster radius in **Eq. (2.30)** should be enlarged via increasing the spectral overlap between donor emission and acceptor absorption spectra. This strategy has been widely employed to facilitate exciton transfer in host (donor)–guest (acceptor) systems both in fluorescent and phosphorescent OLEDs [28], [30]. Note that κ^2 dictates that the FRET only occurs between non-orthogonal dipoles of the donor and acceptor molecules. κ^2 =2/3 for a randomly oriented molecular system [77]. In summary, the FRET governs the long-range transfer of the excited singlet state via dipole-dipole interaction whose transfer radius (R_0) ranges from 5 nm to 10 nm for the typical organic small molecules [45].

Dexter transfer is a coherent exciton transfer process based on the simultaneous charge exchange between the donor and the acceptor molecules. The Dexter transfer rate is [78]:

$$k_{Dexter} = \frac{2\pi}{\hbar}\Gamma^2 \int_0^\infty f_D(\upsilon)\sigma_A(\upsilon)d\upsilon \,. \tag{2.31}$$

Here, Γ is the matrix element for the charge exchange as

$$\begin{aligned}\Gamma^2 &= \left\langle \Psi_D(1)\Psi_A^*(2)\left|\frac{1}{4\pi\varepsilon_r\varepsilon_0 R_{DA}}\right|\Psi_D^*(1)\Psi_A(2)\right\rangle \\ &= \left\langle \Phi_D(1)\Phi_A^*(2)\left|\frac{1}{4\pi\varepsilon_r\varepsilon_0 R_{DA}}\right|\Phi_D^*(1)\Phi_A(2)\right\rangle\left\langle \sigma_D(2)\middle|\sigma_A(2)\right\rangle\left\langle \sigma_D^*(1)\middle|\sigma_A^*(1)\right\rangle\end{aligned} \,. \tag{2.32}$$

where Ψ, Φ and σ are the molecular ground state wavefunction, its spatial and spin components, respectively, with their excited analogs, Ψ^*, Φ^*, and σ^*. According to the **Eq. (2.32)**, Dexter transfer is allowed under the condition that (i) there is an intimate overlap between orbitals of the donor and the acceptor, and (ii) their integrated spin is conserved before and after the transition. Since the ground states of the donor and acceptor molecules are both singlets, their excited states can be either both triplets, or both singlets. Thus, unlike FRET, the Dexter transfer allows triplet–to–triplet energy transfer, which is shown the dominant mechanism for the triplet diffusion in the PHOLED EMLs [79]. Given that spin selection rules for the Dexter transfer is

satisfied, $\Gamma^2 \propto \exp\left(-\frac{2R_{DA}}{\lambda}\right)$, where λ is an effective van der Waals radius of the donor and acceptor molecules. This indicates that the donor and acceptor should be in close proximity to one another as in **Eq. (2.32)** enabling the charge exchange. Since λ has been experimentally calculated in the range of 1.3–1.6 nm for the triplet–to–triplet transfer in phosphorescent host-guest systems [79], Dexter transfer is likely to occur only between the nearest-neighboring molecular sites (i.e. intermolecular spacing of $r \sim 1$ nm).

2.3. Fundamentals of blue PHOLED materials

2.3.1. Design principles of blue-emitting phosphorescent emitters

There are two approaches to obtain the large energy gap for the blue phosphorescent emitters: either by stabilizing their HOMO or destabilizing the LUMO with respect to the vacuum level as shown in **Fig. 2.7**.

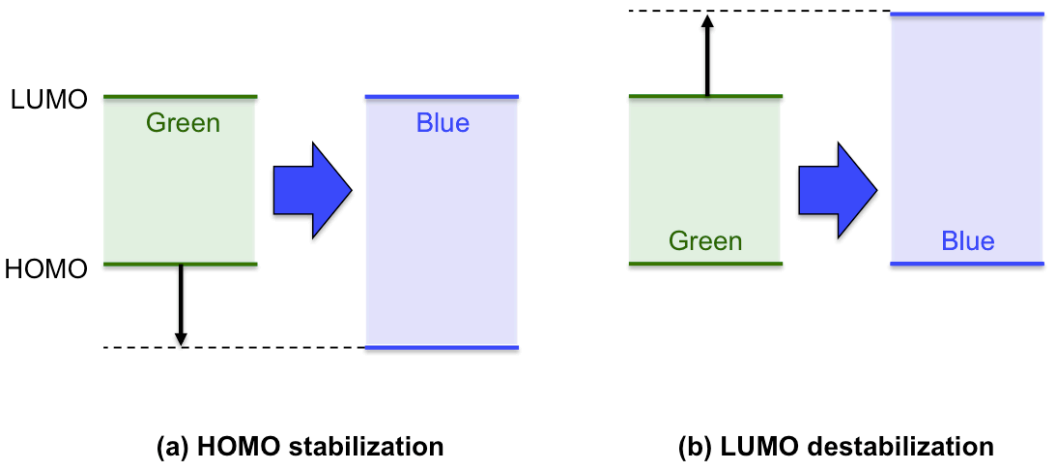

Figure 2.7 Two approaches to design blue phosphorescent emitters. (a) HOMO stabilization or (b) LUMO destabilization with respect to the vacuum level.

The molecular orbitals, including the frontier orbitals, are constructed by the linear combination of the atomic orbitals and are generally represented by the part of the molecules where the electron distribution is largest. Tris-cyclometalated iridium (III) complexes have HOMOs and LUMOs on different molecular moieties, and thus the nearly independent control of the energetics of each orbital is possible. **Figure 2.8** shows the molecular formula and frontier orbitals of the archetypal green phosphorescent emitter, Ir(*ppy*)$_3$.

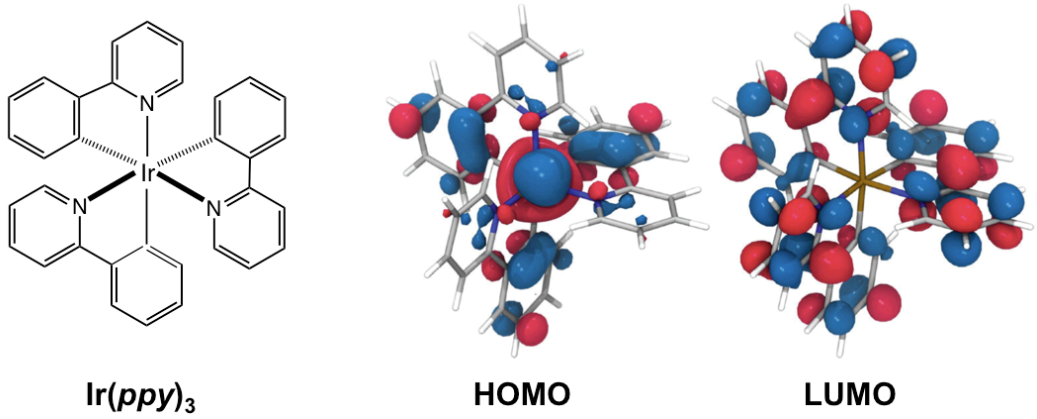

Figure 2.8 Molecular formula of Ir(*ppy*)$_3$ and its frontier orbitals diagram. HOMO and LUMO are calculated by density functional theory calculation (images obtained from Ref. [80]).

The Ir(*ppy*)$_3$ HOMO is comprised of the phenyl-π and Ir-d orbitals, while its LUMO is preferentially localized on the pyridine moiety. Most Ir (III)-based organometallic complexes are designed based on the structure of Ir(*ppy*)$_3$. Their HOMOs and LUMOs can be redistributed, for example, by attaching different functional groups to the phenyl or pyridine rings, respectively.

Figure 2.9 shows tris[2-(4,6-difluorophenyl)pyridyl] Ir(III) or Ir(F_2*ppy*)$_3$, having fluoride (i.e. a fluorine anion) attached to the 4 and 6 positions of the phenyl ring of Ir(*ppy*)$_3$ [81]. The fluoride is an electron-withdrawing group that attracts the electron from the π-conjugated system,

rendering it more electrophilic. As a result, the HOMO of Ir(F_2*ppy*)$_3$ is lowered compared to that of Ir(*ppy*)$_3$, leading to the wider energy. It is also reported that by replacing one ligand of the homoleptic Ir (III) organometallic complex with a functional ancillary ligand, the HOMO of the resulting heteroleptic complex can be adjusted while its LUMO is nearly unaffected [82]. Then, the luminescence characteristics such as the quantum efficiency and the emission energy of the Ir-complex is modified.

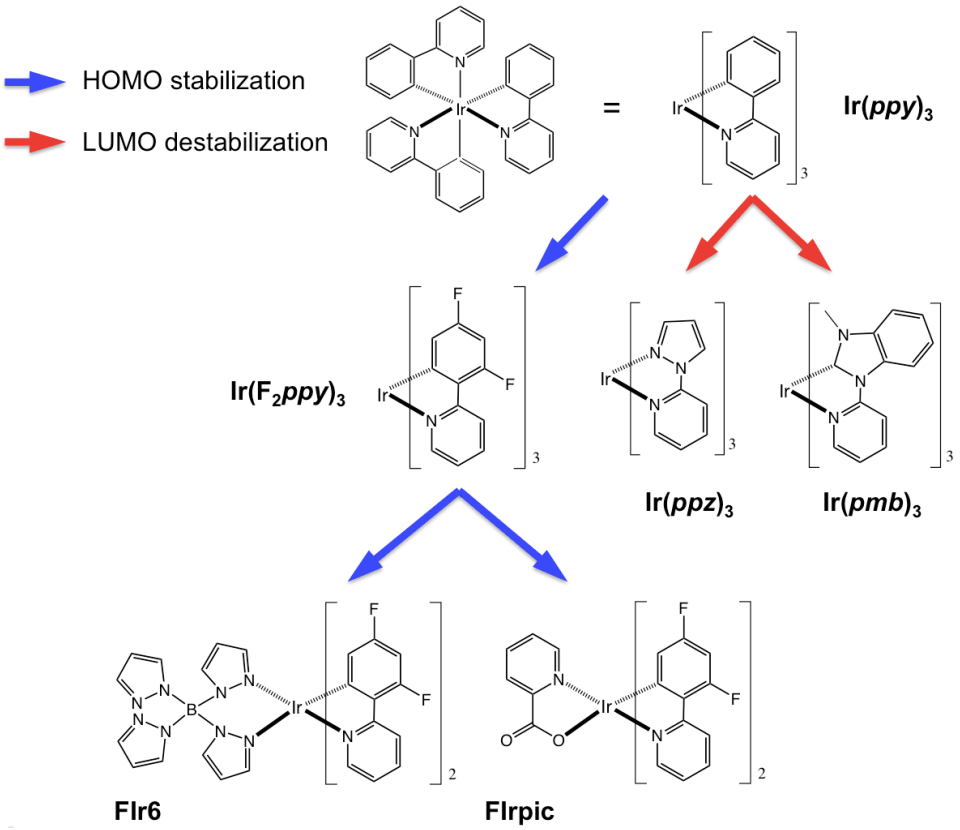

Figure 2.9 Examples of blue-emitting Ir(III)-based organometallic complexes. By adding an electron withdrawing fluoride to the phenyl ring of Ir(*ppy*)$_3$, cyan-emitting Ir(F_2*ppy*)$_3$ is made. By replacing one of the cyclometalated ligands of Ir(F_2*ppy*)$_3$ with the ancillary ligand, heteroleptic FIrpic and FIr6 complexes are made. By replacing the pyridine ring of the *ppy* ligand with either pyrazolyl or methylbenzimidazolyl, homoleptic Ir(*ppz*)$_3$ or Ir(*pmb*)$_3$ complexes are made, respectively.

The ancillary ligand of Ir-complexes, such as acetylacetone (*acac*), picolinate (*pic*), pyrazolyl (*ppz*) and so on, interacts with the HOMO of the cyclometalated ligands via the metal orbitals, and thereby the energy of the singlet metal-ligand-charge-transfer state (^{1}MLCT) is modified while the triplet ligand-centered (^{3}LC) state is nearly unperturbed. If the ancillary ligand is used in the Ir-complex such that the HOMO is lowered without affecting the LUMO compared to that of the homoleptic complex, i.e. increased energy of the ^{1}MLCT with unchanged ^{3}LC, the overall emission energy (E_{em}) of the lowest excited state (an admixture of both ^{1}MLCT and ^{3}LC states) increases. $T_1 = \alpha\left|{}^1MLCT\right\rangle + \sqrt{1-\alpha^2}\left|{}^3LC\right\rangle$ where $\alpha = \dfrac{\left\langle {}^1MLCT\left|H_{SOC}\right|{}^3LC\right\rangle}{\Delta E}$. Here, ΔE is the energy difference between ^{1}MLCT and ^{3}LC states and H_{SOC} is the spin-orbit coupling perturbation. The nonradiative decay rate of the exciton (k_{nr}) decreases according to the energy gap law ($k_{nr} \sim \ln(E_{em})$). But at the same time, the radiative rate (k_r) is determined by the oscillator strength of T_1, which is reduced with the increase in ΔE and the reduced spin-orbit-perturbed ^{3}LC by the metal orbitals in ^{1}MLCT. Since the luminescent quantum efficiency of the Ir-complex is $\Phi = k_r/\left(k_r + k_{nr}\right)$, care must be taken in choosing the ancillary ligand.

The efficient sky blue-emitting phosphorescent emitter, Bis[4,6-di-fluorophenyl)-pyridinato-N, C$^{2'}$]picolinato Ir(III) (FIrpic), has been demonstrated. FIrpic is modified from Ir(*ppy*)$_3$ by adding the electron withdrawing group and replacing one cyclometalated *ppy* ligand with the ancillary *pic* ligand [83]. Combined with the large energy-gap host that has a significant absorption-emission overlap for efficient energy transfer, FIrpic can achieve the photoluminescence (PL) quantum yield of 100 % [44], and thereby highly efficient blue PHOLEDs based on FIrpic can achieve EQE > 30 % [84]. However, the emission of FIrpic yields a light blue color corresponding to CIE = (0.18, 0.33) which is unsuitable for display applications requiring much deeper blue, i.e. CIE = (0.15, 0.06) [85]. Many efforts have been

made to further increase the energy gap of the Ir-complex by fluorination or by adding another ancillary ligand such as bis(4',6'-difluorophenylpyridinato)tetrakis(1-pyrazolyl)borate (FIr6) with a CIE of (0.16, 0.26) [86]. However, a major concern in using the Ir-complexes with the fluorine and ancillary ligand is that both components are easily cleaved during device operation [87]. The operational lifetime of such device is unacceptably short, T80 < 10 hrs at L_0 = 1000 cd/m^2.

As an alternative to obtain a large energy gap for deep blue emitters, the LUMO can be increased towards the vacuum level without changing the HOMO energy. For this purpose, a more electron-rich or electron donating group can be substituted with the pyridine, such as tris[1-phenylpyrazolyl]Ir (III) (Ir(*ppz*)$_3$) as shown in **Fig. 2.9**. Ir(*ppz*)$_3$ has a larger energy gap 4.5 ± 0.1 eV vs. 3.6 ± 0.1 eV for Ir(*ppy*)$_3$. This is attributed to a significantly stabilized LUMO of Ir(*ppz*)$_3$ = 0.6 ± 0.1 eV vs. 1.2 ± 0.1 eV for Ir(*ppy*)$_3$, while their HOMO energies are nearly similar at 4.9 ± 0.1 eV and 5.0 ± 0.1 eV, respectively [81]. As a result, Ir(*ppz*)$_3$ exhibits phosphorescence emission that peaks at λ = 414 nm vs. 494 nm for Ir(ppy)$_3$ at T = 77 K, although it fails to emit at room temperature due to non-radiative loss via triplet metal-centered ligand-field states (see **§2.3.2**).

To reduce the non-radiative loss channel found in the large energy gap Ir–complexes, the N–heterocyclic carbene (NHC) ligand was introduced. For example, tris(1-phenyl-3-methylbenzimidazolin-2-yildene-C,C$^{2'}$) Ir or Ir(*pmb*)$_3$ emits at λ_{peak} = 378 nm with a PL quantum efficiency of 37 ± 5 %. NHC Ir(III) complexes have a very wide energy gap for deep blue emission with potentially high efficiency, are thermodynamically stable and have strong metal-ligand bonds. Therefore, many blue phosphorescent emitters are designed based on NHC ligands. Detailed characteristics of NHC Ir(III) complexes and their use in PHOLEDs to achieve

the deep blue color with very high efficiency will be discussed in **Chapter 4**. Furthermore, they are used as non-emissive, ancillary dopants in sky blue PHOLEDs to improve their operational stability, which will be introduced in **Chapter 6**.

2.3.2. Metal-centered ligand-field state

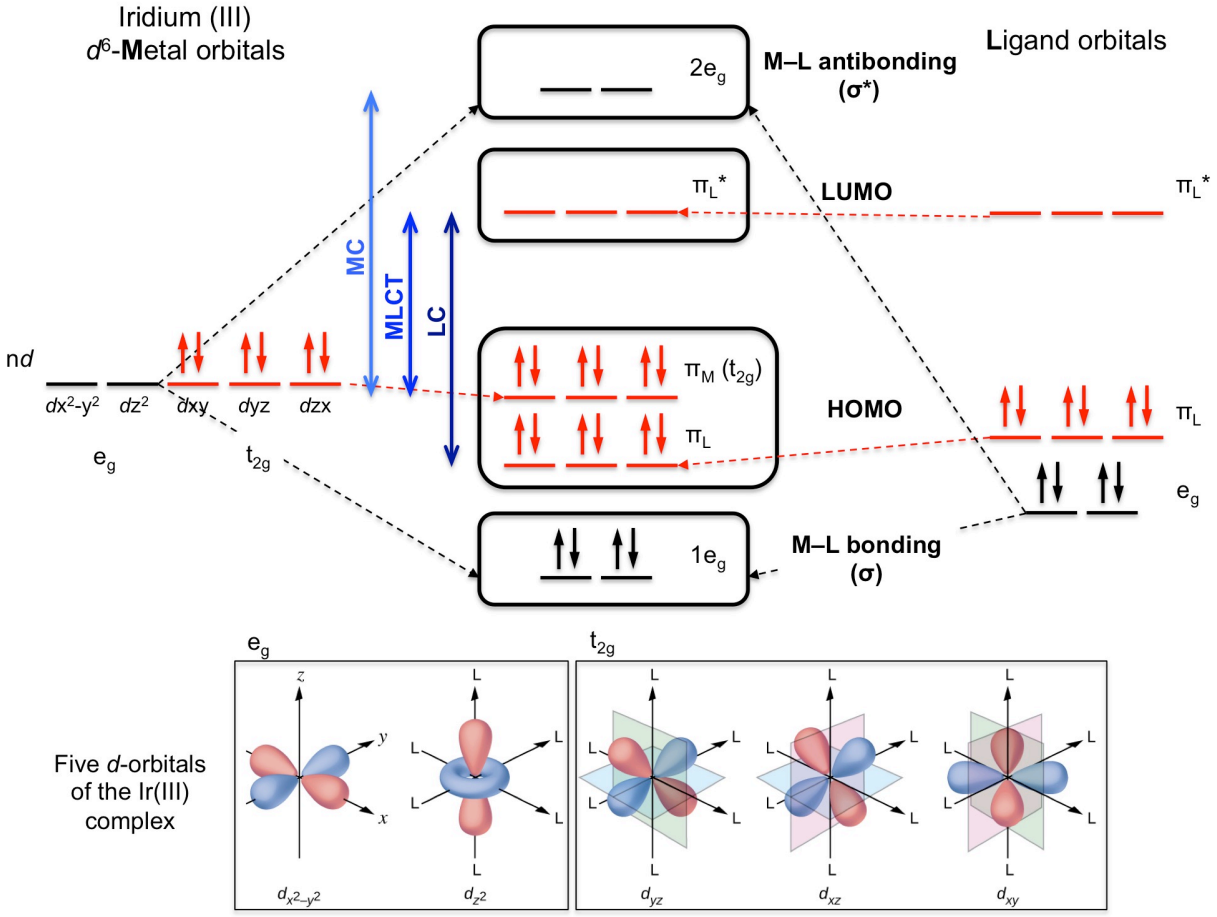

Figure 2.10 Molecular orbital diagram for the octahedral Ir (III) organometallic complex. Isolated orbitals for the Ir atom and ligands, and those for the coordinated complex are shown. *e* and *t* refer to doubly and triply degenerated *d*-orbitals, respectively, of the Ir ion. MC, MLCT, and LC refer to metal-centered ligand-field, metal-ligand-charge-transfer and ligand-centered transitions, respectively. Image of five unhybridized Ir *d*-orbitals is obtained from http://opentextbc.ca/chemistry.

To understand metal-centered ligand-field states (^{3}MC), we first discuss the molecular orbitals of the octahedral Ir(III) organometallic complex [88]. **Figure 2.10** shows the orbitals of the transition Ir(III) ion, ligands, and their coordinated complex. In the uncoordinated Ir(III) ion, the electrons are distributed across the five *d* orbitals having identical energy. $dx^2–y^2$ and dz^2 orbitals directly point to the ligands and these doubly degenerate orbitals are referred as e_g. The triply degenerate orbitals (t_{2g}) include *dxy*, *dyz*, and *dzx*, pointing between the ligands. Here, the subscript g for the orbitals e_g and t_{2g} indicates their *gerade* symmetry where the inversion of the corresponding orbital through the center of symmetry in the molecule conserves the phase. This is compared to the *ungerade* (*u*) symmetry, where the phase of the molecular orbital changes upon the inversion through the center of symmetry. When the Ir(III) ion is coordinated with the ligands, the electrons in the ligands repel those in the e_g orbitals of the Ir-ion more strongly than t_{2g}, resulting in the higher potential of the e_g vs. t_{2g} (see **Fig. 2.10**). t_{2g} orbitals of the Ir(III) ion contribute to π orbitals of the coordinated complex (π_M) that form the HOMO along with the occupied π orbitals of the ligands (π_L). On the other hand, unoccupied π orbitals of the ligands (π_L^*) become the LUMO of the complex. Upon coordination, e_g orbitals of the metal ion and ligands that point toward each other are split into σ-bonding and σ^*–antibonding orbitals.

The electronic transitions between $\pi_M \leftrightarrow \pi_L^*$, $\pi_L \leftrightarrow \pi_L^*$, and $\pi_M \leftrightarrow 2e_g$ are referred as metal-ligand charge transfer (MLCT), ligand-centered (LC), and metal-centered ligand-field (MC) transitions, respectively. In the Ir (III) organometallic complex, phosphorescence is a combination of the MLCT and LC transition between the excited triplet and ground states [69]. On the other hand, the MC transition is a forbidden process, because the transitions between two states (t_{2g} and e_g, *gerade* ↔ *gerade*) with the same parity in the centrosymmetric molecule are forbidden according to the Laporte selection rule [88]. That is, the electric dipole operator, $e\boldsymbol{r}$,

responsible for the transition probability has odd symmetry under the spatial inversion so that the transition probability between the states with the same parity vanishes or yields very small oscillator strength via coupling with the anti-symmetric vibrational states.

The MC transition is nonradiative and limits the efficiency of the Iridium (III) organometallic complexes when involved with the emission process. Since the ^{3}MC state is an antibonding (σ^*) orbital of the M–L bond (**Fig. 2.10**), its energy is highly destabilized and the electronic configuration is distorted from the lowest excited triplet state (T_1). Therefore, the potential of the ^{3}MC state is displaced from that of T_1 as shown in **Figure 2.11**. When these two states are strongly coupled and displaced from each other, their potentials overlap and the transition between two states shows an Arrhenius behavior with the thermal activation energy required for the surface crossing [88].

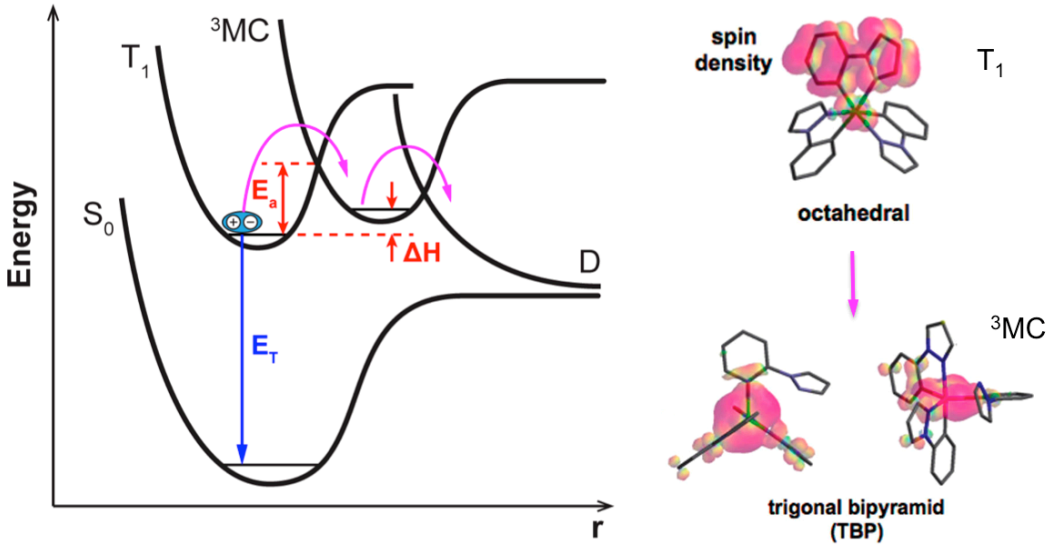

Figure 2.11 Potential well diagram for Ir (III) organometallic complexes. When ^{3}MC state is occupied, one of metal-ligand bonds is ruptured and the Ir complex becomes the trigonal bipyramidal (TBP) structure [89]. There is an activation energy, E_a, required for transferring from the lowest triplet state (T_1) to ^{3}MC, and ΔH is defined as the energy difference between T_1 and TBP states. E_T refers to the lowest triplet state energy.

When the ^{3}MC state of the Ir (III) organometallic complex is thermally accessed from the lowest triplet state (T_1) by overcoming the thermal activation energy, E_a, one of the metal ligand bond is cleaved and the complex becomes the five-coordinated, trigonal bipyramidal (TBP) structure [89]. The energy difference between the T_1 and TBP states, ΔH, can be obtained by the density functional theory (DFT) calculation for several heteroleptic Ir (III) complexes. **Figure 2.12** shows some examples including Ir(*ppy*)$_3$, Ir(*ppz*)$_3$ and Ir(*pmb*)$_3$.

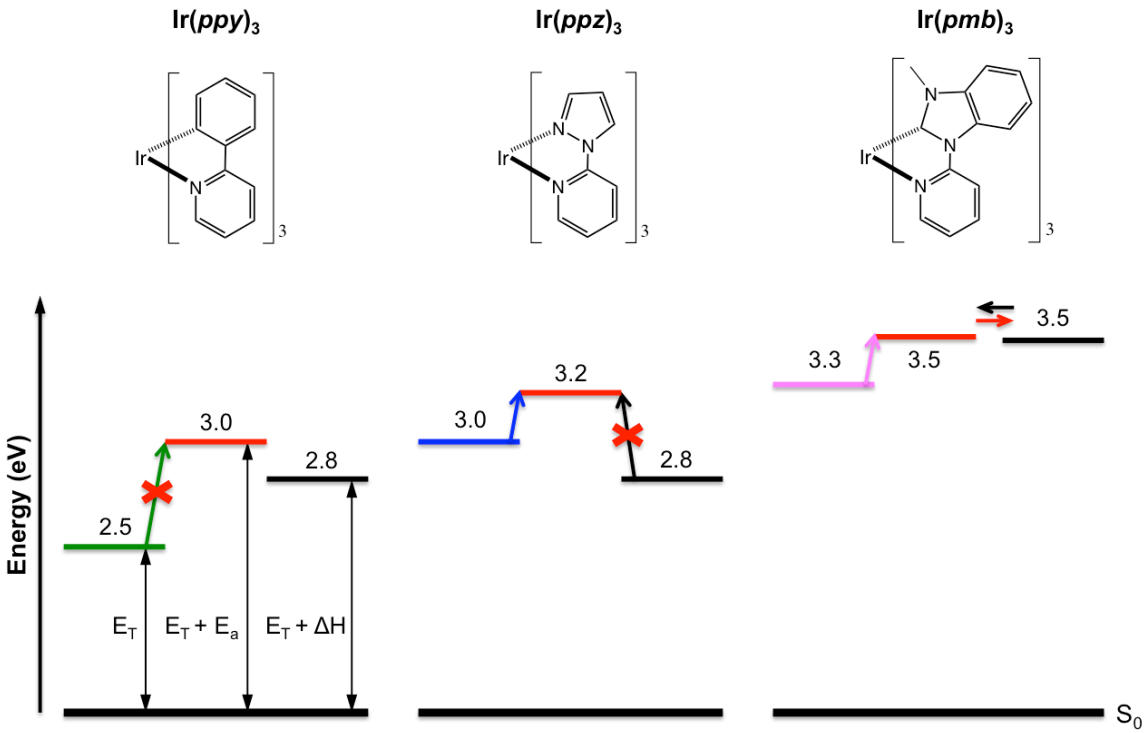

Figure 2.12 Schematic energy diagram for excited state of several iridium (III) organometallic complexes.

Since Ir(*ppy*)$_3$ has a larger E_a = 0.5 eV than other complexes, the excited state cannot thermally transfer from T_1 to the ^{3}MC state. This leads to negligible nonradiative loss via the ^{3}MC state, contributing to its PL quantum efficiency of Φ_{PL} ~ 100%. Likewise, most red and green Ir (III) complexes have relatively stable emissive T_1 states (i.e. their $E_T \approx$ 2.4 and 2.1 eV,

respectively) compared to the ^{3}MC or TBP states so that their efficiencies are not decreased by coupling to the ^{3}MC state. However, Ir (III) complexes with high E_T for blue emission have unavoidably small E_a so that their excited states are more likely to couple to the ^{3}MC states compared to their red or green analogs. For example, the excited state of Ir(*ppz*)$_3$, designed for the blue phosphorescent emitter, can readily cross from T_1 to ^{3}MC due to its low E_a = 0.2 eV and since the TBP structure of Ir(*ppz*)$_3$ is more stabilized than its T_1 state, the transition from T_1 to TBP states becomes irreversible. As a result, Ir(*ppz*)$_3$ suffers from significant nonradiative loss via the ^{3}MC state, leading to Φ_{PL} = 0 % at room temperature. Ir(*pmb*)$_3$ has a similarly small E_a = 0.2 eV due to the very high E_T = 3.3 eV, although the complex has a fairly high thermal energy threshold to access the ^{3}MC state. Since there is negligible energy required for the transition between the ^{3}MC and TBP states, the excited state occupying the TBP state can transfer back to the more stabilized T_1 state and participate in the radiative recombination. As a result, Ir(*pmb*)$_3$ attains Φ_{PL} = 37 ± 5 % in violet.

To raise the nonradiative ^{3}MC state so that it is thermally inaccessible from the emissive excited state, one can employ ligands that form a strong metal-ligand bond with the Ir (III) ion so that its σ*-antibonding orbitals comprising the ^{3}MC state are destabilized. The NHC ligand used in Ir(*pmb*)$_3$ is a good candidate because it renders a strong and short metal-ligand bond, as well as has a high energy gap for deep blue emission.

2.3.3. Facial and meridional isomers of the Ir(III) organometallic complex

Tris-cyclometalated Ir (III) complexes, Ir(C^N)$_3$, have two types of molecular configurations, facial (*fac*-) and meridional (*mer*-) isomers. Here, the isomer refers to two or more molecules with the same molecular components that are arranged differently. The *fac*-

isomer of the pseudo-octahedral Ir(C^N)$_3$ has three identical ligands forming the face of an octahedron as shown in **Figure 2.13**. The *mer*-isomer has the three identical ligands arranged to form the meridian of the octahedron. Thus, a *fac*-isomer has the C_3 symmetry that is indistinguishable from the original by 360^o/3 rotation, while a *mer*-isomer is asymmetric (i.e. C_1) by the rotation.

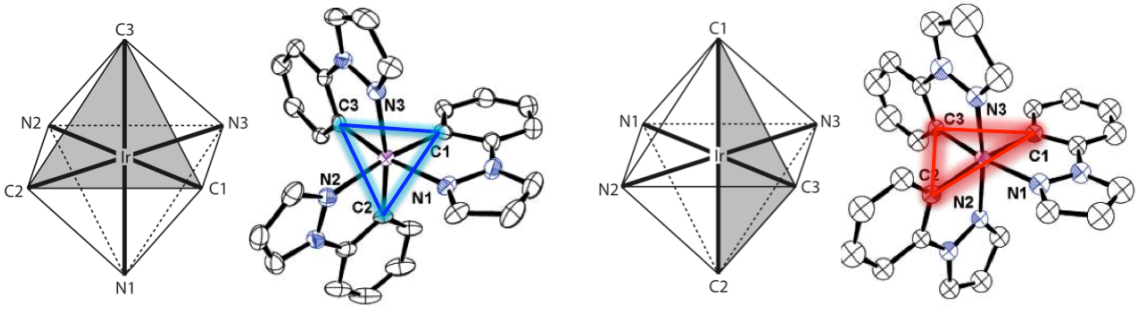

Figure 2.13 Crystal structures of facial (*fac*-) and meridional (*mer*-) isomers of Ir(*ppz*)$_3$. Note that ligands in the *fac*- or *mer*-isomers of the pseudo-octahedral Ir (III) complex form one face or a meridian of the octahedron, respectively. ORTEP drawings obtained from Ref. [81].

The difference in molecular arrangement between *fac*- and *mer*-isomers leads to the disparity in the electron distribution of their molecular orbitals. Thus, *fac*- and *mer*-isomers have distinctive energetics, electrochemical and photophysical characteristics. In the synthetic processes of the coordination between the iridium (III) and the cyclometalating ligands, *fac*-isomers are obtained at a high temperature (>200^{o}C) compared with *mer*-isomers [81]. This indicates that the *fac*-isomer is more thermodynamically stable. Tamayo *et al*. demonstrated the *mer*-to-*fac* conversion by applying high temperature or high energy UV irradiation to the *mer*-isomer [81]. This process involves the dissociation of the Ir-ligand bond of the *mer*-isomer and recoordination of the complex into the facial configuration.

Due to the reduced energy gap, *mer*-isomer exhibits red-shifted luminescent spectrum compared to that of the *fac*-isomer. Also, due to the more distributed and distorted excited state of the *mer*-isomer, the luminescence spectrum appears broader and featureless compared to vibrationally resolved and narrow spectrum for the *fac*-isomer. Finally, due to the lengthened Ir–C bonds comprising the HOMO and thus the excited state, the ^{3}MC state of the *mer*-isomer is lowered, leading to the significant nonradiative loss. As a result, *mer*-isomers of the conventional red and green Ir(C^N)$_3$ have at least a tenfold smaller PL quantum efficiency than their *fac*-counterparts.

Chapter 3 Phosphorescent organic light-emitting concentrator

3.1. Introduction to phosphorescent organic light-emitting concentrator

Recently, PHOLEDs are finding applications in solid-state lighting due to their color tunability and potentially low cost [90]. For use in general lighting, however, PHOLEDs must operate at a higher luminance (>3,000 cd/m^2) than in displays. To obtain this level of brightness, current densities >1 mA/cm^2 are required, which can lead to a reduced device lifetime and efficiency [33], [52]. Moreover, to obtain a desirable light distribution profile for uniform surface illumination, additional optical lighting source solutions [91]–[93] are required that often increase the cost and complexity of the fixture. In this chapter, we demonstrate an application that can provide solutions to both problems: a newly designed PHOLED luminaire, called a concentrator, achieves highly concentrated electroluminescence and a pattern of its emission provides uniform surface illumination. The concentrator is comprised of four triangular PHOLED panels that are assembled into a pyramidal structure, whose open base forms the emission aperture. The reflective PHOLED panels of the concentrator serve both as the light source and the reflector, confining the emitted light into the structure. Ultimately, the concentrated emission is directed toward the aperture. Since the emissive area is larger than that of the aperture, the luminance is increased by approximately a factor of three compared to a conventional device with the same area as the aperture. The far-field intensity profile of the concentrator exhibits a “batwing” distribution desirable in many illumination applications. The

directionality of the emission from the comprising PHOLEDs determines the radiation pattern of the concentrator, and also affects the degree of concentration.

3.2. Experimental methods

An illustration of the concentrator with a structure of the comprising PHOLEDs is shown in **Figure 3.1**. Four PHOLEDs are grown on triangular, indium tin oxide (ITO)-coated polyethylene terephthalate (PET) substrates (Sigma Aldrich) and they are attached to metal plates having the same shape and size as the devices. Each panel, combining the device and the plate as shown in **Fig. 3.1 (c)**, is then assembled into a pyramidal structure with an apex angle of 15.5°.

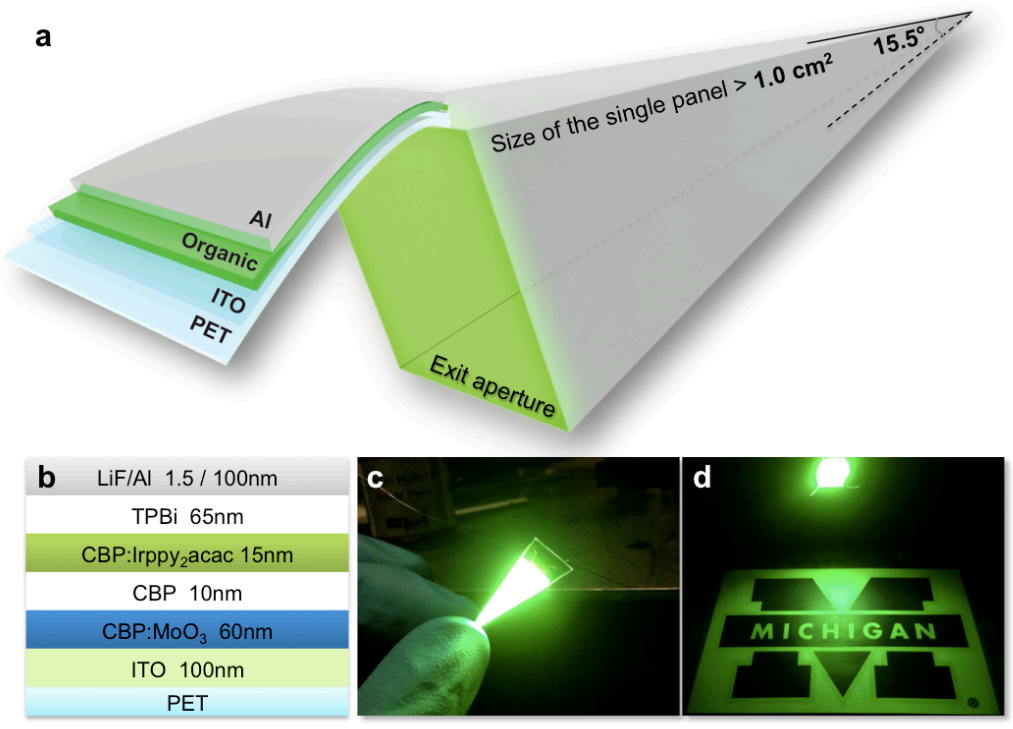

Figure 3.1 Illustration of concentrator. (a) Configuration of PHOLED panels comprising the concentrator. (b) The Green PHOLED structure. (c) Photographs showing the emission from a single panel PHOLED and (d) from a four-sided concentrator.

The emissive (or substrate) side of the PHOLED faces inwards so that the light emission from one panel is reflected by adjacent or opposing devices, and is eventually directed towards the exit aperture (see **Fig. 3.1 (d)**). PHOLEDs were grown by vacuum sublimation at a base pressure $<5\times10^{-7}$ Torr on ITO-coated plastic substrates. The substrate has the sheet resistance of 60 Ω/□ and the transmittance of >79% at a wavelength of λ=550 nm. The device structure is as follows: ITO (100 nm)/MoO_x doped at 15 vol. % in 4, 4'-bis(carbazol-9- yl)biphenyl (CBP) as a hole injection layer [94], [95] (HIL, 60 nm)/CBP as the HTL (10 nm)/bis(2-phenylpyridine) (acetylacetonate) iridium(III) (Ir(*ppy*)$_2$(*acac*)) doped at 8 vol. % in CBP as the EML (15 nm)/2,2',2''-(1,3,5-benzinetriyl)-tris(1-phenyl-1- H-benzimidazole) (TPBi) as the HBL and ETL [43] (65 nm)/LiF (1.5 nm)/ Al (cathode, 100 nm). The area of the reference PHOLED and one triangular panel of the concentrator were 1 cm^2 and 1.85 cm^2 (resulting in a total concentrator interior area of 7.4 cm^2), respectively. Prior to deposition, particulates remaining on the solvent-cleaned substrates were removed by CO_2 snow-cleaning to minimize electrical shorts [96]. PHOLED electroluminescence characteristics were measured by a parameter analyzer and a calibrated Si-photodiode whose area is larger than that of the concentrator aperture [97].

3.3. Results and Discussion

The concentration factor (CF) is defined as the ratio of the luminous flux of the concentrator measured at the exit aperture to that of the planar PHOLED as a reference with the same area as the aperture:

$$CF(J) = \frac{\sum_{i=1}^{4} L_{side,i}(J) \times A_{side}}{L_{ref}(J) \times A_{ref}}. \quad (3.1)$$

Here, $L_{\text{side,i}}$ and L_{ref} are the luminance from the single panel of the concentrator and the reference device with the areas of A_{side} and A_{ref}, respectively, measured at current density, J. Further, we define $L_{eff} = \sum_{i=1}^{4} L_{side,i} \cdot \left(A_{side} / A_{ref} \right)$ as the effective luminance of the concentrator emitted at the aperture compared with the reference.

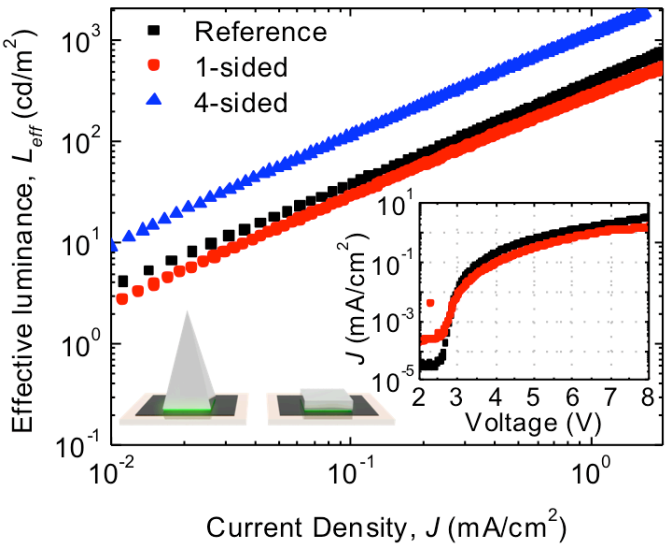

Figure 3.2 Effective luminance vs. current density of concentrator. Data for the reference device (squares), a single panel device (circles), and the four-sided device forming the concentrator are included. Inset: current density vs. voltage characteristics of the reference device and a single-panel PHOLED.

Figure 3.2 shows the L_{eff} -J characteristics of the reference, a single panel device with the other panels turned off, and from all four panels forming the concentrator. The J-V characteristics (inset) indicate that the panel device operates at a higher voltage than the reference, which is primarily a result of increased lateral resistance of ITO with device area [98], [99]. Although the single panel device has lower L_{eff} than the reference due to losses from reflections inside the concentrator, the integrated L_{eff} from the concentrator substantially exceeds

that from the reference. As a result, CF = 2.5 to 3.1 at current densities from 0.01 to 1 mA/cm^2, as shown in **Figure 3.3**.

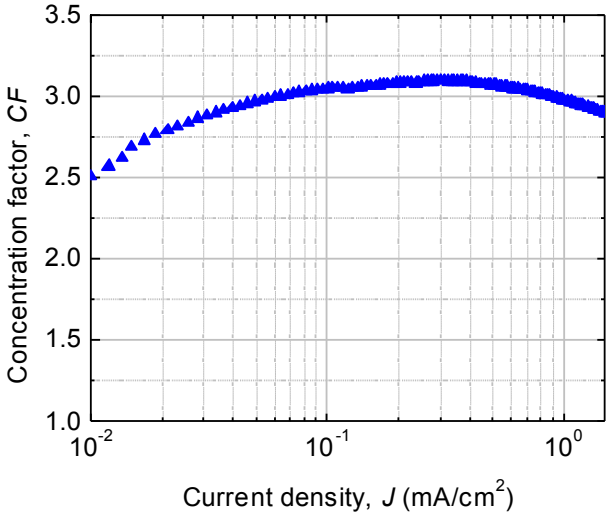

Figure 3.3 Concentration factor vs. current density of concentrator.

Given that the area ratio is 7.4, the loss in the concentrator is approximately 60 %, yet this is partially compensated by the higher brightness at the aperture.

To investigate the effect of geometry on CF, we rewrite **Eq. (3.1)** as:

$$CF(J) = 4 \cdot G\left(\theta_{apex}\right) \cdot \eta_{ext}\left(J, G\left(\theta_{apex}\right)\right). \tag{3.2}$$

where $G\left(\theta_{apex}\right) = 1/4 \cdot \csc\left(\theta_{apex}/2\right)$ is the geometric areal ratio between the single concentrator panel and the aperture as a function of apex angle, θ_{apex}. Also, $\eta_{ext}\left(J, G\left(\theta_{apex}\right)\right)$ is the geometric extraction efficiency measured by comparing the luminance of the single panel concentrator device vs. the reference at J.

Now:

$$\eta_{ext}\left(J,G\left(\theta_{apex}\right)\right)=\frac{\int_S I(s)\cdot\left\{R\left(\theta_{apex}\right)\right\}^{N_{ds}}ds}{\int_S I(s)ds}, \tag{3.3}$$

where $I(s)$ is the initial luminance emitted by an area segment, ds, of the single panel device with a total area of S, $R(\theta_{apex})$ is the reflectance of the PHOLED and N_{ds} is the number of reflections for a ray from ds to reach the aperture as discussed below.

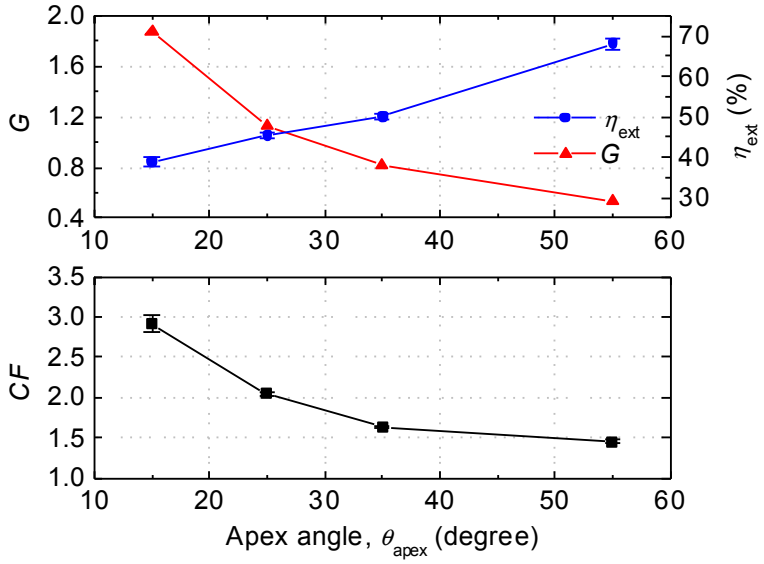

Figure 3.4 Figures-of-merit of concentrator as a function of its apex angle. (Top) Geometric area ratio (G), extraction efficiency (η_{ext}) and (Bottom) CF vs. apex angle (θ_{apex}) at J = 10 mA/cm^2 for concentrators with θ_{apex} values of 15.5, 25.5, 35.5, 55.5°. Note that CF increases monotonically as θ_{apex} decreases due to the increased number of reflections compared to concentrators with large θ_{apex} values. At the same time, η_{ext} decreases due to the increased propagation losses.

Figure 3.4 shows G, η_{ext} and CF at J=1.0 mA/cm^2 as functions of four different θ_{apex} and a fixed aperture area of 1.0 cm^2. As θ_{apex} is decreased from 55.5^o to 15.5°, η_{ext} decreases from 68 ± 2 % to 39 ± 1 % due to the increased number of reflections. This suggests that utilization of the

effective area that contributes to the output luminance decreases with θ_{apex}. Nonetheless, *CF* increases from 1.46 ± 0.03 to 2.92 ± 0.10 due to the dramatic increase of *G*. **Table 3.1** gives values for *CF* and η_{ext} at $J = 1.0$ mA/cm^2 for these devices.

Table 3.1 Concentration factor and geometric extraction efficiency vs. apex angle. These factors are obtained at a current density of $J = 1.0$ mA/cm^2

θ_{apex}	15.5°	25.5°	35.5°	55.5°
CF	2.9 ± 0.1	2.05 ± 0.03	1.64 ± 0.02	1.46 ± 0.03
η_{ext} (%)	39 ± 1	46 ± 1	50 ± 1	68 ± 2

Figure 3.5 (a) shows the normalized luminous intensity of the concentrator with respect to the reference as a function of viewing angle, ϕ, measured in the direction parallel to the side (denoted as horizontal) and along the diagonal of the aperture. While the reference is approximately a Lambertian source, the concentrator exhibits a batwing intensity profile where the intensity at viewing angles from ϕ=40 to 50° relative to the aperture normal is larger than along the central axis of the concentrator. The resultant illuminance distribution [100] is given by:

$$I(\phi) = \frac{L(\phi)}{h^2}\cos^3\phi \ , \tag{3.4}$$

at ϕ and distance, *h*, from the concentrator to illuminated area. For arbitrary *h*, the concentrator produces nearly uniform surface illumination over $\Delta\phi = \pm 40°$, while the reference has peak illuminance at $\phi = 0°$ and decreases dramatically with ϕ, as shown in **Fig. 3.5 (b)**. When installed overhead, the intensity profile of the concentrator, unlike the reference, avoids strong veiling reflections from the illuminated surface that results from intense downward emission at low ϕ.

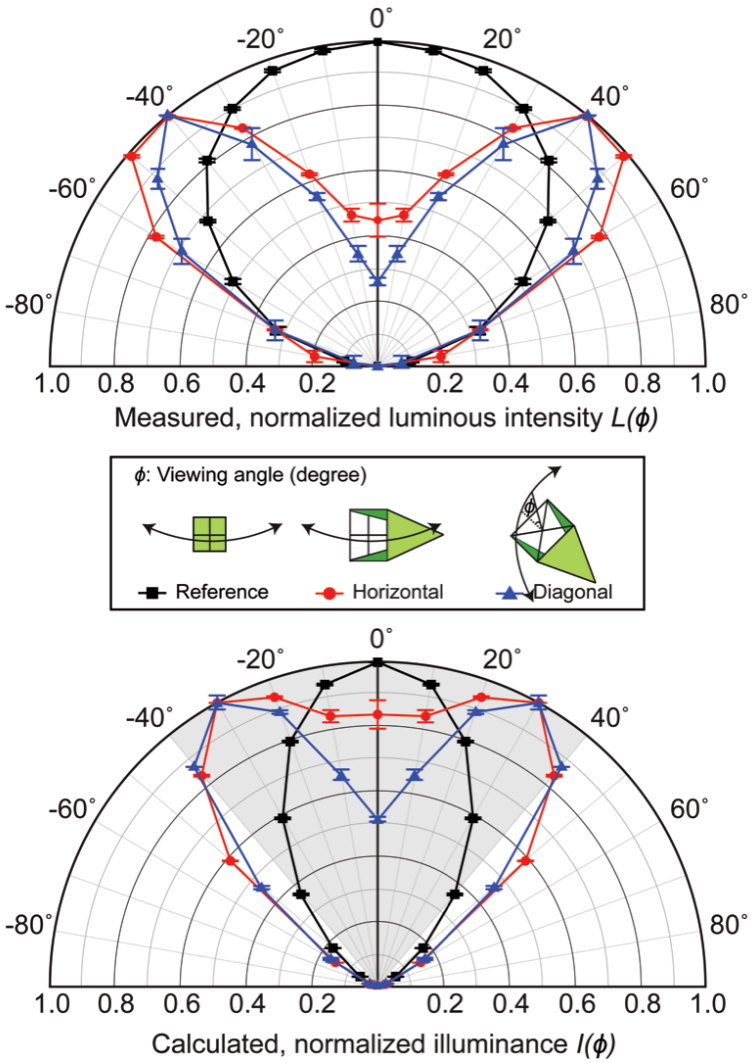

Figure 3.5 Normalized luminous intensity and illuminance of concentrator. (a) Normalized luminous intensity, $L(\phi)$, in polar coordinates vs. the viewing angle, ϕ. Also shown in an illustration of the directions along which the intensity profiles of devices were measured. (b) Calculated illuminance, $I(\phi)$, of the concentrator with respect to the reference measured in the direction parallel to the side (denoted as horizontal) and along the diagonal of the aperture. The shaded area indicates the zone of nearly uniform illumination achieved by the concentrator along the horizontal axis.

We used a ray-tracing algorithm to model the angular distribution profile of the luminaire, and to determine N_{ds} in **Eq. (3.3)**. The simulation generates the extraction efficiency, η_{ext_x}, of the rays emitted at distance, x, from the vertex of the concentrator, the intensity-weighted average

number of reflections, $\bar{N}$, required to reach the aperture, and their intensity-weighted average exit angles, $\bar{\alpha}_{exit}$, relative to the concentrator central axis. Each property for two different PHOLED reflectances, R_{PHOLED}, is provided in **Table 3.2**, with details of the algorithm and assumptions used found in **Appendix A**.

Table 3.2 Simulated characteristics of exiting rays from the PHOLED concentrator. Extraction efficiency ($\eta_{\mathrm{ext,x}}$), average intensity-weighted reflections ($\bar{N}$) and exit angles ($\bar{\alpha}_{exit}$) of the exiting rays for two values for PHOLED reflection (R_{PHOLED}) vs. the relative position of the emission (x) from the apex are calculated.

Position, x	R_{PHOLED} [%]	0	0.1	0.2	…	0.8	0.9	1.0
$\eta_{\mathrm{ext,x}}$	66	14 %	16 %	18 %	…	43 %	54 %	69 %
	71	19 %	20 %	23 %	…	48 %	57 %	71 %
$\bar{N}$	66	3.6	3.4	3.2	…	1.3	0.8	0.3
	71	3.9	3.7	3.4	…	1.5	0.9	0.4
$\bar{\alpha}_{exit}$	66	1.2°	0.6°	0.5°	…	29°	39°	51°
	71	1.1°	0.6°	0.5°	…	30°	39°	51°

* Concentrator height is assumed to be unity and the device reflectance is assumed to be invariant to the incident angle.

Emission originating near to the vertex is strongly attenuated due to high N_{ds}, and hence does not contribute significantly to the exit luminance. In addition, $\bar{\alpha}_{exit}$ of such rays are low, which is responsible for the relatively weak intensity along the central axis (c.f. **Fig. 3.5**). On the other hand, rays emitted near the aperture escape with fewer reflections, and their $\bar{\alpha}_{exit}$ is distributed across a range from only 30° to 50°, corresponding to the high intensity peak near 40° observed in the profile. Note that a primary factor that determines $\bar{\alpha}_{exit}$ and the resultant batwing distribution is the Lambertian emission distribution of the panels, while the reflectance of the device determines $\eta_{\mathrm{ext}x}$ (**Table 3.2**). Hence, we infer that the desired emission profile of the

concentrator is achieved by tailoring the profiles of its component PHOLEDs. For example, if the PHOLEDs in the concentrator have relatively intense emission at high angles by using, for example, microlens arrays [101] or a grating [102] embedded in the substrate, the emission can be extracted with a lower $\bar{N}$ at smaller $\bar{\alpha}_{exit}$, which results in directed or spot illumination profiles.

The geometry of the concentrator also affects its emission profile. The concentrator with a larger aperture (or θ_{apex}) can produce a higher luminous flux at low $\bar{\alpha}_{exit}$ than that with a smaller aperture, since the rays emitted near the vertex experience fewer reflections with an enlarged escape cone as shown in **Fig. 3.6**.

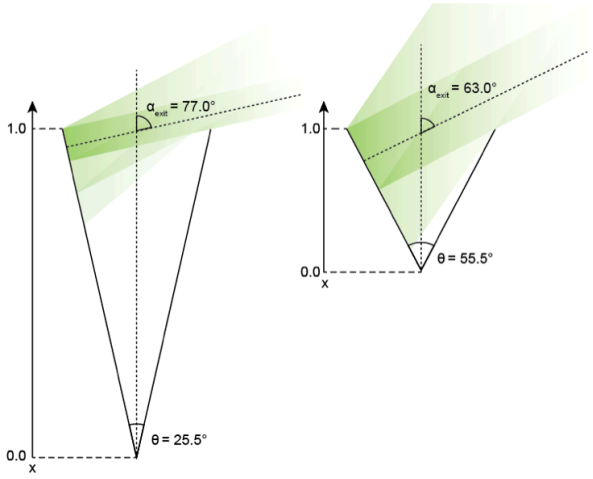

Figure 3.6 Exit angles (α_{exit}) of emission normal to the concentrator panel. Concentrators with different apex angles, θ = 25.5° and 55.5°, are compared.

Additionally, if the side panel angle is large, its emission near the aperture exits at smaller $\bar{\alpha}_{exit}$, while increasing the total η_{ext}. However, this configuration has a correspondingly decreased geometric areal ratio, leading to a reduced *CF* (see **Fig. 3.4**).

An effective means for enhancing both η_{ext} and CF independent of geometry is to increase the PHOLED reflectance, R_{PHOLED}. The PHOLED forms a weak microcavity [103] where R_{PHOLED} is determined by the reflection, transmission and interference occurring inside the organic thin films and the metal cathode. **Figures 3.7 (a)** and **(b)** show R_{PHOLED} as a function of incident angle, θ_{inc} and wavelength, λ calculated for PHOLEDs using Al (denoted as Device A) or Ag (Device B) as the cathode metal, respectively (**Appendix A**).

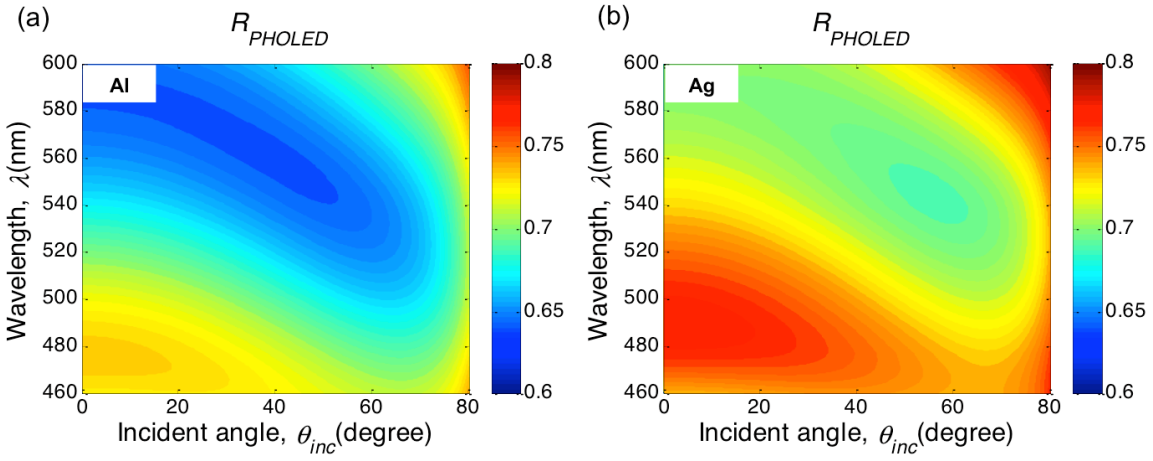

Figure 3.7 Calculated reflectance of the PHOLED using (a) aluminum or (b) silver cathode. Average of the transverse electric and magnetic mode reflectance values of a PHOLED (R_{PHOLED}, z-scale) is obtained as a function of the wavelength λ and the angle of incident light, θ_{inc}, relative to the surface normal of the PHOLED. Here, the reflectance values range from 60 to 80%, as denoted by the blue to red color scale on the right of each contour plot.

Since the PHOLED emission is unpolarized [104], its total reflectance is obtained from the average of the transverse electric and magnetic mode reflectances at wavelengths from λ = 460 to 600 nm, corresponding to 90 % of the spectral emission from the green PHOLED, and at incident angles from θ_{inc} = 0 to 80°. At θ_{inc} > 80°, most emission for both devices is reflected by the PET substrate. The reflectance of Device A varies from 64.2 ± 1.3 % to 76.3 ± 1.2 %,

compared with that of the Device B which varies from 69.2 ± 0.6 % to 79.9 ± 2.2% (Error is based on the 10% variation of the total thickness of the organic layers). Since Ag has a smaller extinction coefficient than Al, Device B is correspondingly less absorbing and has a higher R_{PHOLED} as shown in **Fig. 3.7**, leading to an increased η_{ext} from the concentrator (**Table 3.2**).

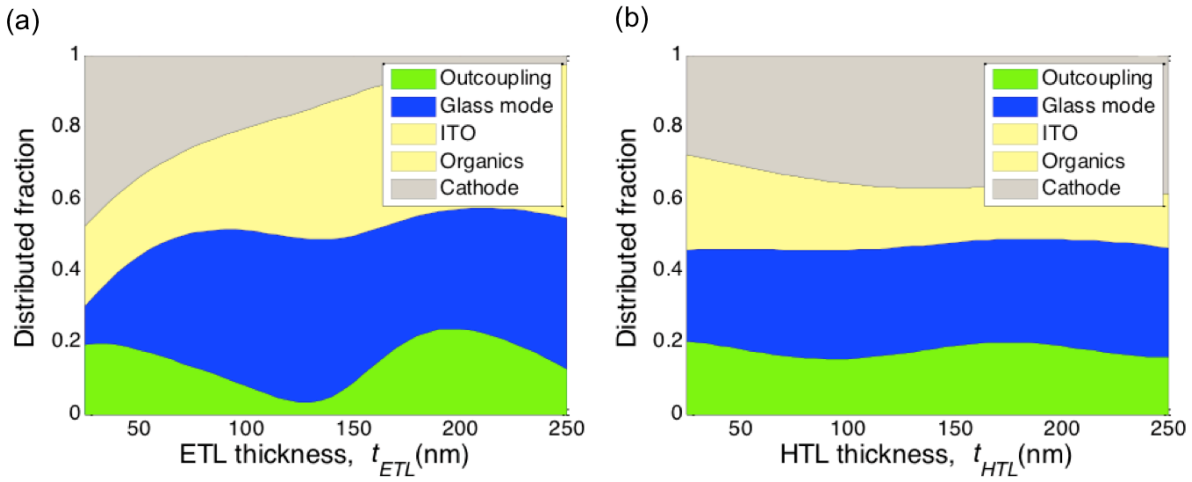

Figure 3.8 Calculated outcoupling efficiency of green PHOLED. Each fraction coupled to air modes (outcoupling), glass modes, waveguide modes (ITO and organics) and the cathode, is calculated from the relative energy transferred from the dipoles [105] at wavelength λ = 522 nm and at an emission angle normal to the layers. Here, we assume that the dipole is formed at the interface between EML and HBL. The thickness are varied for the (a) ETL (t_{ETL}), (b) HTL (t_{HTL}). The device structure used in the calculation is: ITO (100 nm) / 15 vol% MoO_x doped in CBP (t_{HTL} nm) / CBP (10 nm) / 8 vol% Ir(*ppy*)$_2$(*acac*) doped in CBP (15 nm) / TPBi (10 nm) / 2 vol% Li doped in Bphen (t_{ETL} nm) / LiQ (1.5 nm) / Ag (150 nm). The refractive indices of the organic layers are measured by variable angle spectroscopic ellipsometer.

Note that the high R_{PHOLED} contours in **Fig. 3.7** can be spectrally shifted to the PHOLED emission maximum by tuning the thickness of the ETL and/or the HTL. However, the outcoupling efficiency of the PHOLEDs, which contributes to the total luminous flux of the concentrator, is also dependent on the properties of the microcavity formed between the emission

zone and the cathode. Therefore, R_{PHOLED} can be modified by varying the HTL thickness without significantly changing its outcoupling efficiency as shown in **Fig. 3.8**.

Finally, the fraction of incident light that is not reflected is primarily absorbed by the ITO and the cathode. For example, at normal incidence at λ = 522 nm where the PHOLED emission peaks, ITO and Al in Device A absorbs 20.0 ± 1.2 % and 10.1 ± 0.8 % of the light, while the ITO and Ag absorption in Device B are 19.7 ± 1.7 % and 5.1 ± 0.2 %, respectively, considering 10% variation in thickness of organic layers.

3.4. Conclusions

We demonstrate concentrated PHOLED emission from a pyramid-shaped luminaire. By increasing the area of the side of the concentrator, a high concentration factor is achieved at the expense of the geometric extraction efficiency due to increased reflections from the surfaces of the devices comprising the edge of the luminaire. To achieve efficient extraction and high *CF*, increasing the cathode reflectivity is an effective means to increase the device external luminance efficiency. We observe that the angular intensity profile of the luminaire follows a batwing distribution, making it suitable for uniform downward illumination of surfaces. These principles of the concentrator can be generally applied to any color of light (R, G, B or W), which diversifies its usage in lighting; however to obtain desirable white color from the concentrator, the original spectrum of its component PHOLEDs should be tuned by adjusting the microcavity condition, or the thickness of the organic layers, considering the different PHOLED reflectance with respect to the wavelength. We also note that while a pyramid shape is used in our demonstration, different concentration factors and emission profiles can be achieved employing other geometries using this same general design concept. For example, parabolic or

compound parabolic concentrator shapes show promise for achieving *CF* as high as 7, and may provide aesthetic advantages over the current design. Hence, the method of concentrating emission demonstrated here can be advantageously realized in many practical, high intensity OLED-based luminaire configurations.

Chapter 4 High brightness deep blue PHOLEDs

4.1. Introduction to deep blue PHOLEDs

A driving force behind the use of organic electroluminescence in displays and lighting has been the introduction of long-lived red and green electrophosphorescent devices with up to 100% IQE [30], [41]. However, achieving deep blue electrophosphorescence with high efficiency and luminance, and long-term operational stability remains a significant challenge [33]. The design of robust and efficient blue phosphors free of electrochemically reactive moieties offers one possible solution. For example, the thermodynamically stable NHC ligands [106], [107] were used in saturated blue emitting tris-cyclometalated iridium (III) complexes [Ir(C^C:)$_3$] [108]. This is compared with blue Ir complexes using fluorination to obtain a wide energy gap (see **§2.3**), which has resulted in high efficiency but only an unsaturated sky-blue color unsuitable for displays and chemical instability.

Unfortunately, a significant drawback of previously demonstrated deep blue PHOLEDs is that they are subject to a pronounced efficiency roll-off at high luminance required in most display and lighting applications [109]–[117]. For example, the current density at the half maximum EQE, $J_{1/2}$, is typically <50 mA/cm^2 due to the loss of excitons and electrons from the PHOLED EML, as well as strong bimolecular annihilation [39]. Thus, they barely achieve a brightness > 3,000 cd/m^2 at $J_{1/2}$ or even higher current densities. Up to the present work, preventing these parasitic effects has been exacerbated by the lack of exciton and charge

blocking layers that are compatible with the high energy-triplet emitters required for deep blue emission.

Based on our understanding of the unique energetics of the NHC ligand-based Ir(C^C:)$_3$ complexes, we introduce a device design that significantly improves the efficiency of the deep blue PHOLEDs especially at high luminance. Here, Ir(C^C:)$_3$ complexes are used as the phosphorescent emitting molecules, electron/exciton blocking layers (EBL) and dopants that conduct holes across the EML. The combined effects of these multiple uses lead to a marked improvement in EQE at high current densities. Specifically, $J_{1/2}$ is increased in devices with an EBL by more than a factor of 280 compared to those without it, and is improved by an additional 50% (resulting in a cumulative improvement by a factor of 420) by grading the dopant across the EML, thereby reducing triplet annihilation losses at very high brightness [50], [118].

fac- and *mer*-Ir(C^C:)$_3$-based PHOLEDs exhibit CIE coordinates of (0.16, 0.09) and (0.16, 0.15), with maximum EQE = 10.1 ± 0.2 and 14.4 ± 0.4 % at low luminance, decreasing slightly to 9.0 ± 0.1 and 13.3 ± 0.1 % at L = 1,000 cd/m^2. Surprisingly, the *fac*- or *mer*-Ir(C^C:)$_3$-based devices attain unusually high luminance, i.e. L = 7,800 ± 400 and 22,000 ± 1000 cd/m^2 at their $J_{1/2}$ = 160 ± 10 and 210 ± 10 mA/cm^2, respectively. These devices produce unparalleled luminance at $J_{1/2}$ compared with the PHOLEDs with similar color coordinates [117], [119]. To our knowledge, the *fac*-isomer-based device achieves the brightest deep blue emission among the PHOLEDs reported to date, which almost meets sRGB requirement.

An additional finding is that the *mer*-Ir(C^C:)$_3$ is equally or more efficiently luminescent than the *fac*-isomer in solution and the solid-state [120], while conventional red and green-emitting Ir(C^N)$_3$ complexes follow the opposite trend, i.e. *fac* is more efficient than *mer* [121], [122]. We find that the strong Ir-NHC ligand bonds [106] in Ir(C^C:)$_3$ result in reduced

nonradiative decay via the ^{3}MC states for both isomers [89]. Our studies of the photophysics of Ir(C^C:)$_3$ complexes along with their employment in proposed device architectures provides a solution for achieving efficient deep blue emission at very high brightness.

4.2. Experimental methods

4.2.1. Cyclic voltammetry

Cyclic voltammetry and differential pulsed voltammetry were performed using a VersaSTAT 3 potentiostat. Anhydrous DMF (Sigma Aldrich) was used as the solvent under inert atmosphere, and 0.1 M tetra(n-butyl)ammonium hexafluorophosphate (TBAF) was used as the supporting electrolyte. A glassy carbon rod was used as the working electrode, a Pt wire was used as the counter electrode, and a Ag wire was used as a pseudo-reference electrode. The redox potentials are based on values measured from differential pulsed voltammetry and are reported relative to a ferrocene/ferrocenium (Cp_2Fe/Cp_2Fe^+) redox couple used as an internal reference.

4.2.2. Device fabrication and characterization

PHOLEDs were grown on pre-cleaned glass substrates coated with 80 nm-thick ITO by vacuum thermal evaporation in a chamber with a base pressure 6×10^{-7} torr. The devices consist of 10 nm MoO_3 doped at 15 vol% in 9-(4-tert-butylphenyl)-3,6-bis(triphenylsilyl)-9H-carbazole (CzSi) as a HIL / 5 nm CzSi HTL / 5 nm Ir(C^C:)$_3$-based EBL / 40 nm Ir(*pmp*)$_3$ doped in TSPO1 to form the EML / 5 nm TSPO1 HBL / 30 nm TPBi ETL / 1.5 nm 8-hydroxyquinolinolato-Li (Liq) electron injection layer (EIL) / 100 nm Al (cathode). The devices were patterned using a shadow mask with an array of circular openings resulting in contacts with a measured diameter of d = 430 μm. The standard deviation for a population of >20 devices leads

to a variation in area of ~ 2 %. The EBLs used for the *fac*- and *mer*-Ir(*pmp*)$_3$–based PHOLEDs were *fac*-Ir(*pmp*)$_3$ and *fac*-Ir(*pmb*)$_3$, respectively (see **Figure 4.1**). The current density-voltage-luminance (*J-V-L*) characteristics were measured using a parameter analyzer (HP4145, Hewlett-Packard) and a calibrated photodiode (FDS1010-CAL, Thorlab) according to standard procedures [97]. The emission spectra at J = 10 mA cm^{-2} were recorded using a calibrated spectrometer (USB4000, Ocean Optics) coupled to the device with an optical fiber.

4.2.3. Probing the recombination zone

The triplet exciton density, $N(x)$, in the EML as a function of distance, x, from the EBL/EML interface was determined by measuring the relative emission intensity from a 1.5 nm-thick "sensing" layer comprised of 5 vol% doped red-emitting phosphor, i.e., iridium (III) bis (2-phenyl quinolyl-N,C$^{2'}$) acetylacetonate (PQIr), inserted at different positions within the EML, as previously [50].

4.2.4. EQE modeling

Based on TTA and TPA dynamics, EQE vs. J is modeled using:

$$\frac{dn(x,t)}{dt} = G(x) - \gamma n^2(x,t), \tag{4.1}$$

$$\frac{dN(x,t)}{dt} = \gamma n^2(x,t) - \frac{N(x,t)}{\tau} - k_{TP} n(x,t) N(x,t) - \frac{1}{2} k_{TT} N^2(x,t) \tag{4.2}$$

where, n is the electron and N is the triplet density, $\gamma = e(\mu_n + \mu_p) / \varepsilon\varepsilon_0$ is Langevin recombination rate and μ_n, and μ_p are the respective electron and hole mobilities in the doped EML. Also, $\varepsilon = 3$ is the dielectric constant, x is position, t is time, G is the charge generation rate, and k_{TT} and k_{TP} are the TTA and TPA rates, respectively. Here, $G(x) = J_0 / e \cdot N(x) \Big/ \int_{EML} N(x)dx$,

where N is the measured recombination profile in **Figure 4.10**, different from previous assumptions based on the constant recombination zone width [39], [118]. **Eq. (4.1)** assumes that $p = n$ in the EML, and τ is obtained from the transient phosphorescence decay of Ir(pmp)$_3$ doped into TSPO1. $N(x)$ is obtained in steady state and integrated over the EML to obtain $N_{tot} = \int_{EML} N(x)dx$. Then, N_{tot}/J is normalized by the EQE value at $J = 0.1$ mA/cm^2 and fit to $J =$ 100 mA/cm^2 (**Fig. 4.14**, lines), where bimolecular quenching is active.

4.3. Material properties of deep blue-emitting Ir(*pmp*)$_3$

4.3.1. Results

The structure of our newly synthesized NHC Ir(III) complex, tris-(N-phenyl, N-methyl-pyridoimidazol-2-yl)iridium (III), Ir(pmp)$_3$, is based on the near UV-emitting tris-(N-phenyl, N-methyl-benzimidazol-2-yl) Ir (III), or Ir(pmb)$_3$, whose benzannulated component in the NHC ligands is replaced with a fused pyridyl ring as shown in **Figure 4.1**.

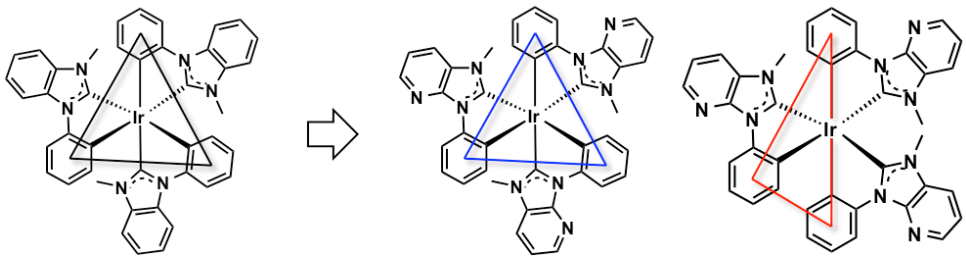

Figure 4.1 Molecular structural formulae of *fac*-Ir(pmb)$_3$, *fac*- and *mer*-Ir(pmp)$_3$. Here, *fac*- and *mer*-Ir(pmp)$_3$ have the C_3 and C_1 molecular symmetries, respectively, in pseudo-octahedral coordinates.

The greater electronegativity of the nitrogen atom vs. methine (CH) lowers the reduction potential of *fac*-Ir(*pmp*)$_3$ to $E_{red} = -2.77 \pm 0.05$ V relative to *fac*-Ir(*pmb*)$_3$ ($E_{red} = -3.19 \pm 0.05$ V), while their oxidation potentials are nearly identical (E_{ox} = 0.47 ± 0.05 and 0.45 ± 0.05 V, respectively). The absorption spectra of *fac*-Ir(*pmb*)$_3$ and *fac*-Ir(*pmp*)$_3$ in **Fig. 4.2** show that their spin-allowed ^{1}MLCT transitions have a high energy onset at λ = 350 and 380 nm, respectively. The observed red shift for the absorption spectrum of *fac*-Ir(*pmp*)$_3$ results from its smaller energy gap compared to *fac*-Ir(*pmb*)$_3$ inferred from their E_{red} and E_{ox}.

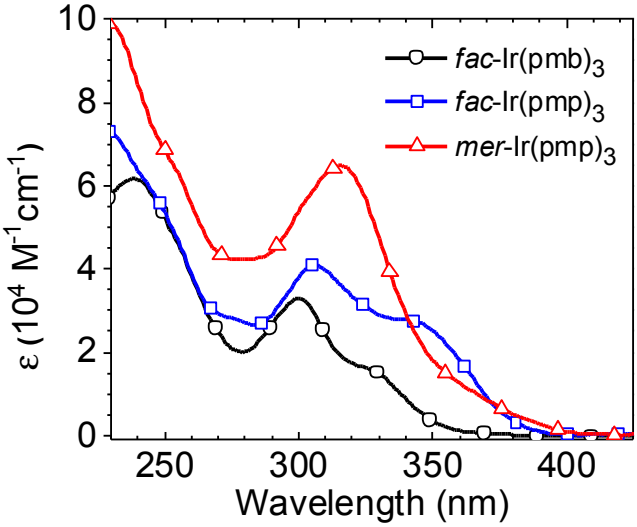

Figure 4.2 Absorption spectra of *fac*-Ir(*pmb*)$_3$, *fac*-Ir(*pmp*)$_3$ and *mer*-Ir(*pmp*)$_3$ diluted in dichloromethane.

Accordingly, the photoluminescence (PL) spectrum of the *fac*-Ir(*pmp*)$_3$ in **Figure 4.3** has a red-shifted spectrum with peak wavelength of λ_{max} = 418 nm in the deep blue compared to the near-UV emission of *fac*-Ir(*pmb*)$_3$ (λ_{max} = 380 nm) [106]. Meanwhile, the PL spectrum of *mer*-Ir(*pmp*)$_3$ is broad and displays a large room temperature bathochromic shift (λ_{max} = 465 nm) relative to the *fac*-isomer. The lower emission energy of the *mer*-Ir(*pmp*)$_3$ compared to the *fac*-isomer is due to its lower oxidation potential (E_{ox} = 0.23 ± 0.05 V) and nearly identical reduction

potentials (E_{red} = −2.80 ± 0.05 V), which result in a correspondingly reduced energy gap. The emission from both Ir(*pmp*)$_3$ isomers undergo a pronounced rigidochromic shift at T = 77 K, with the *fac*-isomer displaying a vibronically structured line shape. **Table 4.1** summarizes the reduction and oxidation potentials, and PL characteristics of *fac*-Ir(*pmb*)$_3$, *fac*- and *mer*-Ir(*pmp*)$_3$.

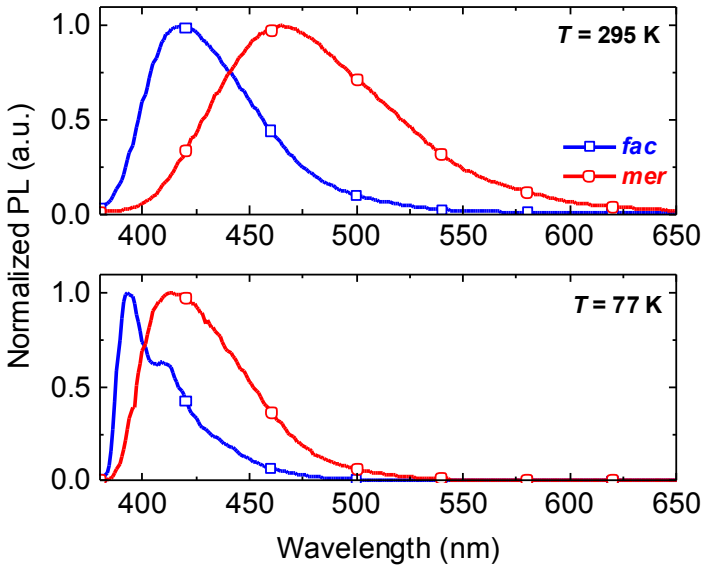

Figure 4.3 Temperature dependence of PL spectra of *fac*- and *mer*-Ir(*pmp*)$_3$. Complexes are diluted in degassed 2-methyltetrahydrofuran and their PL are obtained at temperatures of T = 295 K (top) and 77 K (bottom).

Table 4.1 Reduction and oxidation potentials of *fac*-Ir(*pmb*)$_3$, *fac*-Ir(*pmp*)$_3$ and *mer*-Ir(*pmp*)$_3$. The peak wavelength of their PL spectra are also given.

Complexes	[a]E_{ox} (V)	[a]E_{red} (V)	[b]PL λ_{peak} (E_{peak})
fac-Ir(*pmb*)$_3$	0.45 ± 0.05	-3.19 ± 0.05	380 nm (3.26 eV)
fac-Ir(*pmp*)$_3$	0.47 ± 0.05	-2.77 ± 0.05	418 nm (2.97 eV)
mer-Ir(*pmp*)$_3$	0.23 ± 0.05	-2.80 ± 0.05	465 nm (2.67 eV)

[a] Measured by cyclic voltammetry and values are determined versus Fc/Fc+. [b] Measured in degassed 2-methyltetrahydrofuran. Value in parenthesis corresponds to energy.

Figure 4.4 shows the temperature dependent transient PL characteristics of *fac*- and *mer*-Ir(*pmp*)$_3$ in de-aerated 2-methyltetrahydrofuran (2-MeTHF) with quantum yields of Φ_{PL} = 76 ± 5 and 78 ± 5% at T = 295 K [cf. Φ_{PL} of *fac*-Ir(*pmb*)$_3$ = 37 ± 5%] [89], and Φ_{PL} = 95 ± 5 % at 77 K for both isomers.

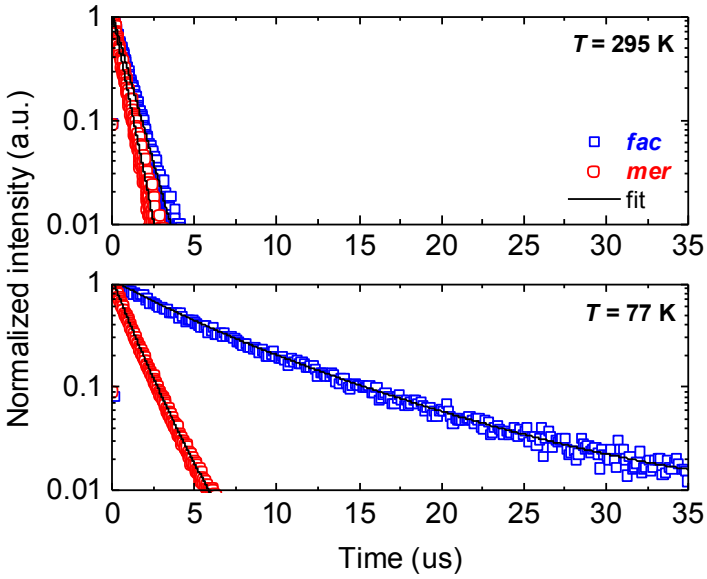

Figure 4.4 Temperature dependence of transient PL decay of *fac*- and *mer*-Ir(*pmp*)$_3$. Complexes are diluted in 2-MeTHF and their PL signals were obtained at T = 295 K (top) and 77 K (bottom), with the fits based on mono- or multi-exponential decays.

The triplet lifetimes, τ, were obtained from mono-exponential fits to the transient PL decay at room temperature. Radiative (k_r) and nonradiative (k_{nr}) rate constants are calculated using the relationship [122] $k_r = \Phi_{PL}/\tau$, where $\Phi_{PL} = k_r/(k_r + k_{nr})$. The *mer*-isomer has a shorter triplet lifetime of τ = 0.8 ± 0.1 vs. 1.2 ± 0.1 μs for the *fac*-isomer, that results in its higher k_r = (1.0 ± 0.2)×10^6 vs. (6.4 ± 1.3)×10^5 s^{-1} and k_{nr} = (2.7 ± 0.4)×10^5 vs. (2.0 ± 0.4)×10^5 s^{-1}. At T = 77 K, triplet lifetimes of *fac*-Ir(*pmp*)$_3$ were extracted from multi-exponential fits. Accordingly, *fac*-Ir(*pmp*)$_3$ has two relatively well-resolved lifetimes of τ_1 = 3.9 ± 0.2 μs (weighting: 45%) and τ_2 =

9.2 ± 0.2 μs (55%). In contrast, the *mer*-isomer still shows a mono-exponential decay with only slightly increased τ = 1.0 ± 0.1 μs at T = 77 K. **Table 4.2** summarizes the photophysical parameters of both isomers.

Table 4.2 Temperature-dependent photophysical properties of *fac*- and *mer*-Ir(*pmp*)$_3$ dispersed in degassed 2-methyltetrahydrofuran solution.

Temperature	295 K				77 K	
	Φ_{PL} (%)*	τ (μs)†	k_r (10^5 s^{-1})	k_{nr} (10^5 s^{-1})	Φ_{PL} (%)‡	τ (μs)
fac-Ir(*pmp*)$_3$	76 ± 5	1.2 ± 0.1	6.4 ± 1.3	2.0 ± 0.4	95 ± 5	3.9 ± 0.2, 9.2 ± 0.1
mer-Ir(*pmp*)$_3$	78 ± 5	0.8 ± 0.1	10 ± 2	2.7 ± 0.4	95 ± 5	1.0 ± 0.1

* Photoluminescence quantum yield (Φ_{PL}). † Mono- and multi-exponential fits are used for extracting triplet lifetimes (τ) at temperatures of T = 295 and 77 K, respectively. ‡ Calculated by referencing the integrated emission intensity to that of *fac*-Ir(*ppy*)$_3$ (Φ_{PL} = 100 %). Errors for the model parameters (k_r and k_{nr}) are the 95% confidence interval.

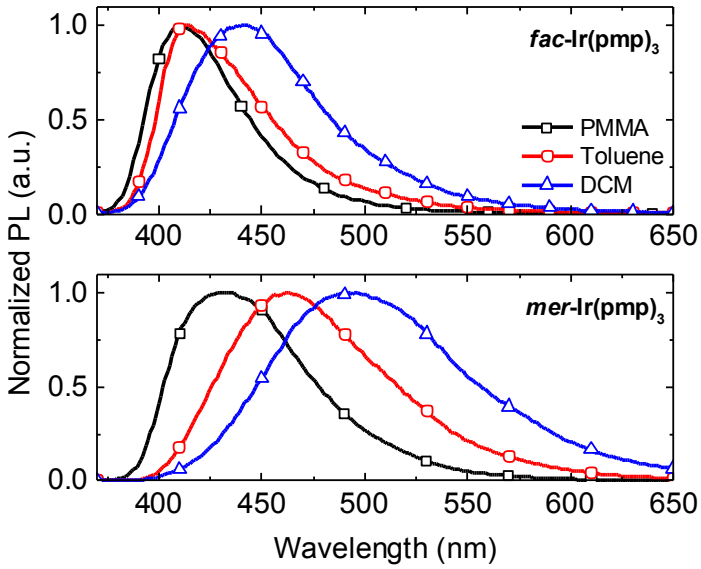

Figure 4.5 PL spectra of diluted *fac*- and *mer*-Ir(*pmp*)$_3$ in different polarity media. Media are poly(methyl methacrylate) (PMMA), toluene, and dichloromethane (DCM).

Figure 4.5 shows the PL spectra of diluted *fac*- and *mer*-Ir(*pmp*)$_3$ in different polarity media, poly(methyl methacrylate) (PMMA), toluene, and dichloromethane (DCM) having dipole moments of 0, 0.375, and 1.6 Debye [123], respectively. Both complexes exhibit positive solvatochromism (bathochromic shift) in a polar medium. Interestingly, the PL spectrum of the *mer*-isomer is more red-shifted and broadened than that of the *fac*-isomer, indicating that the excited states of the former complex are more stabilized in the similar polar solvent.

Figure 4.6 illustrates the calculated HOMO, LUMO and the spin density surfaces from the optimized triplet states for *fac*- and *mer*-Ir(*pmp*)$_3$, which were obtained from density functional theory (DFT) and time-dependent DFT calculations, respectively. Commonly, the HOMOs of both isomers are disposed on the phenyl-π and Ir-*d* orbitals, while their LUMOs are preferentially formed in the methyl-pyridoimidazole ligands [122]. The HOMO and LUMO of *fac*-Ir(*pmp*)$_3$ are equally distributed among the three ligands due to its C_3 symmetry (nearly identical LUMO, LUMO+1, LUMO+2), whereas for C_1-symmetric *mer*-Ir(*pmp*)$_3$, the phenyl π-orbitals in the two mutually trans pyridoimidazole ligands (both denoted as L) form the HOMO, and its lowest LUMO is localized in π*-orbitals in the third ligand (denoted as L' and LUMO < LUMO+1, LUMO+2). This electron configuration of the *mer*-isomer elongates its transoid Ir−C bonds that leads to the destabilized HOMO and the slightly affected LUMO [122]. The calculated HOMOs are at 5.21 eV and 5.10 eV and LUMOs of 1.27 eV and 1.20 eV from the vacuum level for *fac* and *mer*-Ir(*pmp*)$_3$, respectively. The spin density distribution of triplet states of *fac* and *mer*-Ir(*pmp*)$_3$ show that both isomers have pronounced metal-ligand charge-transfer (^{3}MLCT) character (see **Table 4.3**); however, the greatest difference between two isomers is that triplets in a *fac*-isomer are localized within a single ligand represented by intraligand-charge-transfer (ILCT) admixed with ^{3}MLCT states, whereas those in the *mer*-isomer are delocalized

across the ligands represented by combined ligand-to-ligand charge-transfer (^{3}LL'CT) and ^{3}MLCT states (see **Fig. 4.6**). From the calculated energy of the excited states, we get the singlet-triplet splitting, Δ_{ST}, of 0.22 and 0.10 eV for *fac*- and *mer*-Ir(*pmp*)$_3$, respectively.

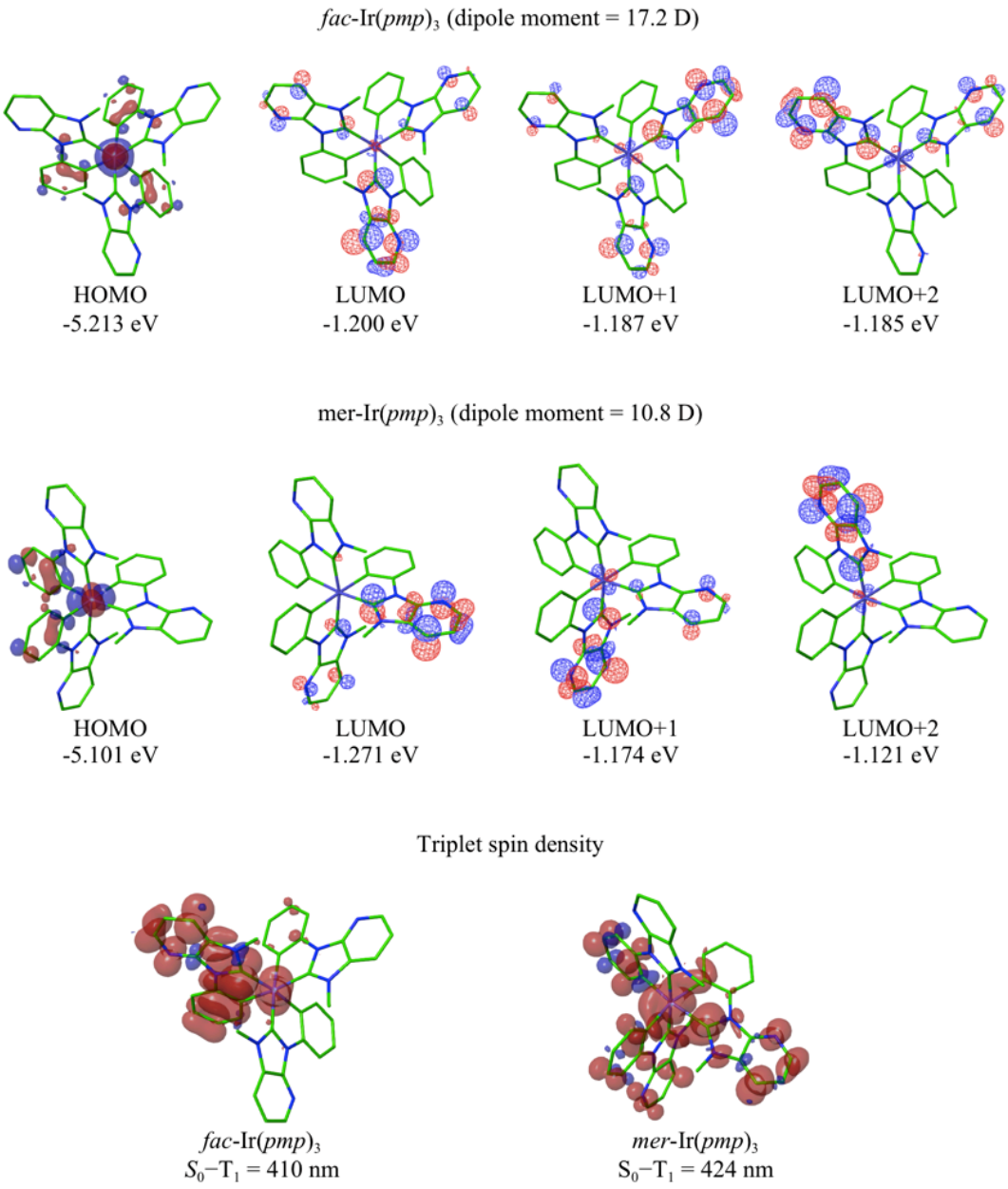

Figure 4.6 Calculated molecular orbitals diagram of *fac* and *mer*-Ir(*pmp*)$_3$. A B3LYP/LACVP** functional in a CH_2Cl_2 solvent continuum dielectric model is used for time dependent density functional theory (TD-DFT) and DFT calculations.

Table 4.3 Calculated characteristics of optical transitions in *fac*- and *mer*-Ir(*pmp*)$_3$. $S_0 \rightarrow T_1$ and $S_0 \rightarrow S_1$ transitions, energies (λ_{cal} and E_{cal}), oscillator strengths (f), orbital contributions (>10%), and assignments of *fac* and *mer*-Ir(*pmp*)$_3$ are obtained from TD-DFT calculations.

	State	λ_{cal} (E_{cal})	f	Orbital contribution	Assignment
fac-Ir(*pmp*)$_3$	T_1	390 nm (3.18 eV)	0	HOMO→LUMO (78%)	MLCT, ILCT
	S_1	365 nm (3.40 eV)	0.0427	HOMO→LUMO+1 (82%) HOMO→LUMO (14%)	MLCT, ILCT
mer-Ir(*pmp*)$_3$	T_1	396 nm (3.13 eV)	0	HOMO→LUMO (71%) HOMO→LUMO+2 (17%)	MLCT, LLCT
	S_1	384 nm (3.23 eV)	0.0035	HOMO→LUMO (98%)	MLCT, LLCT

4.3.2. Discussion

The *mer*-isomers of the conventional red and green-emitting Ir(C^N)$_3$ complexes [121], [122] typically have a nonradiative decay rate (k_{nr}) at least an order of magnitude larger than their *fac*-isomers as shown in **Table 4.4**.

Table 4.4 Photophysical characteristics of red, green and deep blue phosphors.

Emitter	†Ir(*piq*)$_3$ (red)		‡Ir(*ppy*)$_3$ (green)		Ir(*pmp*)$_3$ (blue)	
Isomer	facial	meridional	facial	meridional	facial	meridional
Φ_{PL} [%]	45	7	100	4	76	78
k_r [10^5 s^{-1}]	3.6	3.3	2.1	2.4	6.4 ± 1.3	10 ± 2
k_{nr} [10^5 s^{-1}]	4.4	42	3.2	64	2.0 ± 0.4	2.7 ± 0.4

† Tris[1-phenylisoquinolinator-C^2, N]iridium (III), ‡ Tris[2-phenylpyridinato-C^2, N]iridium (III).

This difference is attributed to a more efficient thermal population of nonradiative triplet metal-centered (^{3}MC) ligand-field states that comprise Ir–ligand antibonding orbitals in the *mer*-isomer [89], [124]. The asymmetric molecular structure (C_1) of *mer*-isomers leads to *trans*-disposed Ir–N linkages that are more labile compared to the three equivalent Ir–N bonds in the

C_3-symmetric *fac*-isomers [125]. Therefore, the ^{3}MC states of the *mer*-isomer are stabilized and thermally accessible compared to the *fac*-isomer. However, for Ir(*pmp*)$_3$, the difference in k_{nr} between *fac*- and *mer*-isomers is less than a factor of two as a result of the strong Ir–carbene bonds destabilizing the ^{3}MC states for both isomers. The lack of *mer*-to-*fac* isomerization for Ir(*pmp*)$_3$ substantiates its strong metal-ligand bond nature, while the Ir(C^N)$_3$ complexes having weaker Ir–N bonds allow such conversion [89]. At T = 77 K, the quantum yields of *fac*- and *mer*-Ir(*pmp*)$_3$ increase to near unity due to suppressed nonradiative decay via thermal population to ^{3}MC states.

The relative dominance of ligand-centered (^{3}LC) over ^{3}MLCT excited states in *fac*-Ir(*pmp*)$_3$ compared to the *mer*-isomer is reflected in the more pronounced temperature dependence of the transient PL response (**Fig. 4.4**). The broader PL spectrum both at T = 295 and 77 K, more pronounced bathochromic shift in a polar medium (**Fig. 4.5**), and rigidochromic shift in a frozen media (see **Fig. 4.3**) confirm that emission from *mer*-Ir(*pmp*)$_3$ originates more from a polar excited state (^{3}MLCT), rather than the relatively nonpolar ^{3}LC-dominant states of the *fac*-isomer [126]. The dispersed electron distribution in the *mer*-isomer as opposed to the ligand-localized condition in the *fac* configuration likely results in its higher transition dipole moment [126] (see **Fig. 4.6**). This also explains the smaller Δ_{ST}, or the electron exchange energy, for the *mer*-Ir(*pmp*)$_3$ than the *fac*-isomer (0.10 vs. 0.22 eV), because Δ_{ST} reduces with the decreased overlap and increased spatial separation between the HOMO and LUMO. **Table 4.5** summarizes the photophysical characteristics of *fac* and *mer*-isomers of Ir(*pmp*)$_3$.

Table 4.5 Photophysical characteristics of *fac* and *mer*-Ir(*pmp*)$_3$

Complex	*fac*-Ir(*pmp*)$_3$	*mer*-Ir(*pmp*)$_3$
[a] FWHM (nm)	51 ± 1	75 ± 1
[b] Solvatochrmism[†] (eV)	0.19 ± 0.01	0.33 ± 0.01
[c] Rigidochromic shift[†] (eV)	-0.19 ± 0.01	-0.34 ± 0.01

[a] Measured from the PL of the isomers doped at 1 vol% in PMMA.

[b] The value corresponds to the spectral shift of the PL peak of the isomer in DCM relative to that in PMMA.

[c] The value corresponds to the spectral shift of the PL peak of the isomer in 2-MeTHF at T = 77 K relative to that at room temperature.

[†] The positive and negative values indicate the spectral red and blue-shift, respectively.

Compared to the structurally analogous violet-emitting *fac*-Ir(*pmb*)$_3$ complex, *fac*- and *mer*-Ir(*pmp*)$_3$ achieve a higher phosphorescence efficiency of Φ_{PL} = 76 ± 5 and 78 ± 5 %, respectively, relative to 37 ± 5 % for *fac*-Ir(*pmb*)$_3$ [89]; the difference once more is due to the increased stabilization of the triplet states in Ir(*pmp*)$_3$. Another possible explanation for the enhanced Φ_{PL} is a decrease in the torsion angle between the phenyl and pyridoimidazole groups in Ir(*pmp*)$_3$ relative to Ir(*pmb*)$_3$ caused by a steric interference between the H-atoms at the 1,7 phenyl and benzimidazole group positions. Substitution of the methine (CH) for N in Ir(*pmp*)$_3$ eliminates this conflict.

4.4. Deep blue PHOLEDs based on Ir(*pmp*)$_3$

4.4.1. Results

Figure 4.7 shows the structures of PHOLEDs using *fac*- or *mer*-Ir(*pmp*)$_3$ (denoted by devices D_{fac} or D_{mer}) along with the highest occupied molecular orbital (HOMO) and lowest

unoccupied molecular orbital (LUMO) energies for all organic materials studied [12], [127], [128].

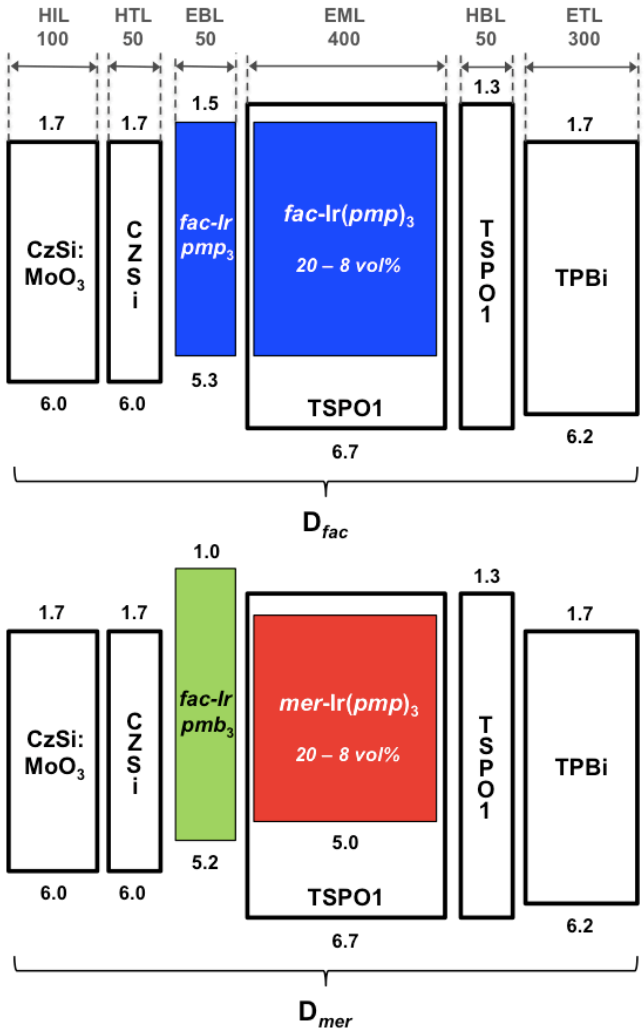

Figure 4.7 Structure and energetics of the PHOLED based on *fac*- and *mer*-Ir(*pmp*)$_3$. The former and latter devices are denoted by (a) D_{fac} and (b) D_{mer}, respectively. HOMO and LUMO energies of comprising materials in eV are either calculated or obtained from the literature [12], [128], [129].

The LUMO energies are calculated from the reported or measured E_{red} following Ref. [12]. The EBLs consist of the Ir(C^C:)$_3$ themselves [i.e. *fac*-Ir(*pmp*)$_3$ and *fac*-Ir(*pmb*)$_3$ for D_{fac} and D_{mer}, respectively] which have equal or shallower LUMO energies than that of the host, as

well as equal or larger triplet energy levels than the dopants. This enables efficient hole injection into the hole-conducting dopants, while blocking electrons transported via the host. The doping concentration in the EML is linearly graded from 20 vol% at the EBL interface to 8 vol% at the hole blocking layer (HBL) interface to create a uniform triplet distribution across the EML [50].

To investigate how injected charges in the EML are transported, we fabricate hole-only (HO) and electron-only (EO) transporting devices. HO and EO devices have the same EML with *mer*-Ir(*pmp*)$_3$ doped at different concentrations of 4, 8, and 20 vol% and other components of the respective types are chosen to conduct only holes or electrons, while blocking opposite charges. Detailed structures of HO and EO devices are as follows:

HO device – ITO (ultraviolet-ozone treated) / 10 nm CzSi:MoO_3 at 15 vol. % / 5 nm CzSi / 5 nm *fac*-Ir(*ppz*)$_3$ / 40 nm TSPO1:*mer*-Ir(*pmp*)$_3$ at 4, 8 and 20 vol. % / 5nm TSPO1 / 5 nm MoO_3 / 100 nm Al.

EO device – ITO (untreated) / 10 nm CzSi:MoO_3 at 15 vol. % / 5 nm CzSi / 5 nm *fac*-Ir(ppz)$_3$ / 40 nm TSPO1:*mer*-Ir(*pmp*)$_3$ at 4, 8 and 20 vol. % / 5nm TSPO1 / 1.5 nm Liq / 100 nm Al.

The lack of emission from both types of devices confirms negligible charges with the undesirable, opposite polarity. **Figure 4.8** shows the current density-voltage characteristics of HO and EO devices.

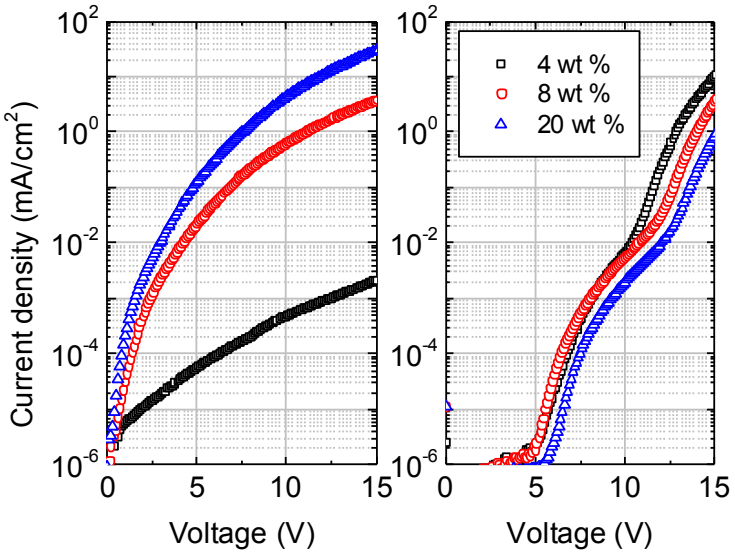

Figure 4.8 Current density-voltage characteristics of hole-only (left) and electron-only (right) devices. They have the same EML structures with different concentrations of 4, 8 and 20 vol. % (squares, circles, and triangles, respectively) of *mer*-Ir(*pmp*)$_3$.

The current density of HO device increases with the doping concentration of *mer*-Ir(*pmp*)$_3$ in the EML, whereas that of EO device is nearly independent of the concentration. This indicates that holes and electrons injected into the EML are dominantly transported by the dopant and the host (TSPO1), respectively. Due to the nested HOMO and LUMO energies of Ir(*pmp*)$_3$ in TSPO1 (**Fig. 4.7**), the majority of electrons transported via the host are trapped by the dopant and then radiatively recombine with the holes on the dopant. Since TSPO1 is preferably electron-transporting due to its diphenylphosphine oxide group [129], triplets are primarily formed at the EBL/EML interface in PHOLEDs (top, **Fig. 4.9**).

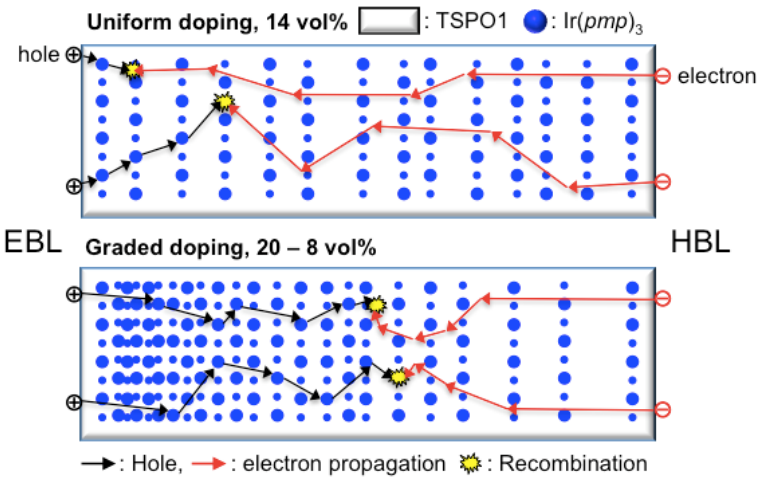

Figure 4.9 Charge-transport mechanisms in standard and graded emission layers. The standard emission layer (EML, top) is uniformly doped with Ir(*pmp*)$_3$ (blue circle) at 14 vol% into TSPO1 host (white rectangular background) and the graded EML (bottom) has linearly graded Ir(*pmp*)$_3$ at 20 – 8 vol% from the EBL to the HBL boundaries. Black and red arrows describe the hole and electron transport trajectories, respectively, which then recombine radiatively as illustrated by a yellow starburst. This conceptually demonstrates that recombination occurs relatively closer to the HBL boundary for the graded vs. uniformly doped EML due to the improved hole injection and transport of the former.

This necessitates the use of EBLs with high triplet and shallow LUMO energies as shown in **Fig. 4.7**. In the graded EML, an initially high doping concentration (20 vol%) near the EBL/EML interface facilitates hole injection and transport, which gradually reduces due to the decreasing dopant fraction (8 vol%) at the EML/HBL interface (bottom, **Fig. 4.9**). The resulting triplet exciton densities [50] (or recombination profiles) of both types of EML are shown in **Fig. 4.10**. In the uniformly doped EML, ~47 % of triplets are concentrated near the EBL/EML interface (x = 0 – 10 nm), which decreases to approximately 33 % in the graded EML due to the deeper hole penetration. The distributed recombination profile reduces the probability of bimolecular annihilation quenching [39].

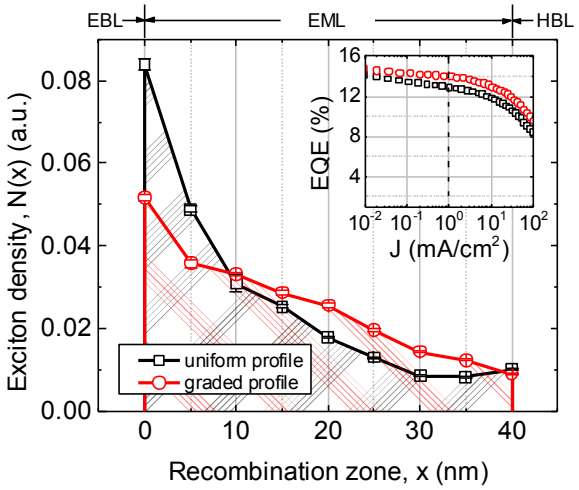

Figure 4.10 Triplet density distributions of standard and graded emission layers. The standard and graded EMLs are uniformly doped (squares) and graded (circle) with *mer*-Ir(*pmp*)$_3$, respectively, and their triplet density profiles were measured at J = 10 mA/cm^2. The EQE vs. J of PHOLEDs for both types of EML structures are compared in the inset.

In addition, radiative recombination in the graded EML device occurs farther from the EBL/EML interface compared to the uniformly doped EML PHOLED, resulting in enhanced light outcoupling.

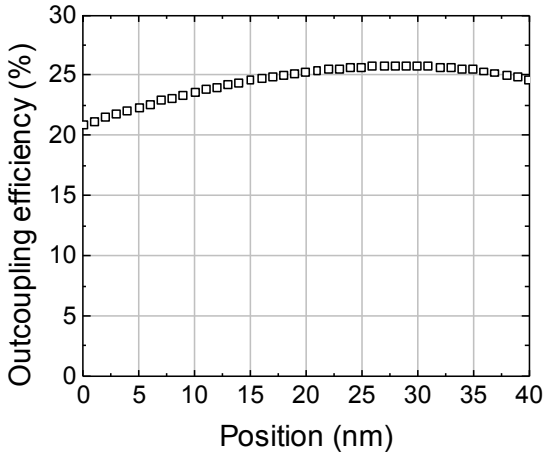

Figure 4.11 Outcoupling efficiency as a function of dipole location in the emission layer. EBL / EML and EML / HBL interfaces are at x = 0 and 40 nm, respectively.

Figure 4.11 shows the calculated energy distribution of the dipole as a function of the position in the EML following ref. [105]. Assuming a radiative triplet exciton as a point dipole, the outcoupling efficiency of the dipole closer to the EML/HBL interface (e.g. x = 30 nm) is higher than that at the EBL/EML interface (x = 0 nm). These combined effects of the high outcoupling efficiency and reduced bimolecular annihilation contribute to the increased EQE of D_{mer}, as shown in the inset of **Figure 4.10**.

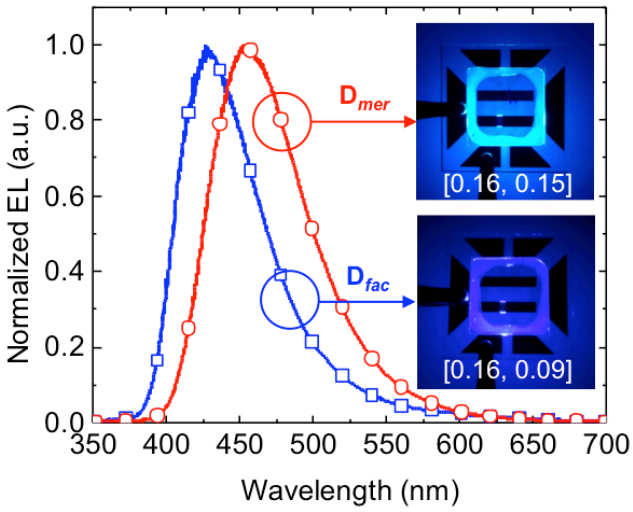

Figure 4.12 EL spectra of deep blue PHOLEDs, D_{fac} and D_{mer}. Spectra were measured at a current density of J = 10 mA/cm^2. The insets are photographs of 2 mm^2, packaged PHOLEDs whose illumination is reflected from a white background to avoid saturation of the camera sensor. The bright irregular square shape in each image is due to light scattered from the epoxy package seal. The package is a sandwich of two glass slides, one containing electrodes (dark regions) and the other serving as a lid.

Figure 4.12 shows the electroluminescence (EL) spectra of D_{fac} and D_{mer} measured at a current density of J = 10 mA/cm^2, which result in deep blue CIE coordinates of [0.16, 0.09] and [0.16, 0.15], respectively. In the inset we show images of the packaged devices along with their

characteristic emission color. The EL spectra have nearly identical CIE coordinates compared to the PL of the EML, confirming the emission solely from the dopants in the PHOLEDs.

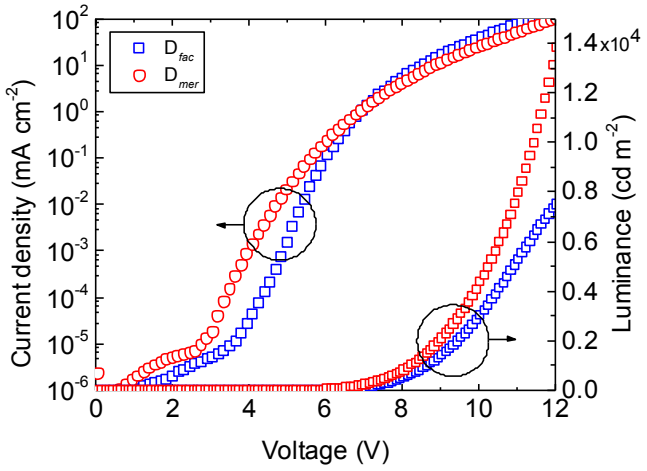

Figure 4.13 Current density-voltage-luminance characteristics of D_{fac} and D_{mer}.

Figure 4.13 shows the current density-voltage-luminance (*J*-*V*-*L*) characteristics of D_{fac} and D_{mer}. D_{mer} turns on at a lower voltage than D_{fac} (3 vs. 4 V), which is presumably due to different charge injection, transport and trapping characteristics [120], and the lower HOMO energy of *mer*-Ir(*pmp*)$_3$ than the *fac*-isomer. Although the current densities of D_{fac} at high voltage (> 7 V) are greater than those of D_{mer}, the latter device still achieves a higher luminance due to its red-shifted emission and higher EQE at all current densities. **Figure 4.14** shows the EQE-*J* characteristics of D_{fac}, D_{mer} and analogous devices whose EMLs are uniformly doped at 14 vol% by *fac* and *mer*-Ir(*pmp*)$_3$ (denoted $D_{fac,uni}$ and $D_{mer,uni}$, respectively), and a device without an Ir(C^C:)$_3$-based EBL ($D_{mer,uni,no\ EBL}$).

By employing *fac*-Ir(*pmb*)$_3$ as the EBL, the uniformly doped EML PHOLED ($D_{mer,uni}$) has a markedly higher EQE and reduced efficiency roll-off at high *J* compared to the PHOLED

lacking an EBL ($D_{mer,\text{uni,no EBL}}$). Therefore, $J_{1/2}$ increases by almost 280 times, from 0.5 ± 0.1 to 140 ± 10 mA/cm^2, and EQE increases by at least 40 % at all current densities. The EQEs of the graded-EML devices employing an EBL (D_{mer}) are further improved by ~10% at all current densities compared to uniformly doped EML PHOLEDs ($D_{mer,\text{uni}}$), and $J_{1/2}$ is increased by an additional 50% leading to a cumulative improvement by a significant factor of 420. Thus, D_{fac} and D_{mer} attain EQE = 10.1 ± 0.2 and 14.4 ± 0.4 % at low luminance, decreasing only slightly to 9.0 ± 0.1 and 13.3 ± 0.1 % at L = 1,000 cd/m^2, and by 50% at L = 7,800 ± 400 and 22,000 ± 1000 cd/m^2 (corresponding to $J_{1/2}$ = 160 ± 10 and 210 ± 10 mA/cm^2), respectively.

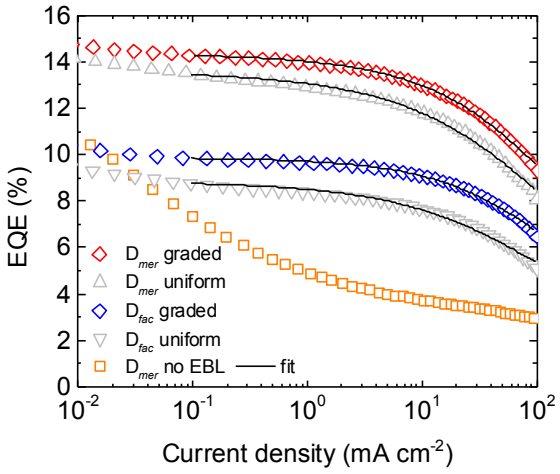

Figure 4.14 EQE vs. current density of deep blue PHOLEDs. The devices have either linearly graded or uniformly doped emission layers consisting of either *fac*- or *mer*-Ir(*pmp*)$_3$. Fits (solid lines) are based on the model in **§4.2.5**. EQE vs. current density for the *mer*-based PHOLED without an EBL is also plotted.

The difference in EQE of D_{fac} vs. D_{mer} is consistent with the trend found in the solid-state PL quantum yields (PLQY) for *fac*- vs. *mer*-Ir(*pmp*)$_3$. **Figure 4.15** shows the higher PLQY of

mer-Ir(*pmp*)$_3$ than the *fac*-isomer when doped in TSPO1 at the same concentrations from 2 to 30 vol% and the values are summarized in **Table 4.6**.

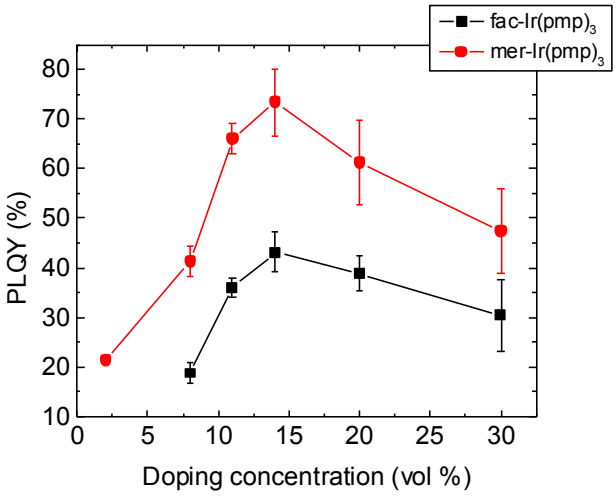

Figure 4.15 Photoluminescence quantum yield of *fac*- and *mer*-Ir(*pmp*)$_3$ doped at various concentrations in TSPO1.

Table 4.6 PLQY of *fac*- and *mer*-Ir(*pmp*)$_3$ at various doping concentrations in TSPO1.

Doping (vol %)	PLQY (%)	
	fac-Ir(*pmp*)$_3$	*mer*-Ir(*pmp*)$_3$
2	-	21 ± 1
8	19 ± 2	41 ± 3
11	36 ± 3	66 ± 3
14	43 ± 4	73 ± 7
20	39 ± 4	61 ± 9
30	30 ± 7	47 ± 8

* Excited at the wavelength of λ = 325 nm by HeCd laser.

Here, a HeCd laser was used for an optical excitation of only the dopant molecules at λ = 325 nm [129]. The PLQY of both isomers increases for doping concentrations of 2 to 14 vol%, decreasing at higher concentrations. It should be noted that the low PLQY of the thin film (<

20 %) at a low doping concentration of 2 vol% significantly deviates from that measured in solution which is 76 – 78 % in 2-MeTHF.

The EQE vs. J of graded and uniformly doped *fac*- and *mer*-Ir(*pmp*)$_3$ PHOLEDs in **Figure 4.14** was modeled to analyze the effect of the distributed recombination profile on device performance (see **§4.2.5** and **Table 4.7**). As the doping concentration changes from the uniform (14 vol%) to graded (20 – 8 vol%), triplet-triplet annihilation rate (k_{TT}) increases while the triplet-polaron annihilation rate (k_{TP}) decreases for both *fac*- and *mer*-Ir(*pmp*)$_3$-based devices. The increased k_{TT} is due to a high triplet concentration in the dopant rich (>14 vol%) region of the EML (**Fig. 4.10**). However, the reduced local density of triplets in the graded EML compensates for the higher k_{TT}. Also, the significantly lower k_{TP} for the graded devices, which is proportional to the charge density [130], is consistent with the measured profiles.

Table 4.7 Parameters for triplet-triplet (k_{TT}) and triplet-polaron annihilation (k_{TP}).

Devices	Doping	Fixed parameter	Fitting parameters	
		τ (μs)*	k_{TT} (10^{-12} cm^{-3}s^{-1})	k_{TP} (10^{-13} cm^{-3}s^{-1})
D_{fac}	Uniform	1.0 ± 0.1	4.6 ± 0.8	8.6 ± 0.1
	Graded		5.6 ± 0.4	3.2 ± 0.5
D_{mer}	Uniform	0.85 ± 0.03	5.8 ± 0.8	10 ± 1
	Graded		7.3 ± 0.4	6.4 ± 0.4

* Triplet lifetime (τ) was obtained from the transient, solid-state phosphorescence decay fit [39]. Errors for the model parameter (k_{TT} and k_{TP}) are the 95% confidence interval.

4.4.2. Discussion

The graded deep blue-emitting phosphor Ir(*pmp*)$_3$ across the EML serves as a wide energy-gap hole transporter that evenly distributes the exciton formation zone, thereby reducing

bimolecular triplet annihilation. Note that light blue-emitting materials such as iridium(III)bis[(4,6-difluorophenyl)-pyridinato-$N,C^{2'}$]picolinate (FIrpic) achieve higher emission efficiency (> 20%) [131], [132] than deep blue PHOLEDs shown here. This is a result of their relatively low emission energies and availability of the corresponding various host materials/systems. Given the difficulties of synthesizing hole-transporting hosts for deep blue PHOLEDs, using hole-transporting gradient doping via the phosphor itself is clearly an effective strategy for improving device efficiency.

While co-host systems using two different compounds to separately transport holes and electrons have previously been shown to improve charge balance in the EML [132], they do not generally eliminate the need for an EBL and/or HBL since charge carriers and excitons can still leak out from the emission zone without them. To prevent leakage, the comparatively high electron mobility in the recent deep blue OLED EML [117], [133] necessitates using an EBL, which have minimal impact on the conventional hole-transport dominated structures [134]. The significantly improved EQE and $J_{1/2}$ of our PHOLED primarily results from the Ir(C^C:)$_3$ EBL (see **Fig. 4.13**). As noted, effective blocking by the dopant itself is a unique property of the Ir(C^C:)$_3$ family of phosphors with their very shallow LUMO energies and wide HOMO-LUMO gaps. Indeed, previously reported deep blue PHOLEDs lacking the EBL are similar to that of our unblocked device with its severe efficiency roll-off, whereas the blocked PHOLED characteristics are similar to those of conventional red and green-emitting devices. This is indicative of charge and exciton confinement achieved in the EML of deep blue PHOLEDs.

The difference in the solid-state PL efficiencies of the *fac*- vs. *mer*-Ir(*pmp*)$_3$ leads to the difference in EQE of D_{fac} vs. D_{mer} and is likely due to different degrees of the emitter aggregation quenching. **Figure 4.16** and **Table 4.8** show the PL spectra and characteristics of

fac- and *mer*-Ir(*pmp*)$_3$ doped at 11 vol% in wide energy gap hosts, p-bis(triphenylsilyly) benzene (UGH2), CzSi, and TSPO1, compared to those diluted at 1 vol% in the solution (2-MeTHF). When the complexes are doped at a high concentration in host matrices, *fac*-Ir(*pmp*)$_3$ tends to form more aggregated clusters resulting in a high degree of concentration quenching [45] and concomitantly lower PLQY. This may be induced by the high static dipole moment of 17.2 D *fac*-Ir(*pmp*)$_3$ versus 10.8 D for the *mer*-isomer, as high dipole moments can promote aggregation [135]. This is compared to the nearly same PLQY of diluted *fac*- and *mer*-Ir(pmp)$_3$ in the solution at a low concentration of 1 vol%.

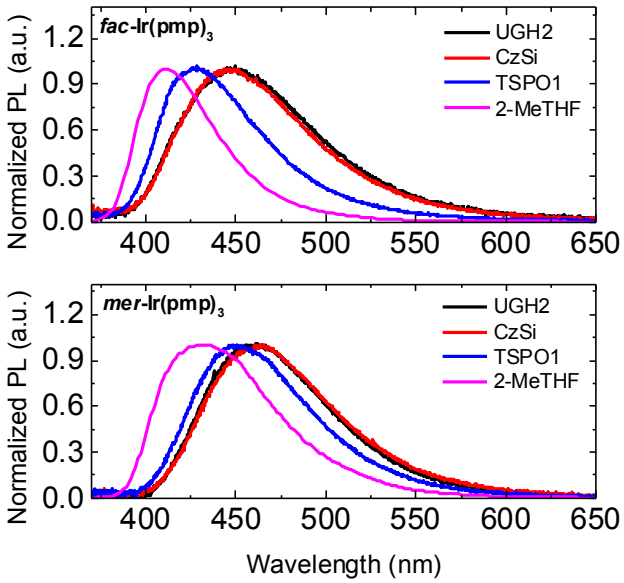

Figure 4.16 PL spectra of *fac*- and *mer*-Ir(*pmp*)$_3$ doped in wide energy gap host matrices compared to those diluted in 2-MeTHF.

TSPO1 is a polar host comprised of the phosphine oxide moieties (P=O) and may lead to additional phosphorescence losses [136]. Strong interactions between TSPO1 molecules form

crystalline domains within an amorphous film, which result in structured, lower energy emission bands [129] superposed with those obtained in solution [137] as can be seen in **Figure 4.17**.

Table 4.8 PL characteristics of thin films of Ir(*pmp*)$_3$ doped in wide energy gap host matrices. Note that PL characteristics of solution samples are included for comparison.

		Solid-state thin film (11 vol%)			Solution (1 vol%)
	Isomers	UGH2	CzSi	TSPO1	2-MeTHF
PLQY (%)	Facial	66 ± 3	23 ± 1	36 ± 2	76 ± 5
	Meridional	85 ± 4	61 ± 3	66 ± 3	78 ± 5
FWHM (nm)	Facial	89	80	66	51
	Meridional	83	83	77	76
CIE (*x*, *y*)	Facial	(0.17, 0.16)	(0.17, 0.15)	(0.16, 0.09)	(0.16, 0.04)
	Meridional	(0.16, 0.18)	(0.16, 0.19)	(0.16, 0.14)	(0.16, 0.09)

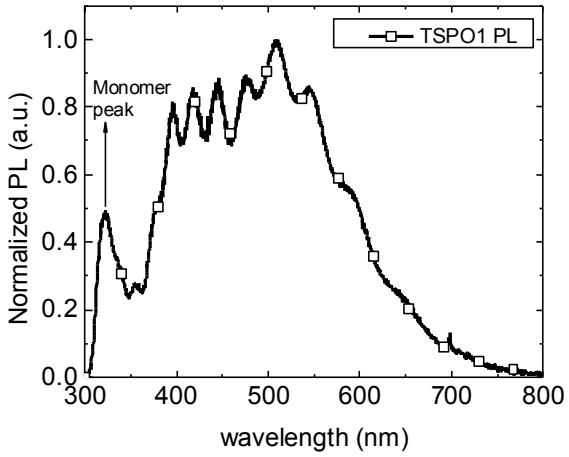

Figure 4.17 PL spectrum of TSPO1. Note that the highest energy emission at λ ≅ 310 nm is from the TSPO1 monomer, while lower energy emission band is from their crystalline domain.

On the other hand, the polar TSPO1 enables a high solid-state solubility of the Ir(*pmp*)$_3$ by preventing interactions between dopants, leading to their physical separation [129], [138]. This enables the comparatively high optimal doping concentration of 14 vol% of Ir(*pmp*)$_3$, as well as a narrower and less bathochromic shifted Ir(*pmp*)$_3$ emission resulting in a more saturated blue emission compared with that in other non-polar hosts (see **Fig. 4. 16** and **Table 4.8**). Finally, Given that the PL quantum yields at 14 vol% in TSPO1 are higher than at either 20 and 8 vol% of Ir(*pmp*)$_3$ (initial and terminal concentrations of the graded doping in the EML), the optimal doping concentrations for EL and PL are different since the dopant also serves as a hole transporter in the PHOLED, affecting the charge balance and hence the EQE.

4.5. Conclusions

We find that deep blue emitting Ir(C^C:)$_3$ complexes can be simultaneously employed as triplet emitting dopants, hole transporters and EBLs. This combination of uses in structures significantly reduce electron and exciton losses. In particular, *fac*-Ir(*pmp*)$_3$-based-PHOLEDs achieved remarkably reduced efficiency roll-off at high current density, resulting in very high brightness (>7,800 cd/m^2) with CIE of [0.16, 0.09] closest to the NTSC requirement among reported Ir-based PHOLEDs. The highly emissive *mer*-isomer of Ir(*pmp*)$_3$, which is due to the strong Ir-NHC ligand bond, enables even brighter PHOLED (>22,000 cd/m^2) operation in the blue. Our advances in materials design and device architectures provide the guidelines for designing efficient and more importantly, long-lived deep blue PHOLEDs.

Chapter 5 Exciton density management for long-lived blue PHOLEDs

5.1. Intrinsic degradation mechanism of PHOLEDs

To improve the operational lifetime of the blue PHOLED, it is imperative to understand the intrinsic factors that cause the degradation of the materials comprising the device during operation and their detrimental impact on the device performance. It was previously suggested that bimolecular annihilation in the EML create the energetically hot excited state that leads to dissociation of molecular bonds of the EML materials [139]. The density of resulting fragmented molecular species increases with time, permanently degrading the device performance.

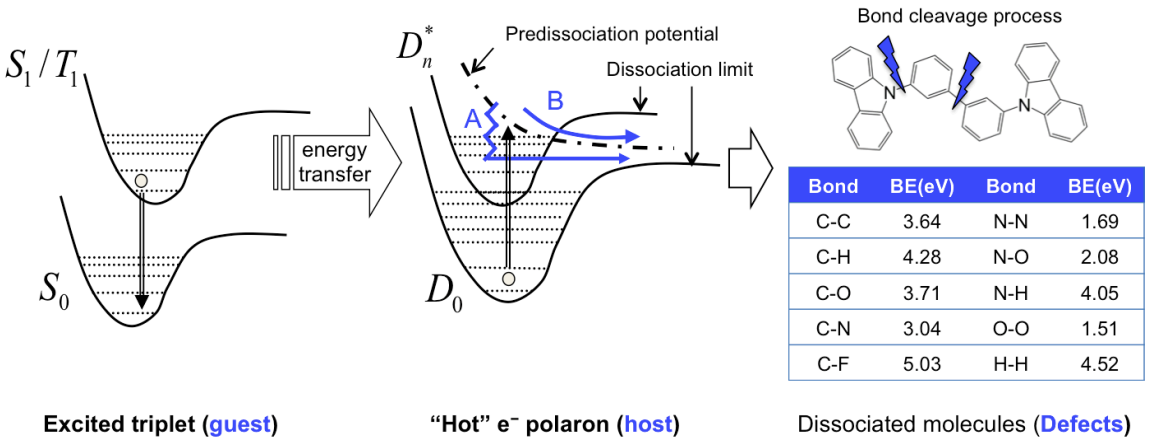

Bond	BE(eV)	Bond	BE(eV)
C-C	3.64	N-N	1.69
C-H	4.28	N-O	2.08
C-O	3.71	N-H	4.05
C-N	3.04	O-O	1.51
C-F	5.03	H-H	4.52

Figure 5.1 Triplet polaron annihilation process causing the degradation of blue PHOLEDs.

Figure 5.1 shows the schematic of triplet-polaron annihilation or TPA proposed as one of intrinsic degradation mechanisms of blue PHOLEDs [33], [140]. The triplet excitons (T_1) on the blue dopant transfer their energy to the electron polarons (D_0) on the host, and subsequently decay to the ground state (S_0) without producing any photons. The polarons gaining energy from the triplets are promoted to energetically higher-lying electronic states called "hot" polarons (i.e. $D_0 \rightarrow D_n^*$). Most of the hot polarons internally convert and relax to their original states (D_0), but some of them can be coupled to a pre-dissociation potential [141] or are possibly routed to the dissociation limit, leading to the bond dissociation of the EML molecules. These fragmented molecules or defects increase in number with time and permanently reduce the device efficiency. For example, the defects may trap and immobilize the electrons or holes, building up space charge that causes the operational voltage to rise. Also, defects can directly quench the excitons, or trapped charges on the defects can nonradiatively recombine with free charges of the opposite polarity, both of which lead to the luminance loss.

This degradation mechanism explains why the lifetime of blue PHOLEDs is shorter than that of the red and green devices. Because of the higher energy of triplet excitons (>2.7 eV) needed for blue emission vs. red (2.0 eV) and green (2.3 eV), hot polarons in the blue PHOLEDs formed due to the TPA can gain an energy up to 6.0 eV. This high energy surpasses the bond dissociation energy of covalent bonds in the molecules, increasing the likelihood that they will be cleaved (see **Fig 5.1**). For this reason, the order of the lifetime of red, green and blue PHOLEDs generally follows the reverse order of energies of their excited states. It is therefore essential to preserve EML molecules by preventing the generation of hot polarons induced by the TPA, and thus the operational stability of the device is improved. In this chapter, we demonstrate

a means to reduce the probability of TPA in the blue PHOLED EML by managing the density of triplet excitons via graded doping [50].

5.2. Performance of the controlled blue PHOLED

Figure 5.2 shows the schematic device structure of the controlled blue PHOLED. The detailed structure is as follow: 70 nm ITO as an anode / 10 nm dipyrazino[2,3,-f:2',3'-h]quinoxaline 2,3,6,7,10,11-hexacarbonitrile (HATCN) as a HIL / 20 nm N,N'-Di(1-naphthyl)-N,N'-diphenyl-(1,1'-biphenyl)-4,4'-diamine (NPD) as a HTL / 30 nm EML / 5 nm 3,3-di(9H-carbazol-9-yl)biphenyl (mCBP) as an HBL / 30 nm Alq_3 as an ETL / 1.5 nm Liq as an EIL / 100 nm Al as a cathode. In the EML, 13 vol% of iridium (III) tris[3-(2,6-dimethylphenyl)-7-methylimidazo[1,2-f] phenanthridine] (Ir(*dmp*)$_3$) is uniformly doped into the mCBP host matrix.

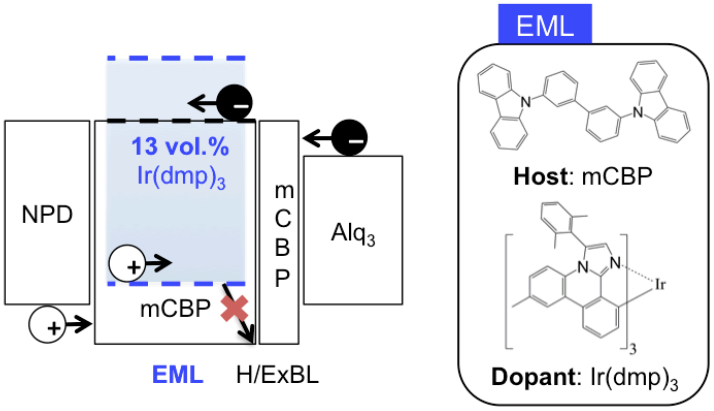

Figure 5.2 Structure of and molecular formulae used in control blue PHOLED.

We investigate charge transport characteristics in the PHOLED EML by fabricating the hole-transport-only (HO) and electron-transport-only (EO) devices. Here, HO and EO devices share the same EML structures whose doping concentrations of the blue dopant are varied from

0, 8, 13 to 20 vol%. Depending on this compositional change, we can analyze the change in the electron and hole transport in the EML. Current density-voltage characteristics of HO and EO devices are shown in **Figure 5.3**.

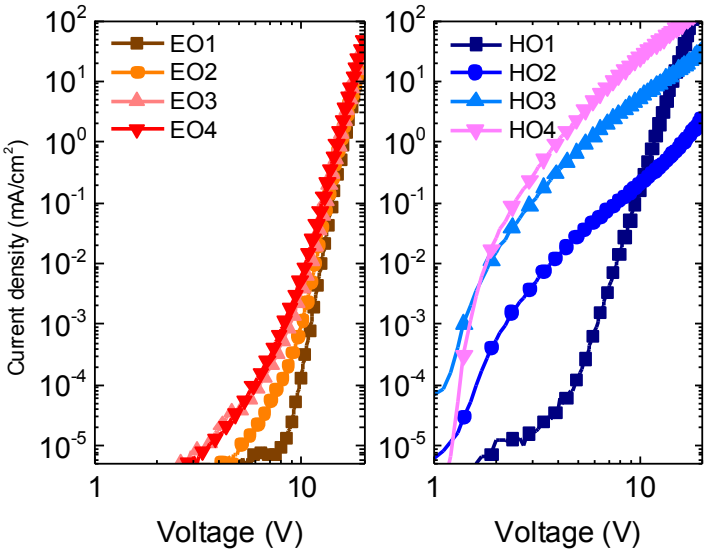

Figure 5.3 Current density vs. voltage of electron-only (EO) and hole-only (HO) devices. EO and HO devices have the same EML with varying doping concentrations from 0, 8, 13, and 20 vol%.

The conductivity of HO devices increases with the doping concentration, while that of EO devices is nearly invariant with the doping concentration. This indicates that the holes are mainly transported by the blue dopant, while electrons are transported by the host. This is consistent with frontier orbitals of the EML molecules, i.e. the blue dopant has more stable and thus favorable HOMO level for the hole transport (4.8 ± 0.1 eV vs. 6.0 ± 0.1 eV for the host), while the host has more shallow LUMO level that is more suitable for the electron transport (1.2 ± 0.1 eV vs. 1.5 ± 0.1 eV for the dopant, see **Fig. 5.2**).

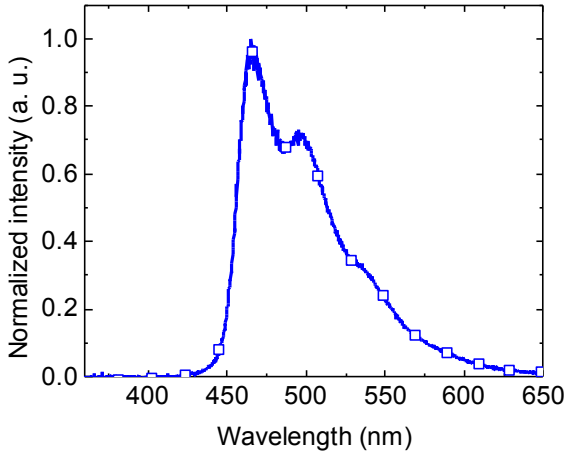

Figure 5.4 EL spectrum of control blue PHOLED.

Figure 5.4 shows an electroluminescent spectrum of the controlled blue PHOLED, whose CIE chromaticity coordinates are $(x, y) = (0.16, 0.31)$. There is no spectral feature of the NPD fluorescence that peaks at a wavelength of $\lambda \approx 425$ nm, indicating that electrons are effectively blocked by the HTL (NPD) and thus confined within the EML. However, triplet excitons may diffuse and potentially leak out of the EML and nonradiatively recombine on the NPD HTL, due to its lower triplet energy of $E_T = 2.3$ eV than both blue dopant and the host of $E_T = 2.7$ and 2.9 eV, respectively. Without an HBL (i.e. a neat layer of mCBP included between the EML and the Alq_3 ETL as shown in **Fig. 5.2**), the fluorescence from Alq_3 is observed [33], indicating that a high density of holes and excitons may be blocked and accumulated at the interface between the EML and the HBL (see below). **Figure 5.5** shows time evolution of normalized luminance degradation, $L(t)/L_0$, and change in the operating voltage, $\Delta V(t) = V(t) - V_0$, measured from an initial luminance of $L_0 = 3{,}000$ cd/m^2 under constant current operation. Here, V_0 is the initial operating voltage of the as-grown device to obtain $L_0 = 3{,}000$ cd/m^2.

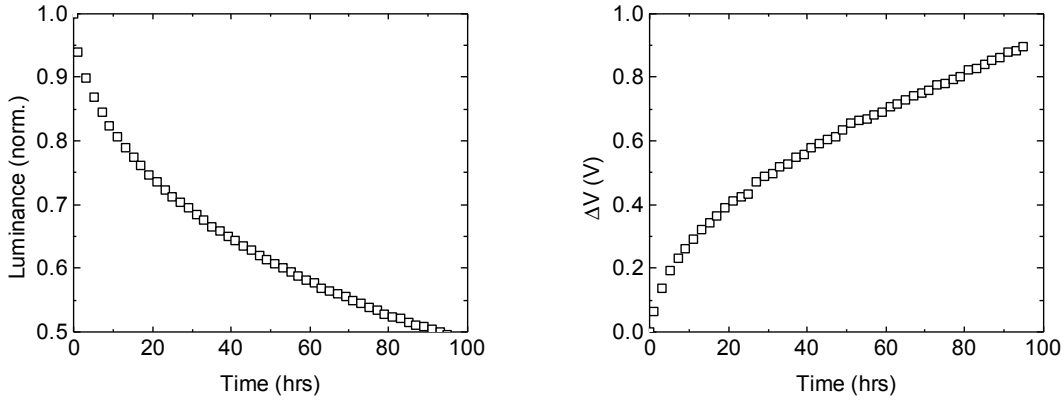

Figure 5.5 Time evolution of normalized luminance degradation and operating voltage rise of the control blue PHOLED. These lifetime characteristics were measured from an initial luminance of L_0 = 3000 cd/m^2 under constant current operation.

The observed, continuous luminance degradation ($L(t)/L_0$) and operating voltage rise ($\Delta V(t)$) of the device is caused by a growing number of defects in the EML. The defects, whose energies are situated within the energy gap of the device EML, act as nonradiative recombination centers, exciton quenchers, and charge traps (see below). The molecular dissociation rate or defect formation rate is associated with the frequency of the TPA that increases with the densities of excitons and polarons. Unbalanced charge transport between electrons and holes in the EML can lead to an irregular distribution of the excitons and the location of the higher density of excitons is preferentially degraded. Therefore, it is important to distribute the excitons across the EML to reduce their local densities and thereby to reduce the probability of TPA.

5.3. Exciton density management by graded doping

To verify that the reduced TPA by distributing the exciton density improves the operational lifetime of blue PHOLEDs, we fabricated three test devices as shown in **Figure 5.6**.

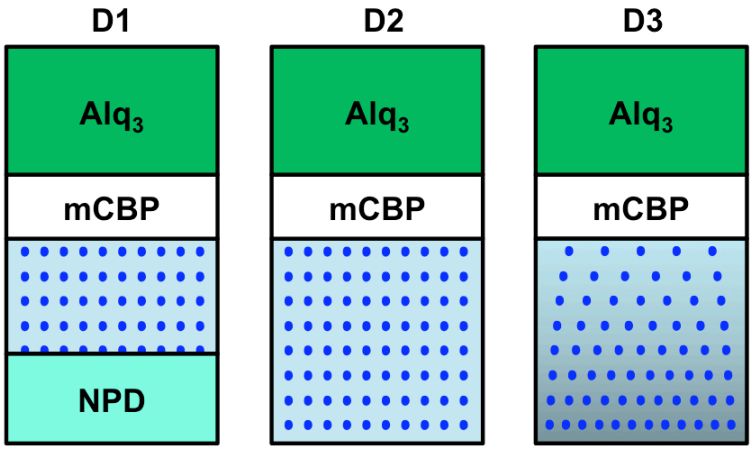

Figure 5.6 Schematic of blue PHOLEDs with different EML structures. D1 is the control device with the 20 nm-thick HTL (NPD) and the 30 nm-thick EML uniformly doped with Ir(*dmp*)$_3$ at 13 vol% into mCBP. Compared to D1, D2 has the widened, 50nm-thick EML at the same doping concentration and lacks the HTL. In D3, the doping concentration is linearly graded from 18 to 8 vol% across the 50nm-thick EML without the HTL.

D1 is the control device with the 20 nm-thick HTL (NPD) and the 30 nm-thick EML uniformly doped with Ir(dmp)$_3$ at 13 vol% into the mCBP host. Compared to D1, D2 has a widened, 50nm-thick EML at the same doping concentration (i.e. 13 vol%), but lacks the HTL. In D3, the doping concentration is linearly graded from 18 at the HTL/EML interface to 8 vol% at the EML/HBL interface across the 50nm-thick EML without the HTL. That is, the average volume concentration of blue dopants in the EML of D1, D2, and D3 are same.

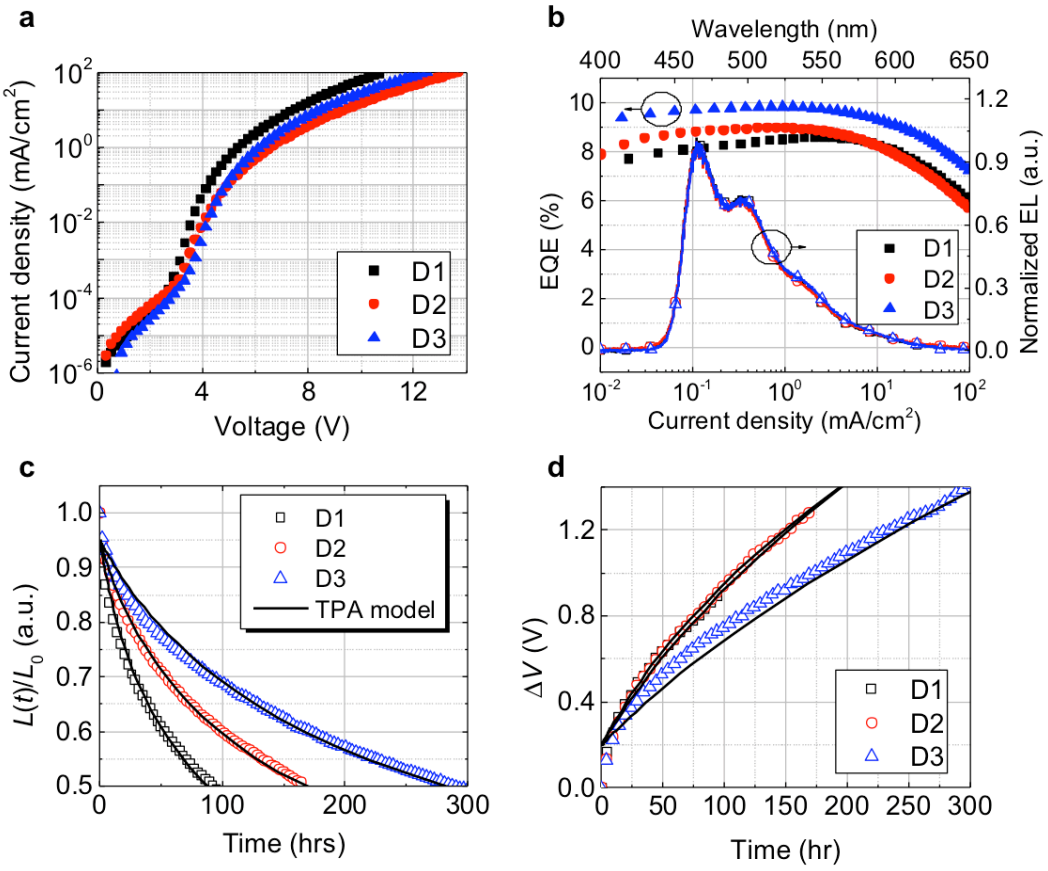

Figure 5.7 Device performance of blue PHOLEDs. (a) Current density vs. voltage characteristics, (b) EQE vs. current density characteristics and normalized EL spectra, (c) time evolution of normalized luminance degradation and (d) operating voltage rise for blue PHOLEDs (D1, D2, and D3). The solid lines in (c) and (d) are fit based on the TPA model.

Figure 5.7 (a) and **(b)** shows the current density vs. voltage and EQE vs. current density characteristics, respectively, of D1, D2, and D3. By increasing the thickness of the EML and eliminating the HTL, the conductivity of D2 and D3 decrease compared to that of D1 due to the reduced hole conductivity. However, due to the higher doing concentration near the HTL/EML interface of D3 (i.e. 18 vol% vs. 13 vol% for D2), holes can be more efficiently injected into and transported through the EML of D3 than that of D2, leading to the higher conductivity of D3. D3

attains the higher EQE at all current densities than both D1 and D2 due to the reduced bimolecular annihilations (see below). The EL spectra measured at a current density of J = 10 mA/cm^2 for D1, D2, and D3 are nearly identical, yielding the same CIE chromaticity coordinates of (0.16, 0.31). Thus, we can confirm that the emission is solely produced from the blue dopant and a negligible spectral shift is attributed to the minor change in their microcavity conditions. **Figure 5.7 (c)** and **(d)** show the time evolution of the luminance degradation and the operating voltage rise of D1, D2, and D3 measured from the same luminance of L_0 = 3000 cd/m^2. The required operating current densities (J_0) to obtain L_0 are J_0 = 21, 21, and 17.3 mA/cm^2 for D1, D2, and D3, respectively. T80 of D1, D2, and D3 are 12, 25, and 39 hr, respectively. T80 of D2 is increased by 2-fold from that of D1, and D3 attains the even longer T80 than D2 by employing the graded doping. The operating voltage rise shown in **Fig. 5.7 (d)** is indicative of the growing number of defects over time. Thus, the lower voltage rise of D3 compared to D1 and D2 is due to the lower density of defects present in the EML. Since the trapped polaron on the defect nonradiatively recombines with the opposite polaron and the empty defect directly quenches the exciton, both of which lead to the luminance loss, a lower density of defects in D3 EML contributes to less severe luminance degradation than D1 and D2, leading to the longer T80.

Figure 5.8 shows the triplet exciton density, $N(x)$, as a function of a distance to the anode, x, of the EMLs of D1, D2, and D3 measured at J = 10 mA/cm^2. A detailed method of measuring the exciton density can be found in ref. [50] and **Chapter 6**. D1 has a high density of excitons accumulated at the EML/HBL interface (x = 60 nm). This is because of more efficient hole transport than that of the electrons. In D2, the exciton density near the EML/HBL interface is decreased, but the peak appears at x = 25 nm. This is because of the reduced hole transport across the broadened EML as well as a lack of the HTL and therefore, electrons can more deeply

penetrate towards the anode side of the EML. In D3 EML, a more distributed and smooth exciton profile is obtained, because high doping concentration of 18 vol% at the HIL/EML interface (x = 10 nm) initially facilitates the hole injection and transport, impeding the penetration of the electrons. Also, since the doping concentration linearly reduces to 8 vol% towards the cathode side (x = 60 nm), holes are gradually blocked and result in the distributed exciton profile without having an abrupt peak.

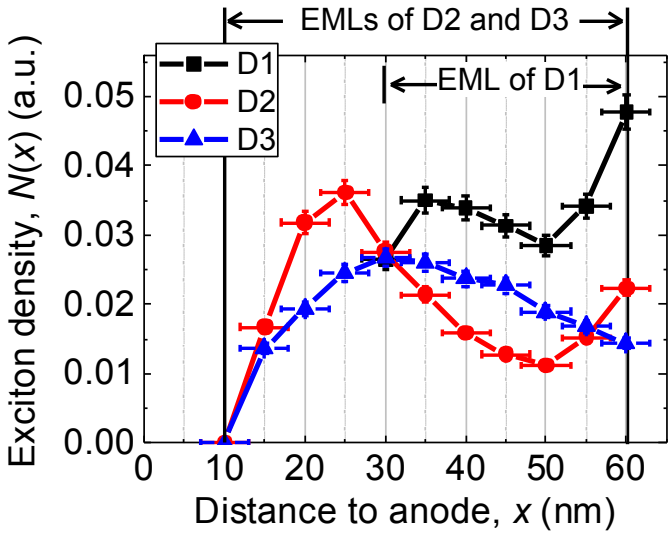

Figure 5.8 Triplet exciton density of blue PHOLED EMLs. The local triplet density, $N(x)$, as a function of the distance to the anode, x, for the EMLs of D1, D2, and D3 is measured at J = 10 mA/cm^2.

Note that the densities of excitons of D2 and D3 EMLs vanish at the HIL/EML interface of x = 10 nm due to quenching by HATCN. This is presumably due to the extremely stable LUMO of HATCN ≈ 5.4 eV that leads to a small energy offset between the LUMO of HATCN and HOMO of the blue dopant = 4.8 ± 0.1 eV. Thus, excitons diffused from the blue dopant to the HIL/EML interface may relax to low energy exciplex states that nonradiatively recombine or

get dissociated. However, this exciton quenching does neither deteriorate the efficiency nor the lifetime of the devices (see **Fig. 5.7**).

To confirm that the distributed exciton density reduces the TPA and thereby improves the device lifetime, we develop a model for fitting both $L(t)/L_0$ and $\Delta V(t)$. The coupled rate equations for densities of hole (p), electron (n), and excitons (N) are:

$$\begin{aligned}
\frac{dp(x,t,t')}{dt'} &= G(x) - \gamma n(x,t,t')p(x,t,t') - k_{Qn}Q(x,t)p(x,t,t') \\
\frac{dn(x,t,t')}{dt'} &= G(x) - \gamma n(x,t,t')p(x,t,t') - k_{Qp}Q(x,t)n(x,t,t') \\
\frac{dN(x,t,t')}{dt'} &= \gamma n(x,t,t')p(x,t,t') - \left(\frac{1}{\tau} + k_{QT}Q(x,t)\right)N(x,t,t')
\end{aligned} \tag{5.1}$$

Two different time scales are used where t' is the duration of charge transport and energy transfer (~μs) and t is the device degradation time (~hr) due to the defects with the density of $Q(x, t)$. For the simplicity of the model, we assume that defects only trap holes [33]. In the equations, $G(x) = J_0/e \cdot N(x) \Big/ \int_{EML} N(x)dx$ is the local recombination rate calculated using the measured triplet exciton density ($N(x)$, see **Fig. 5.8**), γ = 1.7×10^{-13} cm^3s^{-1} is the Langevin recombination rate, τ = 1.1 μs is the natural decay time of the dopant triplet exciton, k_{Qp} = 4.8×10^{-14} cm^3s^{-1} and k_{Qn} = 1.7×10^{-13} cm^3s^{-1} are rates for hole trapping by the defects and trapped hole-electron recombination, respectively, and k_{QT} is the rate for exciton quenching by defects that is used as a fitting parameter [50]. The **Eq. (5.1)** can be solved under steady-state conditions such that $t'\rightarrow\infty$, yielding $\lim_{t'\to\infty} n(x,t,t'), p(x,t,t')$ and $N(x,t,t') = n(x,t), p(x,t)$ and $N(x,t)$. Defects ($Q(x,t)$) are generated as a result of the molecular dissociation in the PHOLED EML, which is triggered by the TPA between the triplet exciton on the blue dopant and the electron polaron on the host [33]:

$$\frac{dQ(x,t)}{dt} = k_Q N(x,t)n(x,t) \tag{5.2}$$

Here, k_Q is the rate of molecular dissociation resulted from the TPA and used as a fitting parameter. Then, **Eq. (5.2)** and steady-state $n(x,t)$, $p(x,t)$ and $N(x,t)$ are numerically solved to fit both the luminance degradation and operating voltage rise as:

$$\begin{aligned} L(t)/L_0 &= \int_{EML} N(x,t)\eta_{OC}(x)dx, \\ \Delta V(t) &= \frac{e}{\varepsilon_r \varepsilon_0}\int_{EML} xQ(x)dx \end{aligned} \tag{5.3}$$

The TPA model fits the lifetime characteristics of D1, D2, and D3 as shown in **Fig. 5.7 (c)** and **(d)** with similar fitting parameters, i.e. $k_Q \approx 1.0\times10^{-11}$ cm^3s^{-1} and $k_{QN} \approx 7\times10^{-24}$ cm^3s^{-1} [50]. This indicates that the lifetime improvement of D3 compared to D2 and D1 results from distributed densities of excitons and charges. Note that initial values for the model fit for $L(t)/L_0$ and $\Delta V(t)$ are 0.95 and 0.2 V, respectively. This arbitrary initial condition was chosen to account for the rapid initial drop of the luminance and rise of the operating voltage of the devices, presumably attributed to water contamination or other external factors [142]. In fact, this is due to various types of EML defects with different energetic distribution and those generated outside the EML by degradation of charge transport and blocking layers. These aspects in the lifetime model will be discussed in **Chapter 6**.

As a further step to improve the lifetime of the blue PHOLED, two stacked graded-EML devices were fabricated and denoted as D3T. The detailed structure of D3T is as follows: ITO / 10 nm HATCN / 50 nm graded EML / 5 nm mCBP / 5 nm Alq_3 / 70 nm 2 vol% of Li doped into Alq_3 as an n-doped ETL / 10 nm HATCN / 50 nm graded EML / 25 nm Alq_3 / 1.5 nm Liq / 100 nm Al. Here, n-doped ETL and HIL forms a charge generation interface where two cells are connected [143]. **Figure 5.9** shows the comparison of electroluminescent and lifetime characteristics of D3 and D3T.

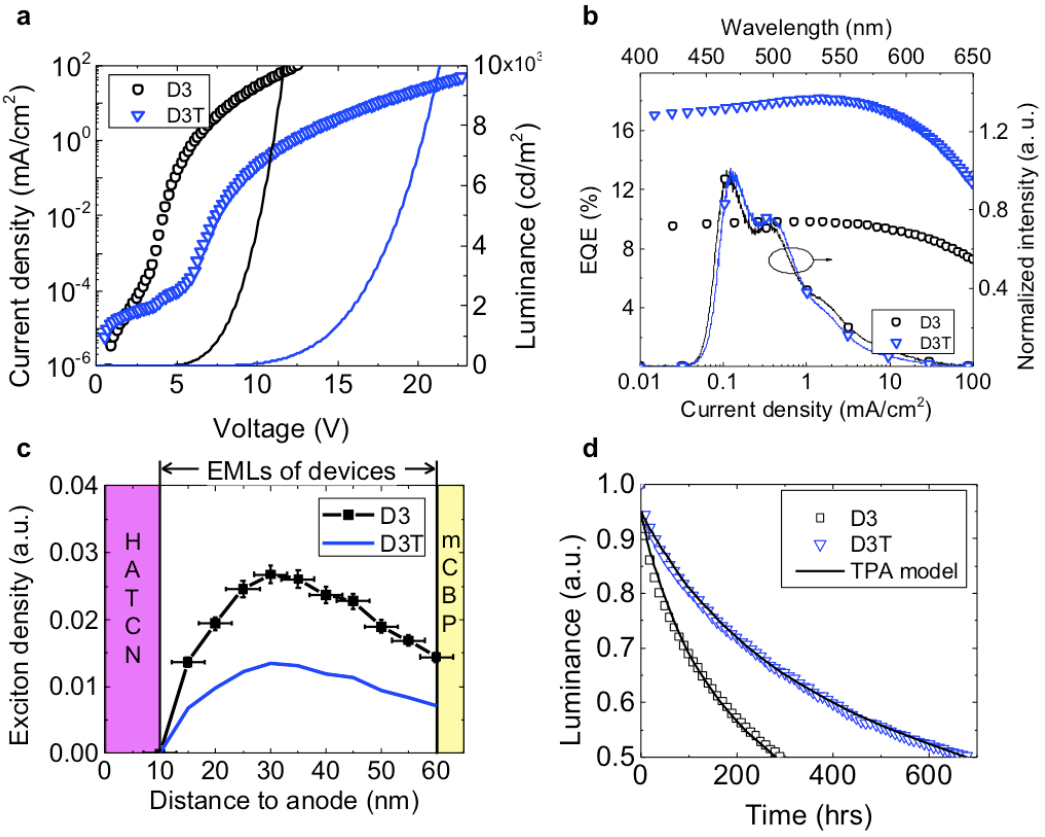

Figure 5.9 Device performance of tandem blue PHOLEDs. (a) Current density–voltage–luminance characteristics, (b) EQE vs. current density characteristics and EL spectra, (c) triplet exciton density profile in the EML, and (d) normalized luminance degradation of D3 and D3T. The solid line is fit based on the TPA model.

As shown in **Fig. 5.9 (a)**, D3T requires nearly twice the voltage of D3 to achieve the same current density; however, at the same luminance, D3T obtains the significantly higher EQE than that of D3 (e.g. 17.3 vs. 9.0 % for D3T and D3 at L_0 = 3000 cd/m^2, respectively, see **Fig. 5.9 (b)**). The high EQE of D3T results in its reduced J_0 = 9.0 vs. 17.3 mA/cm^2 for D3 to obtain L_0 = 3000 cd/m^2, thereby reducing the density of excited states in the device EML. Here, J_0 of D3T was larger than half of that of D3 due to loss in efficiency by stacking devices and the blue shifted EL spectrum due to the microcavity effect relative to that of D3. Nevertheless, the lifetime of D3T is

significantly increased compared to D3 due to the reduced J_0 as shown in Fig. **5.9 (d)**. For example, T80 of D3T = 106 vs. 39 hrs for D3 at L_0 = 3,000 cd/m^2. In the TPA model, we assume that the shape of the exciton profile in the D3T EML is unchanged from that of D3, while its density is scaled by their J_0 ratio (i.e. by 9.0/17.3, see **Fig 5.9 (c)**). Based on this assumption, the TPA model fits the lifetime data of D3T with the reduced TPA by the reduced J_0, leading to the slow luminance degradation compared to D3.

In summary, T80 of D3T = 106 hrs is enhanced by nearly 9.2 times compared to D1 of T80 = 12 hrs at L_0 = 3000 cd/m^2. This results from the reduced TPA by distributing the exciton density in the PHOLED EML via graded doping and by reducing J_0 via stacking devices. As a result, the molecular dissociation process followed by the TPA is reduced, improving the operational stability of blue PHOLEDs. If devices are measured from L_0 = 1000 cd/m^2, T80 is improved from 56 to 616 hrs from D1 to D3T, corresponding to nearly tenfold improvement. The strategy of managing the exciton density introduced here can be universally applied not only to blue PHOLEDs, but also red and green devices, as well as the fluorescent OLEDs to further improve their operational stability.

Chapter 6 Hot excited state management for long-lived PHOLEDs

6.1. Introduction to hot excited state management

The short operational lifetime of blue PHOLEDs has been convincingly attributed to annihilation between excited states (i.e. exciton-exciton or exciton-polaron) in the device EML [33], [50], [140], [144], resulting in an Auger process that produces a "hot" (i.e. multiply excited) exciton while the remaining state nonradiatively transitions to the ground state. The hot state can attain up to double the energy of the initial excited state ($\geq$ 6.0 eV). Thus, there is a possibility that energy dissipation of the hot states on the blue dopant or host molecules can induce chemical bond dissociation [141], [145]. The probability of this reaction increases with the excited state energy, and hence is particularly dominant for blue PHOLEDs compared with red and green-emitting analogs.

The key to realizing long-lived blue PHOLEDs is, therefore, to manage the hot states to prevent molecular dissociation. This can be accomplished by reducing bimolecular annihilations, or by "bypassing" the dissociative processes altogether. Reduction of bimolecular annihilation has recently been demonstrated by evenly distributing excitons and polarons across the EML via dopant grading [50]. Here we demonstrate an effective strategy to thermalize the hot states without damaging the blue dopant or host molecules in the EML. This approach leads to a substantial improvement in the operational stability of blue PHOLEDs beyond that observed to date. For this purpose, we add an ancillary dopant called an excited state "manager" into the

EML. The manager has a triplet exciton energy intermediate between that of the lowest energy triplets of the EML molecules and the hot states generated by bimolecular annihilation. By enabling the rapid exothermic energy transfer from the hot states to the manager, the probability of direct dissociative reactions in the EML is reduced, leading to a significant improvement in the device lifetime.

To optimize the non-destructive de-excitation of hot states, the manager dopant must be located in the region where the triplet excitons have the highest density where bimolecular annihilation is most probable. Implementing this strategy, the longest-lived managed blue PHOLEDs achieve an approximately 3.6 ± 0.1 and 1.9 ± 0.1 times increased lifetime of T80 = 334 ± 5 hr at L_0 = 1,000 cd/m^2, compared to previously reported state-of-the-art conventional and graded-EML devices of T80 = 93 ± 9 and 173 ± 3 hr, respectively. To our knowledge, this significant improvement results in the longest-lived blue PHOLEDs yet reported. We develop a triplet annihilation-based model that accurately predicts the lifetime characteristics of managed PHOLEDs for several different device configurations. Based on our results, we provide selection criteria for manager molecules that can enable further improvement in the stability of both blue phosphorescent and TADF-based OLEDs.

6.2. Experimental methods

6.2.1. Device fabrication and characterization

PHOLEDs were grown by vacuum sublimation in a chamber with a base pressure of 4×10^{-7} Torr on pre-patterned indium-tin-oxide (ITO) glass substrates (VisionTek Systems Ltd., United Kingdom). The device and the structures of GRAD and managed PHOLEDs are as follows: 70 nm ITO anode / 5 nm HATCN as a hole injection layer (HIL) / 10 nm N,N'-

Di(phenyl-carbazole)-N,N'-bis-phenyl-(1,1'-biphenyl)-4,4'-diamine (CPD)[146] hole transport layer (HTL) / 50 nm EML / 5 nm mCBP:Ir(dmp)$_3$ 8 vol% exciton blocking layer (EBL) / 5 nm mCBP hole blocking layer (HBL) / 25 nm Alq$_3$ electron transport layer (ETL) / 1.5 nm Liq as an electron injection layer / 100 nm Al cathode. The conventional PHOLED (CONV) has the following structure [33], [50]: 5 nm HATCN / 30 nm CPD / 35 nm 13 vol% Ir(dmp)$_3$ uniformly doped in mCBP / 5 nm mCBP / 25 nm Alq$_3$ / 1.5 nm Liq / 100 nm Al. The device area is 2 mm^2 defined by the intersection of a 1 mm wide ITO strip and an orthogonally positioned 2 mm wide metal cathode patterned by deposition through a shadow mask. HATCN and Alq$_3$ were purchased from Luminescence Technology Corporation (Taiwan), CPD was from P&H Technology (S. Korea), mCBP and Ir(dmp)$_3$ were provided by Universal Display Corporation (Ewing, NJ. USA) and *mer*-Ir(pmp)$_3$ was synthesized following previous methods [42]. The *J-V-L* characteristics of the PHOLEDs were measured [97] using a parameter analyzer (HP4145, Hewlett-Packard) and a calibrated Si-photodiode (FDS1010-CAL, Thorlab). The PHOLED emission spectra were recorded using a calibrated spectrometer (USB4000, OceanOptics). For lifetime tests, PHOLEDs were operated at constant current (U2722, Agilent) and the luminance and voltage data were automatically collected (Agilent 34972A). Errors quoted for the measured electroluminescent and lifetime characteristics (J_0, V_0, *EQE*, T90, T80 and $\Delta V(t)$) are standard deviations taken from a population of from three devices.

6.2.2. Exciton profile measurement

The exciton density profile, $N(x)$, was measured across the EML by inserting ultrathin (~1Å) red phosphorescent (iridium (III) bis (2-phenylquinolyl-N, $C^{2'}$) acetylacetonate (PQIr))

sensing layers at different locations within the EML in a series of blue PHOLEDs. The integrated emission intensities of PQIr and Ir(dmp)$_3$ at J_0 are converted into the number of excitons at x via:

$$I_{sens}(\lambda,x) = a_{PQIr}(x)I_{PQIr}(\lambda) + a_{Ir(dmp)_3}(x)I_{Ir(dmp)_3}(\lambda) \tag{6.1}$$

where $I_{sens}(\lambda, x)$ is the emission intensity consisting of the combined spectra of Ir(dmp)$_3$ ($I_{Ir(dmp)3}(\lambda)$) and PQIr ($I_{PQIr}(\lambda)$). The relative weights of $a_{PQIr}(x)$ and $a_{Ir(dmp)3}(x)$, respectively, were used. Then, the outcoupled exciton density, $\eta_{out}(x)N(x)$, is equal to the relative number of excitons emitting on the PQIr at x as:

$$\eta_{OC}(x)N(x) = A \cdot EQE(x) \cdot \frac{a_{PQIr}(x)\int I_{PQIr}(\lambda)/\lambda\, d\lambda}{a_{PQIr}(x)\int I_{PQIr}(\lambda)/\lambda\, d\lambda + a_{Ir(dmp)_3}(x)\int I_{Ir(dmp)_3}(\lambda)/\lambda\, d\lambda} \tag{6.2}$$

Here, $EQE(x)$ is external quantum efficiency of the device with the sensing layer at x; thus the right-hand side of **Eq. (6.2)** gives the relative number of excitons at position x. Also, $\int_{EML} N(x)dx = 1$, and $\eta_{out}(x)$ is the outcoupling efficiency calculated as the fraction of outcoupled light emitted at x based on Green's function analysis [105]. The Förster transfer length of ~3 nm [50] limits the spatial resolution of the measurement.

Since the thickness of delta-doped PQIr is less than a monolayer, PQIr molecules are spatially dispersed to avoid emission loss by concentration quenching [147]. A delta-doped sensing layer only slightly affects the charge transport as opposed to previously used 1–2 nm-thick, doped layers [50], [148], [149]. This leads to a variation in operating voltages at J_0 of < 0.5 V among all sensing devices (see also the upper panel of **Fig. 6.4b**).

6.2.3. Lifetime degradation model

The rate equations for holes (p), electrons (n) and excitons (N) are:

$$\frac{dp(x,t,t')}{dt'} = G(x) - \gamma n(x,t,t')p(x,t,t') - k_{Qp}\left[Q_A(x,t) + Q_B(x,t)\right]p(x,t,t'),$$
$$\frac{dn(x,t,t')}{dt'} = G(x) - \gamma n(x,t,t')p(x,t,t') - k_{Qn}\left[Q_A(x,t) + Q_B(x,t)\right]n(x,t,t'),$$
$$\frac{dN(x,t,t')}{dt'} = \gamma n(x,t,t')p(x,t,t') + k_{Qn}Q_B(x,t)n(x,t,t') - \left\{\frac{1}{\tau_N} + k_{QN}Q_A(x,t)\right\}N(x,t,t'). \quad (6.3)$$

There are two different time scales: t' is the duration of charge transport and energy transfer (~μs), and t is the device degradation time (~hr) due to the formation of defect, $Q_A(x,t)$ and $Q_B(x,t)$. The triplet decay lifetime is τ_N = 1.4 ± 0.1 μs, obtained from the transient PL decay of thin-film EMLs of the GRAD and managed PHOLEDs. Also, $G(x) = J_0/e \cdot N(x) \Big/ \int_{EML} N(x)dx$ is the generation rate of excitons due to charge injection at current J_0, $\gamma = e\left(\mu_p + \mu_e\right)\Big/\varepsilon_r\varepsilon_0$ is the Langevin recombination rate, where e is the elementary charge, μ_n and μ_p are the electron and hole mobilities [150], [151] in the EML, respectively, and ε_0 and $\varepsilon_r \sim 3$ are the vacuum and relative permittivities, respectively. It follows that $k_{Qn} = e\mu_n/\varepsilon_r\varepsilon_0$ is the reduced Langevin recombination rate describing the recombination of immobile trapped holes and mobile electrons.

The trap densities, Q_A and Q_B, resulting from the TTA increase at rates k_{QA} and k_{QB} are given by:

$$\frac{dQ_A(x,t)}{dt} = k_{QA}\left\{N(x,t)\right\}^2,$$
$$\frac{dQ_B(x,t)}{dt} = k_{QB}\left\{N(x,t)\right\}^2. \quad (6.4)$$

Eq. (6.3) is solved in steady state ($t' \to \infty$), yielding $\lim_{t'\to\infty} n(x,t,t'), p(x,t,t')$ and $N(x,t,t') = n(x,t), p(x,t)$ and $N(x,t)$, respectively. This set of equations

is numerically solved with $Q_A(x,t)$ and $Q_B(x,t)$ to fit both the luminance loss and voltage rise as a function of *t* using:

$$L(t)/L(0) = \int_{EML} N(x,t)\eta_{OC}(x)dx \tag{6.5}$$

and

$$\Delta V(t) = \frac{e}{\varepsilon\varepsilon_0}\left(\int_{EML} xQ(x,t)dx + \int_{ext} x'Q_{ext}(x',t)dx'\right) \tag{6.6}$$

Here, $\eta_B(x)$ is the outcoupling efficiency of the excitons emitted at x, and $Q_{ext}(x',t)$ is introduced to account for the voltage rise caused by traps present outside the EML. The uniqueness of the fit that yields parameters, k_{QN}, k_{Qp}, k_{QA}, k_{QB}, and k_{Qext}, has been tested and it is found that the parameters are uniquely determined by the model.

Note that when extracting k_{Qext} and thus $\Delta V_{ext}(t)$ from the fits, the polaron densities in the EML at J_0 are used. However, k_{Qext} should more accurately reflect the polaron densities in the transport layers due to charge trapping by Q_{ext}, and thus, a reduction in layer conductivity. This simplifying assumption leads to its large variation among devices compared with other parameters. Initial values of Q_A, Q_B, and Q_{ext} are set at 10^{15} (cm^{-3}), at which they do not result in the initial voltage offset (<0.05 V), but accurately trace the time evolution of $\Delta V(t)$ and converge to their final values after the iteration of the least-square algorithm.

6.3. Hot excited state management mechanism for blue PHOLEDs

Figure 6.1 shows the Jablonski diagram of an EML containing an excited state manager and the possible relaxation pathways for excitons. While we will focus our discussion on phosphorescent OLEDs, this process also represents the excited state energies available in TADF devices; hence a similar degradation pathway is assumed to be active in both cases. The manager

can enable the transfer of the hot singlet/triplet state (S^*/T^*) resulting from triplet-triplet annihilation (TTA, process 2) to the lowest excited state of the manager (S_M/T_M) via process 3'. We note that the hot state can be either an exciton or polaron state resulting from either TTA or triplet-polaron annihilation (TPA), respectively.

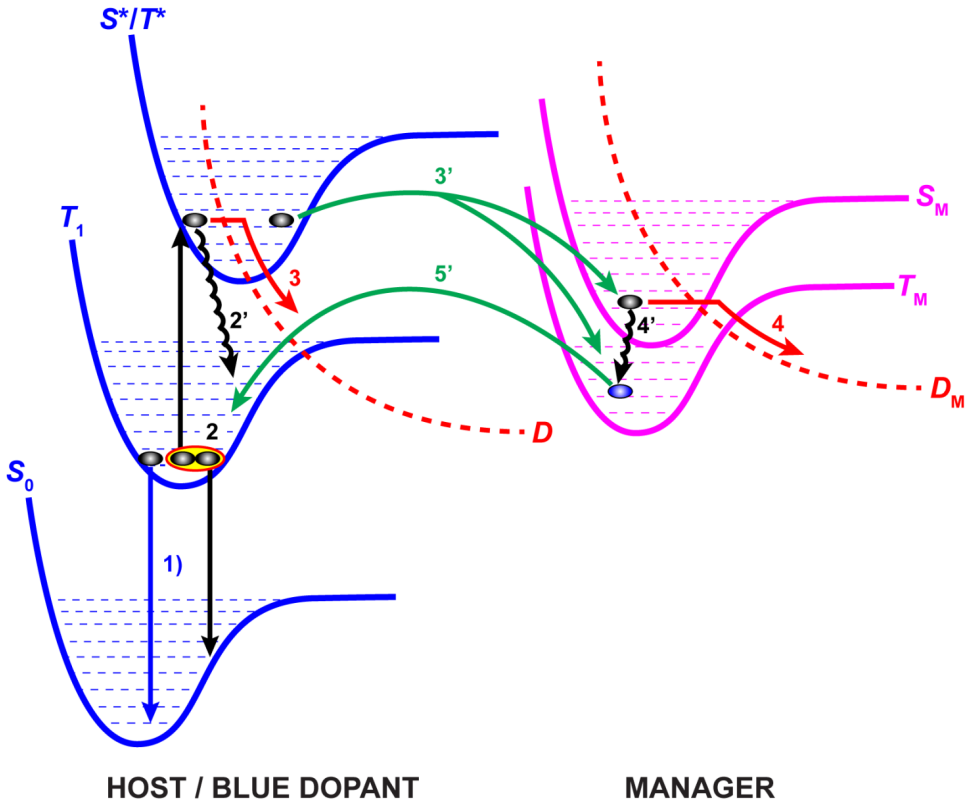

Figure 6.1 Jablonski diagram of the EML containing manager molecules. Here, S_0 is the ground state, T_1 is the lowest energy triplet state and S^*/T^* is a hot singlet/triplet manifold of the blue dopant or host. *D* represents the dissociative state the EML materials. S_M/ T_M is the lowest singlet/triplet state of the manager. Possible energy-transfer pathways are numbered as follow: 1) radiative recombination, 2) TTA resulting in excitation to S^*/T^*, 2)' internal conversion and vibrational relaxation, 3) and 4) dissociative reactions leading to molecular dissociation, 3)' exothermic Förster energy transfer for singlet-to-singlet transitions, and 3)' and 5)' Dexter energy transfer for triplet-to-triplet transitions, and 4)' intersystem crossing and vibrational relaxation.

As will be shown below, the system investigated here is dominated by TTA, although either or both mechanisms may be active [33]. Furthermore, the hot state (S^*/T^*) can be one of many potential electronic state manifolds above the lowest one. However, given the extremely rapid decay rates from the higher states, it is likely that S_2/T_2 is the most probable hot state for inducing dissociative reactions.

By introducing a manager whose energy S_M/T_M is greater than that of either the host or blue dopant, transfer from S^*/T^* to S_M/T_M is allowed, and damage to these molecules via dissociative reactions (process 3) is minimized provided that the rate for $S^*/T^* \rightarrow S_M/T_M$ is comparable to or higher than $S^*/T^* \rightarrow D$, where D is the dissociative state for the guest or the host in the EML. The energy transfer of the hot state to the manager, $S^* \rightarrow S_M$ or $T^* \rightarrow T_M$ via process 3' is based on exothermic Förster or Dexter transfer, respectively. In this work we use a heavy metal (Ir) complex as the manager. Hence, the transferred singlet state on the manager undergoes vibrational relaxation followed by the intersystem crossing to the triplet state ($S_M \rightarrow T_M$ via process 4'), which subsequently transfers back to the blue dopant or host ($T_M \rightarrow T_1$) via the Dexter process 5'. This leads to radiative recombination (process 1), or is recycled back to S^*/T^* by a repeat process. It is also possible that the high energy S_M/T_M state can result in dissociation of the manager itself via $S_M/T_M \rightarrow D_M$ (process 4), i.e. where the manager serves as a sacrificial additive to the EML. Process 4 is not optimal since the number of effective managers decreases over time, providing less protection for the host and blue dopant as the device ages. Nevertheless, even in this case presence of the manager can still increase device stability.

From the foregoing discussion, three primary criteria must be met for effective molecular design of the manager: (i) The exciton energy of the manager should be intermediate between that of the multiply excited (S^*/T^*) and lowest exciton states (S_1/T_1) of the host and blue dopants;

(ii) the rate of transfer to the manager (process 3') must be comparable to or higher than that for dissociation (process 3); and (iii) the manager should be sufficiently stable such that it does not degrade on a time scale short compared to that of the unmanaged device (process 4).

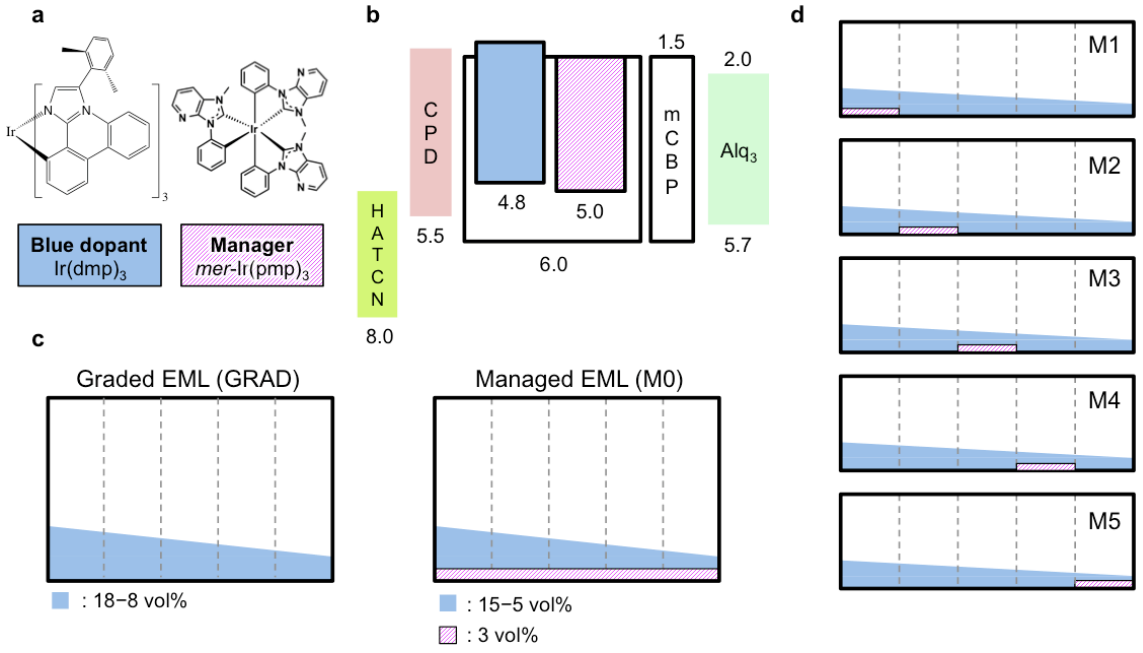

Figure 6.2 Energy and doping schemes of managed blue PHOLEDs. (a) Molecular formulae of Ir(*dmp*)$_3$ and *mer*-Ir(*pmp*)$_3$, used for the blue dopant and the manager, respectively. (b) Energy level diagram of the PHOLED with the manager. Numbers in the figure are energies referred to the vacuum level. (c) Doping scheme of the 50 nm-thick EML for the graded-EML and managed PHOLEDs, denoted as GRAD and M0, respectively. GRAD has the blue dopant graded from 18 to 8 vol% in the mCBP host, while M0 is a similarly graded device but with the 3 vol% of the manager replacing the blue dopant of the same amount, compared to GRAD, to keep the total doping concentration the same for both devices. (d) Managed PHOLEDs M1 – M5 have selectively doped 10 nm-thick zones of the EML. The zones have a manager doping of 3 vol% substituting the blue dopant of the same amount. The other details of the EML are identical to that of GRAD.

For that purpose, we introduce N-heterocyclic carbene (NHC) Ir(III) complex, meridional-tris-(N-phenyl, N-methyl-pyridoimidazol-2-yl)iridium (III) [*mer*-Ir(*pmp*)$_3$] [42], as the manager in the PHOLED EML. The EML also consists of the blue dopant, iridium (III) tris[3-(2,6-dimethylphenyl)-7-methylimidazo[1,2-f] phenanthridine] [Ir(*dmp*)$_3$] [33], [50], and the host, 4,4'-bis[N-(1-naphthyl)-N-phenyl-amino]-biphenyl (mCBP) [152]. **Figure 6.2 (a)** shows molecular formulae of *mer*-Ir(*pmp*)$_3$ and Ir(*dmp*)$_3$. The manager is characterized by a relatively strong metal-ligand bond [106] and a high glass transition temperature of 136 °C. The triplet energy of *mer*-Ir(*pmp*)$_3$ is 2.8 eV calculated from its peak phosphorescence spectrum (λ = 454 nm), while its onset is at $E_{T1} \approx 3.1$ eV, higher than that of the blue dopant and host of $E_{T1} \approx$ 2.8 and 2.9 eV, respectively [152] (**Fig. 6.3 (a)**). Thus, *mer*-Ir(pmp)$_3$ fulfills criterion (i) of the manager, although both criteria (ii) and (iii) are not suitably met by this molecule. Hence, these complexes have not been optimized for rapid transfer via process 3'. This is a function of the intimate orbital overlap between manager and blue dopant or host; a property controlled by the steric and orbital characteristics of all molecules involved. Nor is *mer*-Ir(pmp)$_3$ particularly stable, which can lead to manager depletion with time (process 4) In spite of these shortcomings, we find significant lifetime improvements for the managed vs. the non-managed blue PHOLEDs, suggesting that there is considerable scope for additional benefits that should arise from optimized manager molecules.

6.4. Performance of managed blue PHOLEDs

Figure 6.2 (b) shows the energy level diagram of the managed devices. The lower energy (>1 eV) of the HOMO of the blue dopant compared with that of the host suggests that hole transfer is predominantly supported by the dopant molecules and only slightly by the manager,

while electrons are transported by both the host and the manager having nearly identical LUMO energies. The EML doping schemes of the graded control, and managed PHOLEDs are given in **Fig. 6.2 (c)** (denoted as GRAD and M0, respectively; see **§6.2.1**). For the GRAD device, the concentration of the blue dopant is linearly graded from 18 to 8 vol% from the hole transport layer (HTL) to the electron transport layer (ETL) interfaces to enable a uniform distribution of excitons and polarons throughout the region. This structure was previously shown[50] to have reduced bimolecular annihilation, and thereby achieve an extended lifetime compared to conventional, non-graded EML devices (denoted CONV; see **§6.2.1**). In device M0, a 3 vol% of the manager is uniformly doped across the EML, and the concentration of the blue dopant is graded from 15 to 5 vol%. To investigate the position of the manager that results in the longest operational lifetime, the manager is doped at 3 vol% into 10 nm-thick zones at various positions within the 50 nm-thick EML of devices M1 – M5, shown in **Fig. 6.2 (d)**. Except for the zone with the manager, the remainder of the EMLs for M1 – M5 are identical to that of GRAD. Thus, the total doping concentrations of the managed devices are kept the same as that of the GRAD PHOLED.

Figure 6.3 (a) shows the electroluminescence (EL) spectra of GRAD, M0, M3 and M5 measured at a current density of J = 5 mA/cm^2. The GRAD and managed PHOLEDs exhibit nearly identical EL spectra with Commission Intermationale de l'Elcairage (CIE) chromaticity coordinates of (0.16, 0.30). This confirms that in managed devices, radiative recombination occurs solely on the blue dopant. Note that the excitons can be formed on the manager either by direct electron-hole recombination or transferred from hot states via process 3'. Since the lowest triplet state of the manager has a higher energy of E_{T1} = 3.1 eV vs. 2.8 eV for the blue dopant, triplets on the manager efficiently transfer back to the blue dopant via process 4' in **Fig. 6.1**.

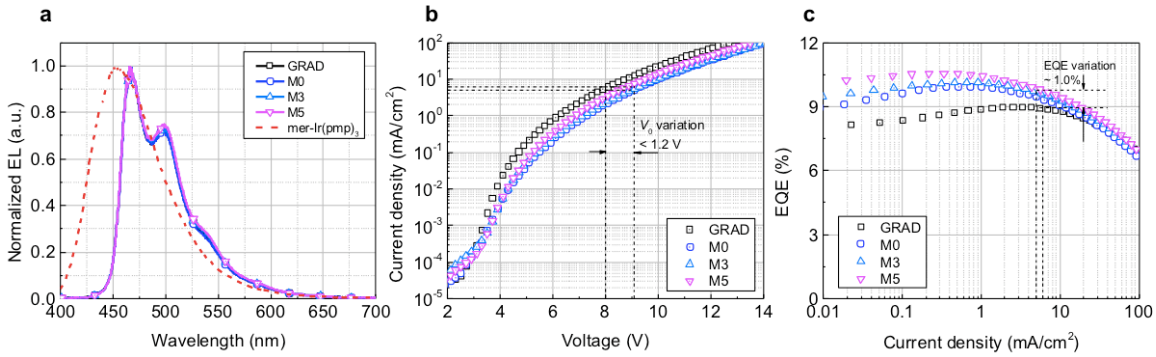

Figure 6.3 Device performance of managed blue PHOLEDs. (a) Normalized EL spectra of the GRAD and managed PHOLEDs, M0, M3, and M5, measured at a current density of J_0 = 5 mA/cm^2. For comparison, the PL spectrum of the manager [*mer*-Ir(*pmp*)$_3$] is also shown. (b) Current density-voltage, and (c) *EQE*-current density characteristics of GRAD and selected managed PHOLEDs. Note that between GRAD and the managed PHOLEDs, the absolute difference of the operating voltages (V_0) and *EQE* at an initial luminance of L_0 = 1,000 cd/m^2 for the lifetime test are < 1.2 V and 1.0 %, respectively.

Figure 6.3 (b) and **(c)** show the current density–voltage (*J*–*V*) and EQE–*J* characteristics of GRAD, M0, M3 and M5. **Table 6.1** summarizes properties of their EL characteristics at L_0 = 1,000 cd/m^2. The initial operating voltages (V_0) of the managed PHOLEDs (M0 – M5) are higher than GRAD by ~1V. This is consistent with the lower hole mobility of the manager compared to that of the blue dopant. For example, when a small concentration (< 5 vol%) of the manager is added as a substitute of the same amount for the blue dopant, the device resistance marginally increases. This is due to the difference in the HOMO levels between the manager at 5.3 ± 0.1 eV and 4.8 ± 0.1 eV for the blue dopant, creating a small energy barrier that impedes hole transport between the manager molecules. The *EQE* of the managed PHOLEDs at L_0 = 1000 cd/m^2 is slightly (< 1.0 %) higher than that of the GRAD, leading to the maximum difference in drive current density of J_0 < 0.6 mA/cm^2 needed to achieve the same L_0.

Table 6.1 EL characteristics for CONV, GRAD and managed PHOLEDs at L_0 = 1,000 cd/m^2.

Device	J_0 [mA/cm^2]	EQE [%]	V_0 [V]	†CIE
CONV	6.7 ± 0.1	8.0 ± 0.1	6.6 ± 0.0	(0.15, 0.28)
GRAD	5.7 ± 0.1	8.9 ± 0.1	8.0 ± 0.0	(0.16, 0.30)
M0	5.5 ± 0.1	9.4 ± 0.1	9.2 ± 0.0	(0.16, 0.30)
M1	5.4 ± 0.1	9.5 ± 0.1	8.8 ± 0.1	(0.16, 0.29)
M2	5.4 ± 0.1	9.3 ± 0.0	8.9 ± 0.1	(0.16, 0.31)
M3	5.3 ± 0.1	9.6 ± 0.0	9.0 ± 0.1	(0.16, 0.30)
M4	5.2 ± 0.1	9.6 ± 0.2	8.6 ± 0.0	(0.16, 0.31)
M5	5.1 ± 0.1	9.9 ± 0.1	8.6 ± 0.0	(0.16, 0.31)

EQE, external quantum efficiency

† Measured at current density of J = 5 mA/cm^2.

***** Errors for the measured values are standard deviation from at least three devices.

Figure 6.4 (a) shows the time evolution of the increase in operating voltage, $\Delta V(t) = V(t)–V_0$, and normalized luminance loss, $L(t)/L_0$ of GRAD and managed devices. For these experiments, the PHOLEDs were continuously operated at constant current to yield L_0 = 1,000 cd/m^2 at t = 0. **Table 6.2** summarizes the lifetime characteristics (T90, T80 and corresponding $\Delta V(t)$) for GRAD and managed PHOLEDs. Managed PHOLEDs (M0 – M5) have increased T90 and T80 relative to those of GRAD. For example, the longest-lived device M3 has a T90 and T80 of 141 ± 11 and 334 ± 5 hr, corresponding to a 3.0 ± 0.1 and 1.9 ± 0.1 times improvement from those of GRAD with 47 ± 1 and 173 ± 3 hr, respectively. Compared with CONV having T90 and T80 of 27 ± 4 and 93 ± 9 hr, M3 achieves 5.2 ± 0.2 and 3.6 ± 0.1 times improvement in T90 and T80, respectively. Here, T90 and T80 are used to determine the short- and long-term effectiveness of the excited state management, indicative of its potential use in PHOLED-based display and lighting applications. Although these applications may impose somewhat different

requirements (e.g. T95 or T70, respectively), consistent improvements in both T90 and T80 indicate the usefulness of the manager in both applications.

Table 6.2 Lifetime characteristics for CONV, GRAD and managed PHOLEDs at L_0 = 1,000 cd/m^2

Device	T90 [hr]	T80 [hr]	ΔV(T90) [V]	ΔV(T80) [V]
CONV	27 ± 4	93 ± 9	0.3 ± 0.1	0.4 ± 0.1
GRAD	47 ± 1	173 ± 3	0.6 ± 0.1	0.9 ± 0.1
M0	71 ± 1	226 ± 9	0.9 ± 0.1	1.2 ± 0.1
M1	99 ± 3	260 ± 15	1.2 ± 0.1	1.6 ± 0.1
M2	103 ± 0	285 ± 8	0.7 ± 0.1	1.0 ± 0.1
M3	141 ± 11	334 ± 5	1.1 ± 0.1	1.5 ± 0.2
M4	126 ± 7	294 ± 16	1.0 ± 0.1	1.3 ± 0.1
M5	119 ± 6	306 ± 3	0.9 ± 0.1	1.2 ± 0.1

* Errors for the measured values are standard deviation from at least three devices.

The reduced lifetime improvement by the manager from 3.0 ± 0.1 to 1.9 ± 0.1 times increases in T90 and T80, respectively, for M3 is attributed to the degradation of the manager molecules via process 5. We found that increasing the manager concentration to > 3 vol% in the EML neither improves the lifetime nor the efficiency, while it leads to an increased operating voltage due to the low hole mobility of the manager. To further enhance both efficiency and lifetime of the devices, manager molecules with improved stability and hole mobility than *mer*-Ir(pmp)$_3$ are required.

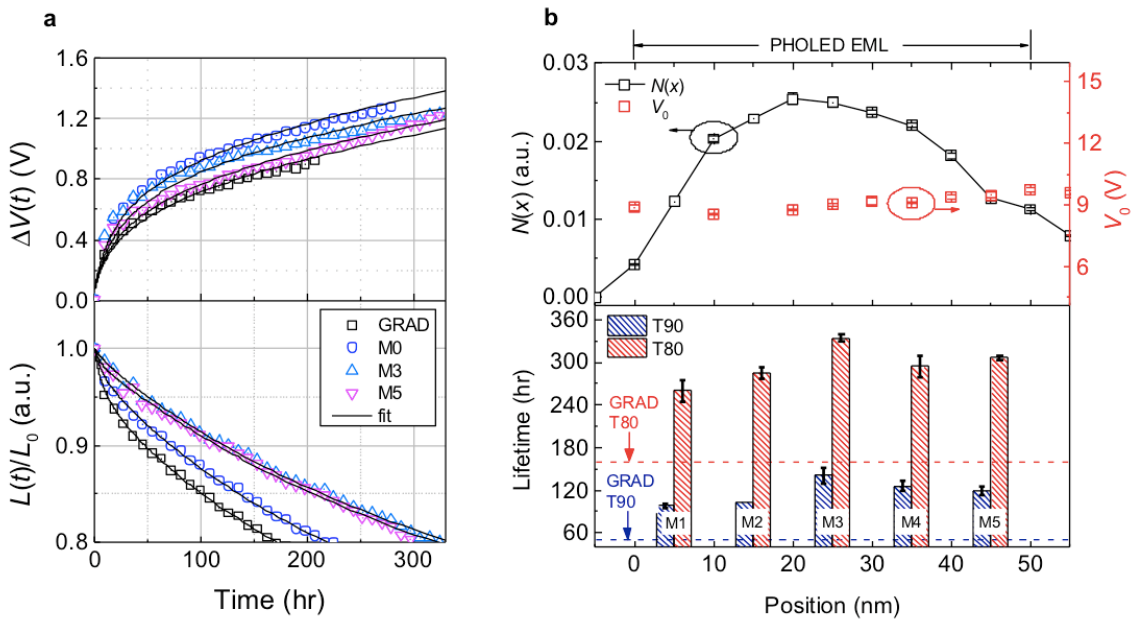

Figure 6.4 Lifetime of managed blue PHOLEDs. (a) Lifetime characteristics of managed PHOLEDs M0, M3 and M5, compared with GRAD. Top and bottom show the time evolution of the operating voltage change, $\Delta V(t) = V(t) - V_0$, and the normalized luminance degradation, $L(t)/L_0$, respectively. Solid lines are fits based on the model in **§6.2.3** (see fitting parameters in **Table 6.3**). (b) (Top) Exciton density profile, $N(x)$, of the PHOLED emission layer (EML) as a function of position, x, and operating voltages of the devices using delta-doped sensing layer at J = 5 mA/cm^2. The origin of the x-axis is at the HTL/EML interface. The operating current density results in a luminance of L_0 = 1,000 cd/m^2. (Bottom) Lifetimes (T90 and T80) of managed devices (M1 – M5) as functions of the position of the managed EML zones. T90 and T80 of the managed devices are compared with those of the GRAD (dotted lines). Note that the variation in lifetime qualitatively follows the exciton density profile, suggesting that placing the manager at the point of highest exciton density results in the longest device lifetime.

The upper panel of **Fig. 6.4 (b)** shows the measured triplet density profile, $N(x)$, in the GRAD EML at J_0 = 5 mA/cm^2, where x is the distance from the EML/HTL interface. The T90 and T80 of managed PHOLEDs (M1 – M5) are compared as functions of the manager position in

the EML in the lower panel in **Fig. 6.4 (b)**. Note that the variation in lifetime qualitatively follows the exciton density profile. For example, the manager in M3 is located at 20 nm < x < 30 nm, which is at the point of highest measured exction density relative to those of the other managed devices. Hence, it is anticipated that the effectiveness of the manager at this position is greatest, as is indeed observed from the data in this figure (**Table 6.2**).

Finally, the change in operating voltage, $\Delta V(t)$, required to maintain a constant current density of the managed PHOLEDs is larger than that of GRAD, while their rate of luminance degradation is reduced (**Fig. 6.4 (a)**). This suggests the formation of polaron traps that have no effect on the luminance.

6.5. Discussion

The degraded products by molecular dissociation can be formed in any and all PHOLED layers, but those located in the EML play a dominant role in affecting the device luminance. On the other hand, changes in the device operating voltage can arise from defects generated both within and outside the EML. Therefore, a premise in understanding device lifetime is that both the energetics and positions of the defects in the PHOLEDs can influence their performance in different ways.

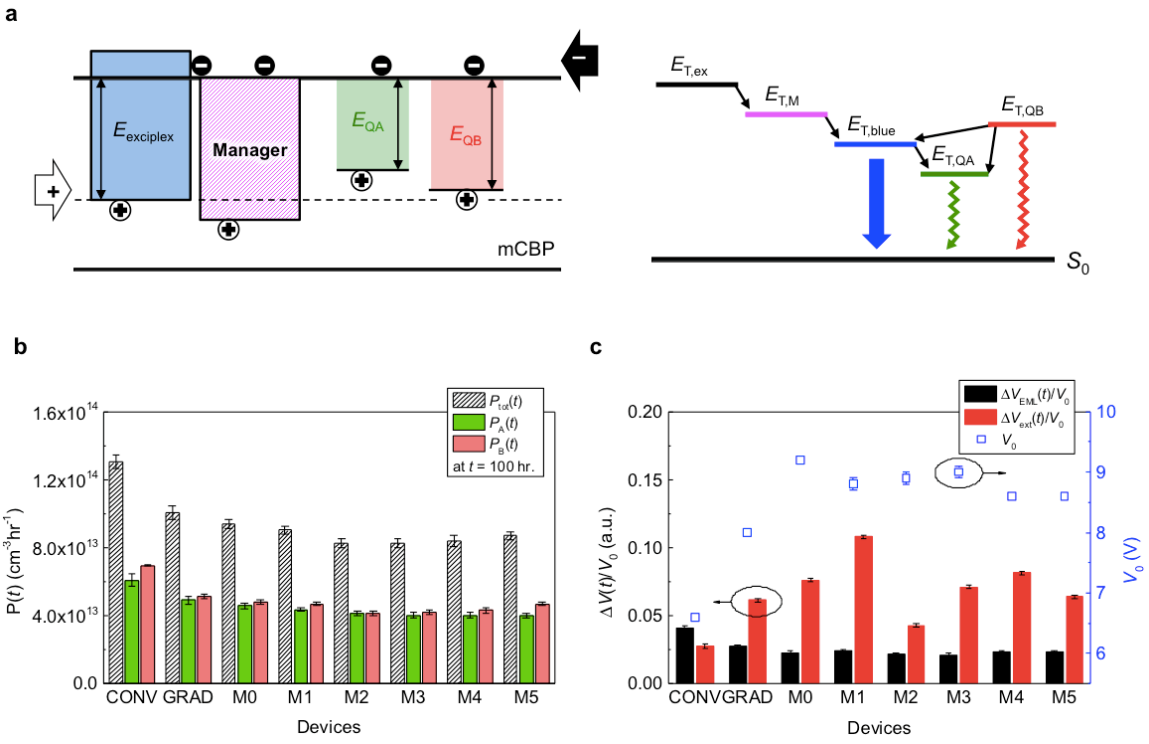

Figure 6.5 Lifetime model for managed PHOLEDs. (a) (Left) Energy level diagram of the doped EML along with proposed positions of Q_A and Q_B. Here, Q_A and Q_B are assumed to be hole traps, with Q_A deeper in the energy gap than Q_B. Holes are transported by the blue dopant and the manager, and are potentially trapped by Q_A and Q_B. Electrons are transported by the host and the manager. (Right) Energy diagram of the triplet exciton states in the EML. The sources of triplet excitons in the as-grown device due to charge recombination are twofold: triplet exciplexes ($E_{T,ex}$) generated between the host and the blue dopant, and triplet excitons directly formed on the manager ($E_{T,M}$). Both can exothermically transfer to the blue dopant ($E_{T,dop}$). Q_A, the deep hole trap, has a low-energy triplet state that results in exciton quenching ($E_{T,QA}$), while Q_B, the shallow trap ($E_{T,QB}$), transfers excitons to the lower energy sites. (b) Average Q_A and Q_B generation rates in the EML, $P_A(t)$ and $P_B(t)$, from hot states in CONV, GRAD, and managed PHOLEDs. The total defect generation rate is $P_{tot}(t)$ where t = 100 hr. (c) Relative contributions to the voltage rise with respect to V_0 induced by defects within and outside the EML (i.e. $Q_A + Q_B$ and Q_{ext}, respectively) at t = 100 hr. The separate contributions to the voltage rise, $\Delta V_{EML}(t)/V_0$ and $\Delta V_{ext}(t)/V_0$, along with V_0 are shown.

To model the lifetime data, we consider that two types of dissociated products, Q_A and Q_B, are generated by the hot states within the EML. For simplicity, both are assumed to be hole traps [153], with Q_A lying deeper in the energy gaps of the host and blue dopant than Q_B, as shown in **Fig. 6.5 (a)**. Both traps are charged when filled, leading to an increase in voltage, $\Delta V(t)$. Shockley-Read-Hall (SRH) nonradiative recombination occurs for holes trapped on Q_A. Likewise, exciton quenching via triplet states at Q_A results in a decrease in luminance (**Fig. 6.5 (a)**). On the other hand, shallow Q_B defects can capture excited states that are subsequently transferred to the blue dopant, and thus do not affect the PHOLED luminance. Note that the triplets on the blue dopant (at energy $E_{T,dop}$) are transferred from exciplex states originally formed between the hole on the blue dopant and the electron on the host ($E_{T,ex}$) [50], as well as from excitons formed directly on the manager ($E_{T,M}$). The latter is possible because, as implied by the energy scheme in **Fig. 6.5 (a)**, the manager is found to transport both electrons and holes in the EML.

Based on these considerations, we developed a lifetime model for fitting $L(t)/L_0$ and $\Delta V(t)$ of CONV, GRAD, and managed PHOLEDs similar to that previously reported [50]. The best fit is provided by assuming that defects generated in the EML are the result of TTA without needing to include TPA processes. This differs from previous conclusions claiming that TPA is the dominant path to failure, although it was noted that both TPA and TTA might be active in defect formation [140], [144]. Indeed, whether TPA or TTA is the dominant degradation mechanism is dependent on several factors including the details of the materials used for the host and dopant, the distribution of charges and excitons within the EML at a particular current density, and so forth. In any case, all of these analyses implicate hot exciton states as the source of the loss of luminance and operating voltage rise in the aged blue PHOLEDs. Thus,

introducing exciton managers in regions with the highest exciton density results in the longest lifetime, as is indeed the case for M3.

The model also includes the effects of degradation of layers outside the EML, resulting in the increase of the operating voltage without affecting luminance. These include the degradation of the charge transport (i.e. HTL and ETL) and blocking layers, and the electrodes, all of which are commonly observed in aged devices [154]–[156]. This extrinsic degradation is possibly due to polaron-induced charge traps of density, Q_{ext} [156]. Unlike Q_A and Q_B however, Q_{ext} only accounts for ΔV and not ΔL (**Eq. (6.6)**). For simplicity, it is assumed that charge and exciton blocking properties of the devices are unchanged over time.

Table 6.2 summarizes the parameters used for fitting the lifetime data for CONV, GRAD and the managed PHOLEDs. The defect generation rates k_{QA} and k_{QB}, are similar for most devices, yielding nearly similar Q_A and Q_B in the managed PHOLEDs, which are smaller than those in the GRAD and CONV over the same operational period, t. For example, Q_A and Q_B in M3 at t = 100 hr are (5.4±0.1) and (5.5±0.1)×10^{16} cm^{-3}, while those in GRAD are (6.1±0.2) and (6.3±0.1)×10^{16} cm^{-3}, and those in CONV are (7.3±0.2) and (8.2±0.1)×10^{16} cm^{-3}, respectively. The routes leading to luminance loss are: (i) SRH recombination between trapped holes on Q_A and electrons at rate, $k_{Qn}Q_An$, and (ii) direct exciton quenching by Q_A at rate, $k_{QN}Q_AN$. Here, k_{Qn} and k_{QN} are the reduced Langevin and defect-exciton recombination rates, respectively, and n and N are the steady-state densities of electrons and excitons, respectively (**Eq. (6.3)**). Reduction in both terms in the managed PHOLEDs compared to CONV and GRAD is primarily attributed to their correspondingly lower Q_A, which results in their reduced rate of luminance degradation. The defect formation reaction rate within the EML is given by $P(t) = \frac{1}{d_{EML}} \int_{EML} \frac{dQ(x,t)}{dt} dx$.

Figure 6.5 (b) shows the rates for generating Q_A and Q_B, and $Q_A + Q_B$ ($P_A(t)$, $P_B(t)$, and $P_{tot}(t)$, respectively) at t = 100 hr. For example, for CONV, $P_{tot} = (1.3\pm0.1)\times10^{14}$ cm^{-3}hr^{-1} is reduced to $P_{tot} = (1.0\pm0.1)\times10^{14}$ cm^{-3}hr^{-1} for GRAD, and decreases further to $P_{tot} = (0.8 \pm 0.1)\times10^{14}$ cm^{-3}hr^{-1} for M3. It is remarkable that only a 15% decrease in the defect formation rate for managed vs. graded doping devices leads to a nearly two-fold improvement in T80, suggesting that even a small change in the probability of dissipation of excess energy can have large effects on extending device lifetime.

Note that since the luminance loss is primarily due to Q_A, the high P_A of CONV and GRAD of (6.1±0.4) and (4.9±0.3)×10^{13} cm^{-3}hr^{-1} leads to a luminance of < 800 and 850 ± 10 cd/m^2, respectively, as opposed to that of M3 = 920 ± 10 cd/m^2 with $P_A = (4.0\pm0.1)\times10^{13}$ cm^{-3}hr^{-1} at t = 100 hr. On the other hand, M3, M4, and M5 have similar P_A, yielding a luminance of 915±5 cd/m^2, while P_B are (4.2±0.1), (4.3±0.2), and (4.7±0.1)×10^{13} cm^{-3}hr^{-1}, respectively. This larger variation in P_B results since Q_B can return excitons to the dopants where they have a renewed opportunity to luminesce, and thus its effect on the in luminance is small compared to P_A.

The percentage contributions of $k_{Qn}Q_An$ to the luminance degradation (i.e. $k_{Qn}Q_An$ + $k_{QN}Q_AN$) is 90 ± 2 % for most devices. This indicates that SRH recombination is the dominant luminance decay mechanism due to the presence the large density of injected polarons that are lost prior to exciton formation.

When hot states are generated in blue-emitting devices, all molecular bonds are potentially vulnerable to dissociation by the very high energy of the hot states (E_{T*} ~ 5.4–6 eV)[156]. That is, Q_A and Q_B may result from many possible molecular fragments or defect species, but for our purposes we simply assign two discrete energy levels without identifying a

particular compound. This assumption can lead to somewhat larger uncertainties in the hole trapping rate (k_{Qp}) compared with other parameters extracted from the model (see **Table 6.3**).

Table 6.3 Parameters for lifetime model for CONV, GRAD and managed PHOLEDs.

Device	k_{QN} [10^{-11} cm^3/s]	k_{Qp} [10^{-7} cm^3/s]	k_{QA} [10^{-21} cm^3/s]	k_{QB} [10^{-21} cm^3/s]	k_{Qext} [10^{-21} cm^3/s]
CONV	3.3 ± 0.4	0.7 ± 0.2	0.9 ± 0.1	1.0 ± 0.1	0.06 ± 0.01
GRAD	2.3 ± 0.2	0.9 ± 0.2	0.9 ± 0.1	1.0 ± 0.1	0.2 ± 0.01
M0	2.3 ± 0.1	1.3 ± 0.2	1.0 ± 0.1	1.0 ± 0.1	0.5 ± 0.1
M1	2.1 ± 0.1	1.6 ± 0.2	0.9 ± 0.1	1.0 ± 0.1	0.8 ± 0.1
M2	1.9 ± 0.1	3.0 ± 0.7	0.9 ± 0.1	0.9 ± 0.1	0.5 ± 0.1
M3	1.9 ± 0.1	3.0 ± 0.8	0.9 ± 0.1	0.9 ± 0.1	1.0 ± 0.3
M4	2.1 ± 0.1	2.1 ± 0.5	0.9 ± 0.1	1.0 ± 0.1	0.8 ± 0.2
M5	2.0 ± 0.1	0.9 ± 0.1	0.9 ± 0.1	1.0 ± 0.1	0.3 ± 0.1

* Errors for the model parameters are the 95 % confidence interval for fit.

Nevertheless, we note that k_{Qp} is generally higher for the managed PHOLEDs than that for CONV or GRAD, possibly resulting from energy levels arising from multiple species. This is offset by the relatively small density of Q_A in the managed PHOLEDs, additional exciton generation via Q_B (**Eq. (6.3)** in **§6.2.3**), and reduced exciton loss due to the smaller k_{QN}.

Compared to CONV and GRAD, the managed PHOLEDs have a lower rate of exciton-defect interactions (k_{QN}), indicating that fewer excitons are eliminated due to the quenching by Q_A (**Fig. 6.5 (b)**). Now, $k_{QN} \cong 2.0 \times 10^{-11}$ cm^3/s of the aged PHOLEDs is larger by nearly two orders of magnitude than the TTA rate of $k_{TT} \cong 1.0 \times 10^{-13}$ cm^3/s obtained from the transient PL of the as-grown PHOLED EML. This implies that the reduction of luminance over time is

severely impacted by defect-related exciton loss compared to increased TTA, while the latter reaction still plays a critical role in triggering molecular dissociation reactions.

Figure 6.5 (c) shows $\Delta V_{EML}(t)/V_0$ and $\Delta V_{ext}(t)/V_0$ for CONV, GRAD and managed PHOLEDs. These are the relative contributions to the total voltage rise induced by defects within and outside of the EML (i.e., $Q_A + Q_B$ and Q_{ext}, respectively) at t = 100 hr with respect to V_0, the initial operating voltage needed to achieve L_0. CONV and GRAD have relatively high $\Delta V_{EML}(t)$ compared to the managed devices due to the higher defect densities in the EML. Note that the relative contributions to the total voltage rise are dominated by Q_{ext} for the more resistive devices (i.e. GRAD and managed PHOLEDs compared to CONV), which also have a slightly higher V_0. Due to the lack of this consideration, previous models [33] underestimated $\Delta V(t)$ or added an arbitrary constant voltage [50] to explain the discrepancy between the model and measurement.

The generation rate of Q_{ext} that produces $\Delta V_{ext}(t)$ is k_{Qext}, which is generally higher for the managed PHOLEDs than CONV and GRAD. This results from the higher resistivity of the devices due to thick EML, as well as the lower hole mobility of the manager relative to that of the blue dopant (**Fig. 6.3(b)**). Using a simple approximation based on space-charge-limited transport [64], the mobility in the managed EML is reduced by ~20% compared to that of the GRAD EML. Due to the limited hole transport in the managed devices, the polaron density in the HTL is increased, accelerating degradation [156], [157].

In summary, $L(t)/L_0$ is accurately modeled by assuming the formation of both deep (Q_A) and shallow defects (Q_B) in the EML. To fully account for $\Delta V(t)$, however, defects formed in other non-luminescent layers of the PHOLEDs (Q_{ext}) were also considered.

Finally, we note that hot state management strategies proposed here may also be useful in extending the lifetime of OLEDs based on TADF. Similar to electrophosphorescence, TADF is

based on the generation of triplets with natural lifetimes [36] typically > 5 μs. Hence, these devices should, in principle, undergo the same degradation process as PHOLEDs. Indeed, to date TADF OLEDs have shown lifetimes considerably shorter than those based on electrophosphorescence, with the problem once more being particularly acute for blue emission.

6.6. Conclusions

We demonstrated a strategy to manage hot excited states that otherwise lead to dissociative reactions and deteriorate the operational stability of blue PHOLEDs. By introducing excited state manager molecules into the PHOLED EML, we achieve to our knowledge the longest lifetime reported thus far for blue-emitting devices. Our findings emphasize the importance of physics-based solutions such as excited state management or similar approaches to further improve the lifetime of blue PHOLEDs. While such solutions are essential, they must be accompanied by the development of highly stable dopants, managers, hosts and transport materials; a challenge made all the more difficult by the very wide energy gaps required for blue PHOLEDs. The properties required for successful manager molecules are, therefore: (i) high molecular stability, (ii) a wide energy gap intermediate between that of the host and dopant molecules and their hot excited states, (iii) significant molecular orbital overlap with the EML components to ensure rapid energy transfer prior to molecular degradation, along with morphological properties that can assist in charge transport. We also developed a phenomenological model that establishes the roles and characteristics of defects present in the device, providing a convincing fit to the time dependence of both luminance decay and voltage rise of managed and unmanaged blue PHOLEDs. Direct spectroscopic measurements of defect characteristics can be useful in determining their energetic properties as well as their chemical

origins. This will provide meaningful information to develop a suite of stable manager materials, enabling even longer-lived and deeper blue PHOLEDs than those reported here.

Chapter 7 Future work

7.1. Mechanically stacked, white phosphorescent organic light-emitting diodes

For solid-state lighting, it is desirable to develop highly efficient, long-lived white phosphorescent organic light-emitting diodes (WOLED). The selected combination of red, green, and blue, or yellow and blue PHOLEDs should produce white light with the desired color quality, i.e., CIE coordinate, color temperature (CT) and color rendering index (CRI). Color stability is an important performance metric for white-emitting devices and should remain unchanged during continuous operation until at least up to T70. However, due to the accelerated luminance degradation of the blue-emitting cells compared to red- or green-emitting ones, the color of WOLED emission will likely turn yellowish after use. Therefore, it is required to adjust the luminance of the each cell during operation to maintain the color quality of white light. However, this is not easily achieved in conventional stacked WOLEDs where individual cells are serially connected and operated by the same drive current.

Here, we propose an idea of independently operated blue and yellow PHOLEDs that are mechanically stacked, and their cathodes are electrically connected through the metal conductor. This results in a three-channel WOLED with controllable color. **Figure 7.1** demonstrates a schematic diagram for unidirectional and bidirectional emission, mechanically stacked WOLEDs (MS-WOLED).

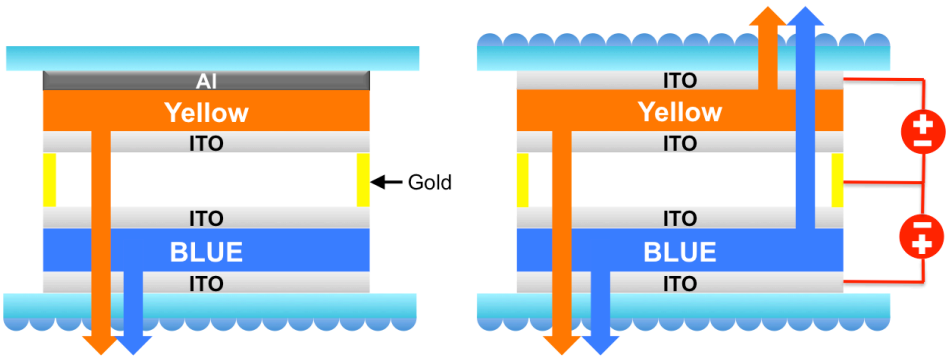

Figure 7.1 Structures of mechanically stacked white OLEDs.

Here, blue and yellow PHOLEDs are fabricated on individual transparent substrates, and are stacked such that their electrodes are electrically connected via cold-welded gold that is patterned along the edges of the top electrodes of both devices. Note that the width of the gold connector should be sufficiently thin to ensure a large device aperture ratio, and its thickness should minimize the optical loss. Sharing a common ground, devices in the MS-WOLED can be operated by different anode channels so that the luminance of individual devices can be independently controlled to produce white light with the desired color coordinates.

Depending on the device structure, the MS-WOLED can produce either unidirectional or bidirectional light emission. For both types, at least one PHOLED should be transparent, while the other device can have a transparent electrode for one side and with a reflective metal or transparent electrode for the other side, resulting in unidirectional or bidirectional MS-WOLEDs, respectively.

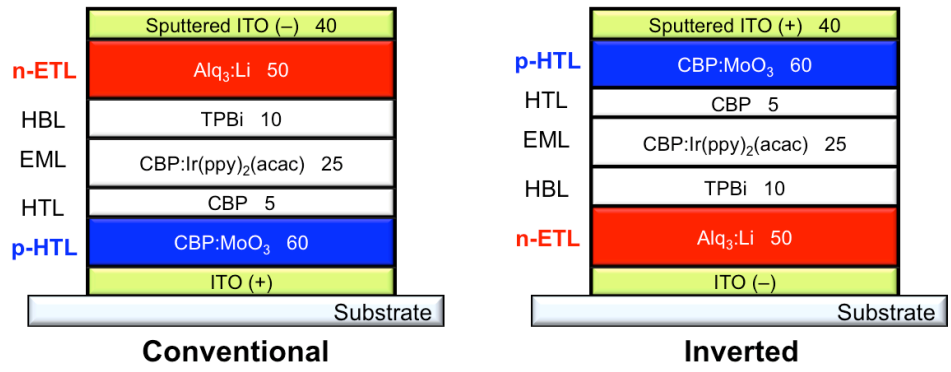

Figure 7.2 Structures of transparent, green-emitting PHOLEDs.

Figure 7.2 shows the transparent PHOLED structures that can be employed in the MS-WOLEDs. Transparent PHOLED structures employ ITO both as the anode and cathode, while the inverted structure has the organic layers deposited in reverse order compared to the conventional one. Here, we dope the transport layers to increase conductivity, resulting in p–type or n–type doped HTL (p–HTL) or ETL (n–ETL), respectively. Thus, hole or electron injection from electrodes into the p–HTL or n–ETL is achieved via tunneling, which does not significantly impact the device conductivity and thus the efficiency of the PHOLEDs [158]. The additional advantage of conductivity doping is that we can make the p–HTL or n–ETL thick without significantly increasing the device resistivity. The thick doped transport layers prevent damage to the EML induced by ITO sputtering, which otherwise negatively affects the device performance.

Figure 7.3 shows the current density (*J*)–voltage (*V*) characteristics of conventional and inverted transparent PHOLEDs, denoted as Conv and Inv, respectively with structures given in **Fig. 7.2**. The inset of **Fig. 7.3** shows the electroluminescence (EL) spectra of the transparent PHOLEDs measured from the substrate side and from the sputtered ITO electrode side, denoted

as Bottom and Top, respectively. This notation similarly applies to the measured EQE shown in **Fig. 7.4** (see below).

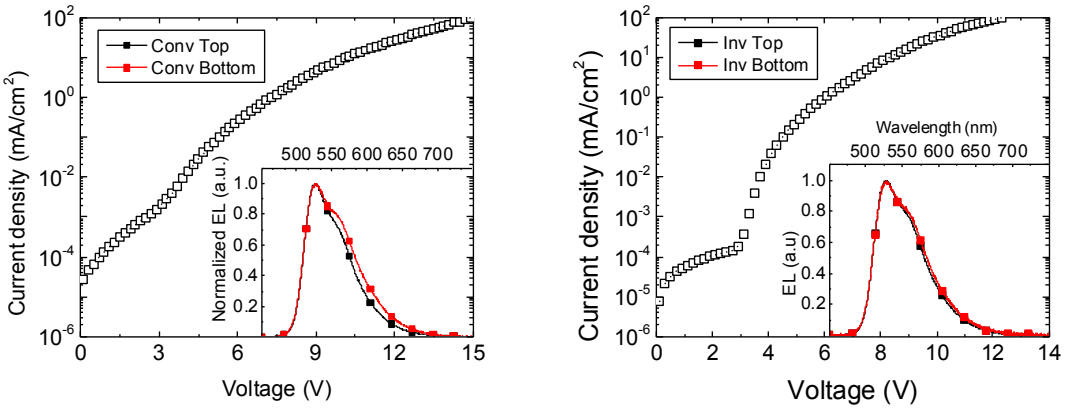

Figure 7.3 Current density vs. voltage of conventional and inverted transparent PHOLEDs. Inset: EL spectra of top and bottom emission of each device type.

Both Conv and Inv devices show slight variations in their EL spectra between Bottom and Top emission due to the microcavity effect. This can be controlled by modifying the thickness of the p–HTL or n–ETL so that the optical resonance can be engineered without impacting the electrical characteristics of the devices [159].

Figure 7.4 shows the EQE of bottom and top transparent PHOLEDs along with their summed values, denoted as Bottom, Top, and Total, respectively. For both structures, the total EQE is nearly comparable to that measured from conventional PHOLEDs having a reflective metal and transparent electrodes for unidirectional light extraction. Thus, the given transparent PHOLED structures with either direction of deposition can be adopted in the MS-WOLEDs without inducing any potential electrical or optical losses.

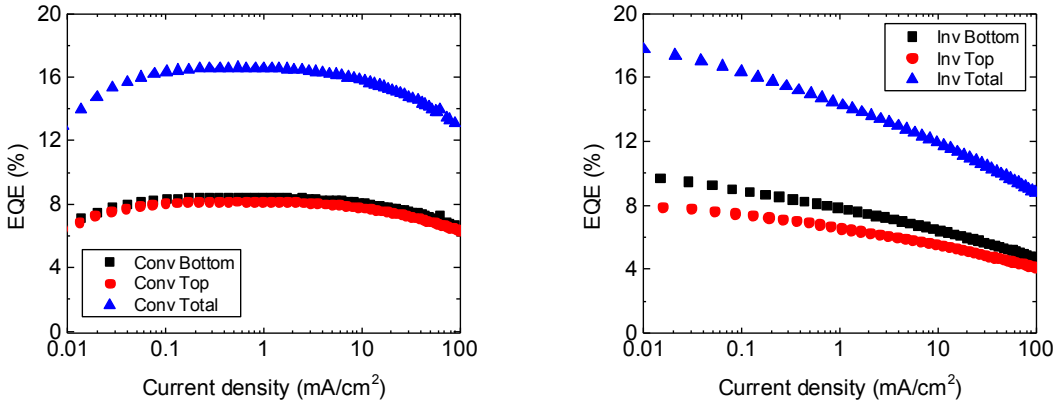

Figure 7.4 EQE vs. current density of conventional and inverted transparent PHOLEDs.

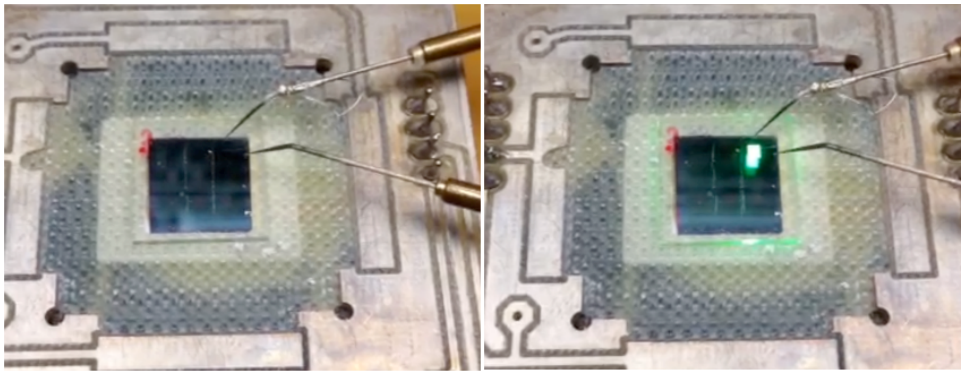

Figure 7.5 Pictures of the operating transparent PHOLED pixel.

Figure 7.5 shows the pictures of the transparent PHOLED pixel when it is off and on under room light. The device emission from the top is directly seen while the bottom emission is deflected by the photodiode placed underneath. When the device is not operating, the photodetector can be seen through the device due its high transparency. Therefore when used in MS-WOLEDs, the transparent PHOLED does not absorb emission produced from the other paired device. Finally, since MS-WOLEDs have two substrates attached with their devices

facing inwards, we can apply epoxy along their edges for encapsulation without needing additional barrier glass to prevent oxygen and water penetration. The outcoupling methods such as microlens arrays can be used to boost the efficiency [101] (see **Fig. 7.1**).

7.2. Triplet exciton quenching for long-lived blue PHOLEDs

It has been shown that the reduction of bimolecular annihilation is crucial for improving the operational stability of blue PHOLEDs [33], [50]. In the PHOLED EML, the long natural decay time of the triplet exciton (τ > 1 μs) leads to its diffusion over long distances. The long-lived triplet exciton has a higher probability of finding another active excited state to annihilate.

Figure 7.6 shows the modeled luminance degradation of a blue PHOLED with varying decay times of the triplet exciton (τ). Other parameters used to generate the response are fixed and were extracted from the model used for the managed PHOLEDs (see **Chapter 6**). If τ decreases from 1.5 μs to 0.9 μs, the device operational lifetime, T80, is significantly increased from 110 hr to 465 hr, resulting in a fourfold improvement.

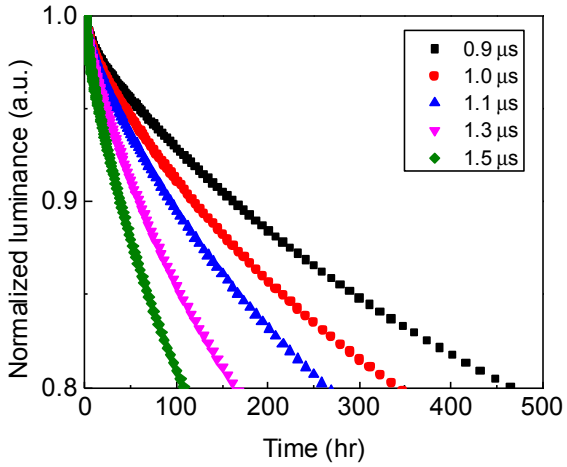

Figure 7.6 Luminance degradation of PHOLED as a function of triplet natural lifetimes.

There are multiple approaches to reduce τ: (i) design the blue phosphorescent emitter with an enhanced metal-ligand charge transfer character [71] (see **Chapter 4**), (ii) optically modify the device structure with an increased Purcell factor, or (iii) provide an additional energy transfer pathway for the triplets. Approach (i) is challenging because molecules with good luminescence characteristics, molecular stability, as well as a large energy gap for blue emission are difficult to design, since these properties are not compatible with each other. Approach (ii) requires a change in the distance of the emission zone to the metal cathode by a significant amount (>100 nm) in the conventional PHOLED structure, or adding components such as thin metal electrodes or distributed Bragg reflectors (DBR) that can modify the optical resonances of the device. This generally makes the device emission dependent on the wavelength and viewing angle.

Here, we propose a means for approach (iii) by introducing an extremely small amount (<0.5 vol%) of stable, triplet exciton quenching molecules in the blue PHOLED EML. This so-called "quenching manager" should have a lower triplet energy than that of the blue dopant to allow for exothermic triplet transfer, should be stable, and should not allow light emission from the triplet states. The Liq molecule can be a potential candidate for this purpose. It has been reported that the thin Liq layer was inserted between the EML and the HBL of the TADF OLED, resulting in a tenfold lifetime improvement (see below) [37].

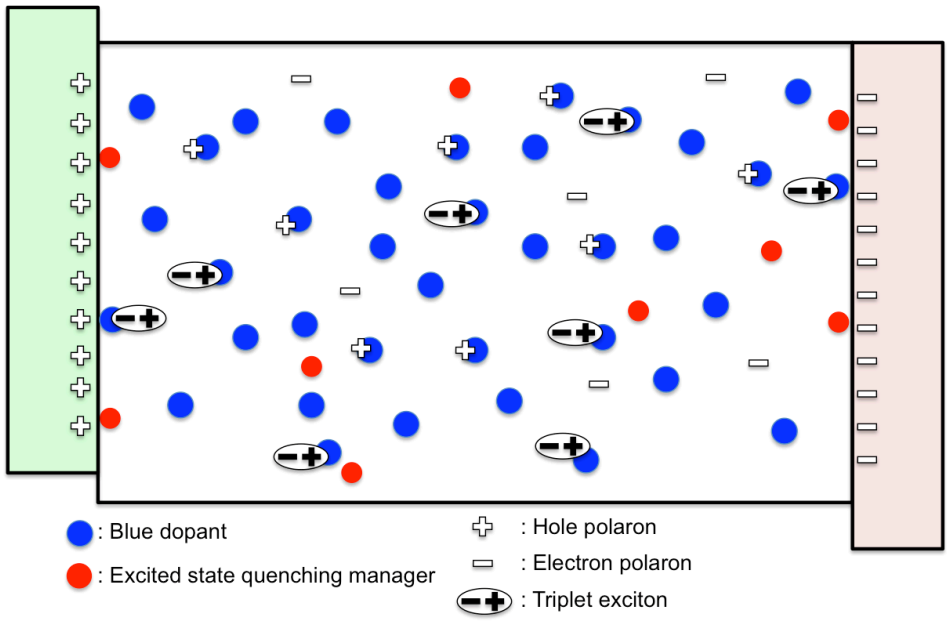

Figure 7.7 Schematic diagram of PHOLED EML containing triplet exciton quenchers. In the given EML system, hole polarons injected from the HTL are transported via the blue dopant and electron polarons injected from the ETL are transported via the host. Exciplex states are then formed between the hole on the blue dopant and electron on the host, which are subsequently transferred to the triplet states on the blue dopant. Triplet exciton quenching manager molecules are lightly doped (<0.5 vol%) to eliminate the excessive number of triplet excitons and thus to reduce their "effective" natural decay time.

Figure 7.7 shows the schematic EML of blue PHOLEDs with hole transport (HTL) and electron transport layers (ETL). At a high brightness (L_0 > 1,000 cd/m^2) an excess number of excitons are generated more than needed, potentially leading to bimolecular annihilation. Thus, even the small fraction of quenching managers can efficiently eliminate triplet excitons so that their "effective" natural decay time is reduced. To maximize lifetime without significantly altering the device conductivity, the quenching manager is locally doped only in the zone of the EML where the triplet exciton density is the highest.

In addition, the quenching manager can be inserted at the EML interfaces adjacent to the HTL and ETL. There exist potential barriers for hole and electron polarons at such interfaces where the polarons are likely to accumulate, leading to the high likelihood of their interaction with excitons in the EML. Degradation of the organic/organic interface has been reported, which is attributed to the charge accumulation at interfaces and is accelerated if excitons are present nearby within the TPA interaction radius [144]. The EML interface is where charge injection and blocking of the opposite charges and excitons occur that critically impact the device performance. Thus, the interfacial degradation may degrade the device stability more severely than that occurring in the bulk of the EML.

By inserting the quenching manager at the EML interface, the triplet excitons can be eliminated before they interact with the charges via TPA and the operational stability of the device will improve. Employing a similar approach, a nearly tenfold improvement of the lifetime has been achieved in green TADF OLEDs [37] (T90 = 175 → 1115 hr).

A major drawback of using the quenching manager is that it can also reduce the radiative recombination rate of the triplet excitons along with the bimolecular annihilation, leading to reduced device efficiency. The device having the quenching manager may require a higher drive current density (J) to achieve the target brightness. Increased J promotes the TTA and TPA due to a high density of excited states.

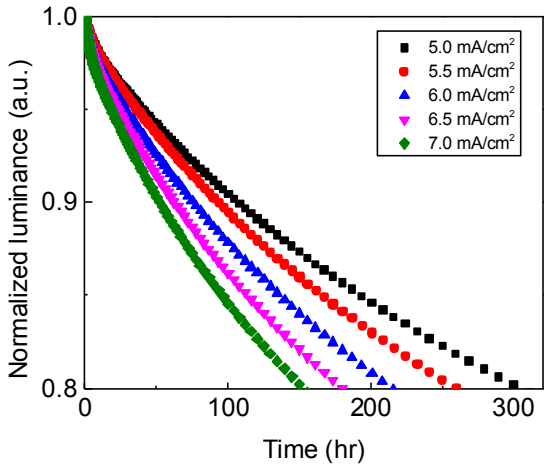

Figure 7.8 Luminance degradation of PHOLED as a function of driving current densities.

Figure 7.8 shows the modeled luminance degradation of a blue PHOLED. As *J* increases from 5.0 mA/cm^2 to 7.0 mA/cm^2, T80 decreases from 305 hr to 150 hr. However, we note that this calculation does not take into consideration the interfacial protection and reduction in the triplet decay time that are potential advantages expected by having the quenching manager. If such a positive impact of the quenching manager overwhelms the negative one induced by the reduction of the device efficiency, the overall operational lifetime of the device will be improved. More importantly, the investigation of the device with the quenching manager at the EML interface will provide important clues to understand the impact of the interfacial degradation on the device performance, e.g. the change of charge injection or blocking leading to the charge imbalance, or loss of exciton blocking ability, and also the impact of interfacial TPA reduction on the operational stability of the PHOLEDs.

APPENDIX A Raytracing algorithm for PHOLED concentrator

A.1. Algorithm and assumptions used for the tray-tracing simulation

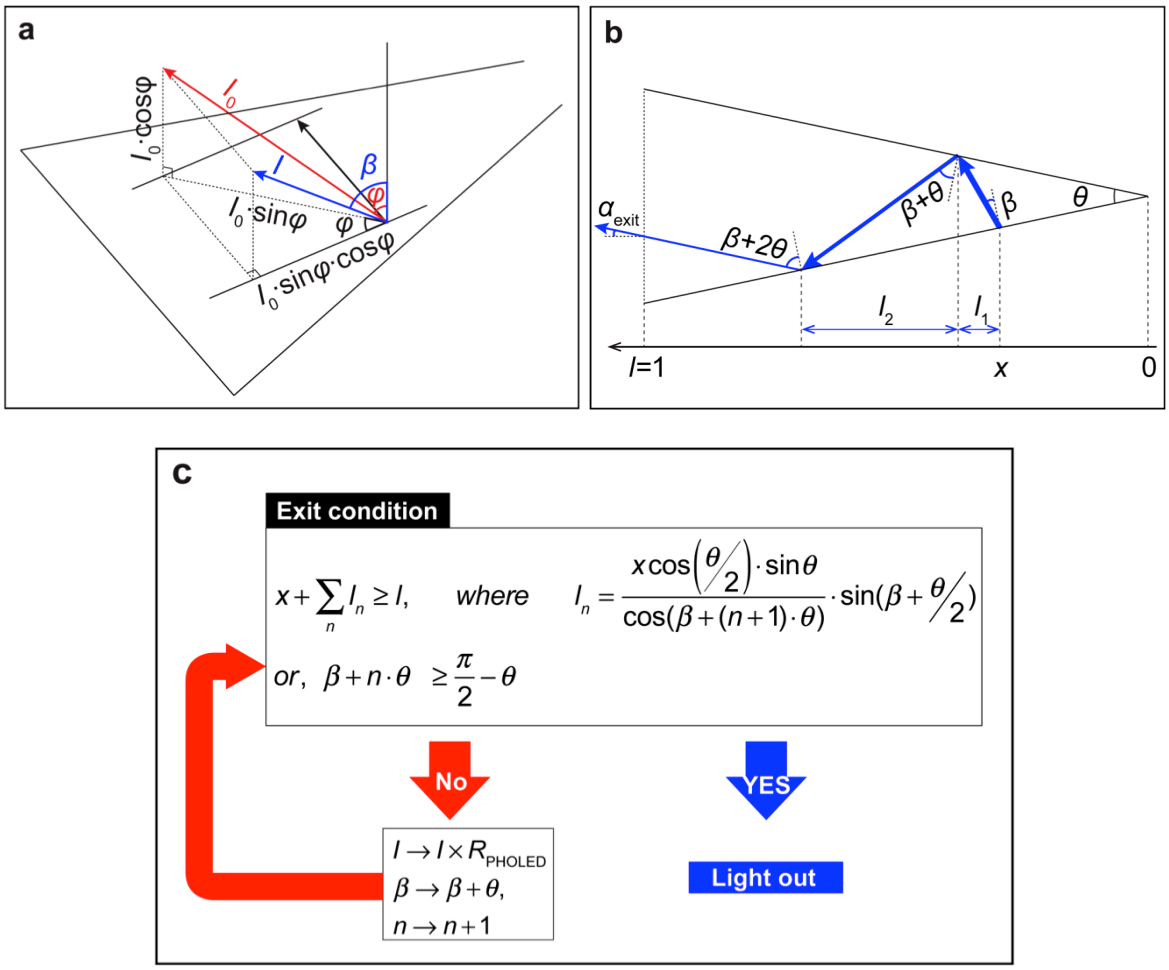

Figure A1. Ray-tracing algorithm for the single panel concentrator device.

(a) Decomposition of the ray with initial intensity, I_0, at the polar angle, φ, and the azimuthal angle, ϕ, with respect to the normal and the median of the concentrator panel, respectively. The forward component is directed toward the aperture (blue), and the lateral component is confined within the concentrator (black), being reflected by adjacent device panels and attenuated. Here, φ

and ϕ are varied from -90° to 90° and 0° to 180°, respectively. (b) Ray tracing of the forward component, I , at an initial emission angle, β, with respect to the normal of the concentrator panel. Note that the original intensity I_0 of the ray emitted at an arbitrary position x from the vertex of the concentrator satisfies the Lambertian distribution (see Figure 4 in text), and its forward compoenent intensity I and emission angle β are determined *vs*. φ and ϕ. As the ray is reflected by the opposing panel, its intensity is attenuated by the PHOLED reflectance, R_{PHOLED}, and its reflected angle is increased by the apex angle, θ, of the concentrator. Then the ray travels the length, l_{n} until the next reflection. The height of the concentrator, l, is set to unity. The exit angle, α_{exit}, of the ray escaping through the aperture is defined with respect to the central axis of the concentrator, which determines the final angular distribution profile. (c) Schematic of the ray-tracing algorithm. The ray can escape through the aperture only if it fulfills the exit condition: the total travel length added to the initial emission position x must be greater than l, or the initial or reflected emission angle is larger than $\pi/2–\theta$ so that it does not meet the opposing panel. Each traced ray contains information about its final intensity, exit angle, and the number of reflections up to extraction.

The simulation is based on a single-wavelength and fixed reflectance R_{PHOLED} independent of the incident angle, and does not include optical effects other than reflection.

A.2. Method for calculating the PHOLED reflectance

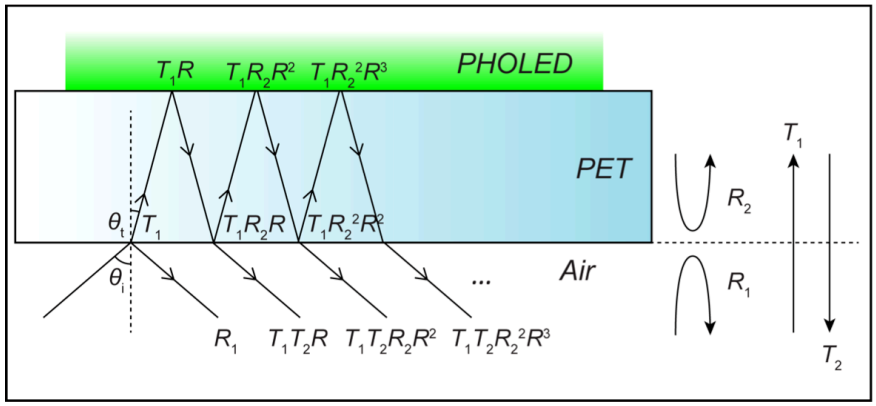

Figure A2. Schematic of the PHOLED reflectance and transmittance.

The total reflectance of the PHOLED including the PET substrate is as follows:

$$R_{PHOLED}(\theta_i) = R_1(\theta_i) + T_1(\theta_i)T_2(\theta_t)R(\theta_t) + T_1(\theta_i)T_2(\theta_t)R_2(\theta_t)R^2(\theta_t) + \cdots \quad \text{(A.1)}$$

where R_1 and R_2 are the fractions of the incident energy reflected back to the air and the PET by the air/PET interface, T_1 and T_2 are the transmitted fractions into the PET and air, respectively, and R is the reflectance of the PHOLED structure calculated using the transfer matrix method. Now, **Eq. (A.1)** is rewritten as:

$$R_{PHOLED}(\theta_i) = R_1(\theta_i) + \frac{T_1(\theta_i)T_2(\theta_t)R(\theta_t)}{1 - R_2(\theta_t)R(\theta_t)} \quad \text{(A.2)}$$

The transverse electric (TE) and transverse magnetic (TM) mode reflectance are calculated separately according to **Eq. (A.2)** and averaged with the assumption that the incident PHOLED emission is unpolarized. Structures of the Device A and Device B discussed in the text are as follows:

Device A: ITO 100 nm / 15 vol. % MoO_3 doped into CBP 60 nm / CBP 10 nm / 8 vol. % doped in $Ir(ppy)_2(acac)$ into CBP 15 nm / TPBi 65 nm / LiF 1.5 nm / Al 150 nm

Device B: ITO 100 nm / 15 vol. % MoO_3 doped into CBP 60 nm / CBP 10 nm / 8 vol. % doped into $Ir(ppy)_2(acac)$ in CBP 15 nm / TPBi 10 nm / 2 vol. % doped Li in Bphen 55 nm / 8-hydroxyquinolinato lithium (Liq) 1.5 nm / Ag 150 nm

APPENDIX B Test of lifetime model

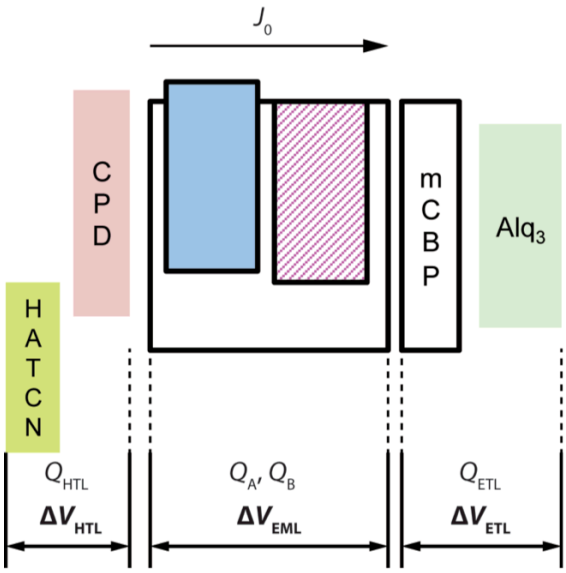

Figure B1. Schematic diagram of the PHOLED structure with defects.

The TTA model requires the use of 5 independent variables; k_{QN}, k_{QA}, k_{QB}, k_{QP} and k_{Qext}. While this is the same as used in previous TTA/TPA analyses, it is essential to test the uniqueness of the fits to the data in **Fig. 6.4**. **Figure B1** shows the possible locations of defects formed in the PHOLED structure. Defect densities in the hole transport layer (HTL), EML, and the electron transport layer (ETL) are Q_{HTL}, Q_{EML}, and Q_{ETL}, respectively. In the model, these defects are formed outside of the EML and hence are simply lumped into a single, external defect density, $Q_{ext} = Q_{HTL} + Q_{ETL}$. The defects trap holes, and depending on their locations and the densities, they contribute to the operational voltage rise, $\Delta V(t)$, via:

$$\Delta V(t) = \Delta V_{EML}(t) + \Delta V_{HTL}(t) + \Delta V_{ETL}(t)$$
$$= \frac{q}{\varepsilon_0 \varepsilon_r}\left(\int_{EML} Q_{EML}(x,t)dx + \int_{HTL} Q_{HTL}(x,t)dx + \int_{ETL} Q_{ETL}(x,t)dx\right) \quad \text{(B.1)}$$
$$= \frac{q}{\varepsilon_0 \varepsilon_r}\left(\int_{EML} Q_A(x,t) + Q_B(x,t)dx + \int_{ext} Q_{ext}(x,t)dx\right)$$

Figure B2 shows the contributions of the various defects to the fits. The lifetime data, i.e. time evolution of the luminance degradation and the voltage rise, of the managed PHOLED M1 is used as an example.

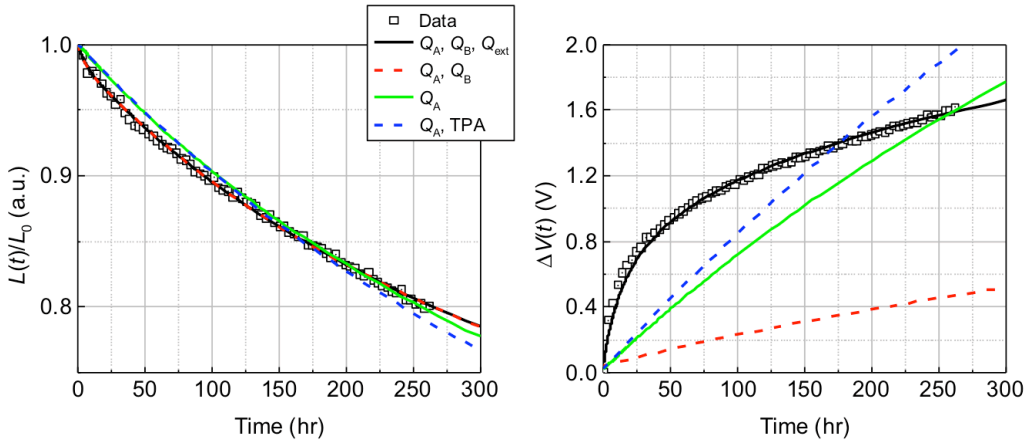

Figure B2. Lifetime model fit based on different combinations of defects. The squares show time evolution of the measured luminance (left) and operating voltage (right).

Compared to the model with a complete set of defects (black solid line, see text), the one excluding Q_{ext} (red dashed line) underestimates $\Delta V(t)$, while providing a reasonable fit for $L(t)/L_0$. This is because $L(t)/L_0$ is affected only by the defects *within* the EML ($Q_{EML} = Q_A + Q_B$), as well as the electrons, holes, and excitons whose densities are determined by the constant current density of J_0 and the measured recombination profile of $G(x) = J_0/e \cdot N(x) \Big/ \int_{EML} N(x)dx$. On the other hand, the voltage rise due to defects Q_A and Q_B within the EML [$\Delta V_{EML}(t)$] is

insufficient to account for the measured $\Delta V(t)$ (see **Fig. 6.4**). Thus the defects present outside of the EML [$\Delta V_{ext}(t)$] need to be included.

If only one type of EML defect (Q_A) is assumed to be active along with Q_{ext}, the fit for both $L(t)/L_0$ and $\Delta V(t)$ significantly deviates from the data. This necessitates the inclusion of shallow defects (Q_B) that trap charges but also contribute to the PHOLED luminescence via transfer back to the dopant molecule (see text). Finally, the fit from the model [33] assuming only Q_A and triplet-polaron annihilation (TPA) for the defect generation is also shown to deviate from data.

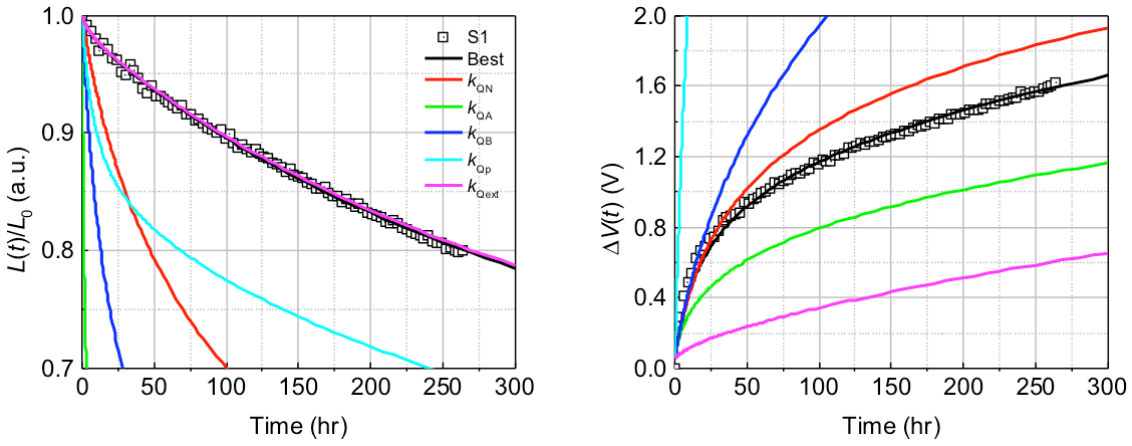

Figure B3. Lifetime model fit by changing a single parameter while fixing others. The squares are data for time evolution of the luminance (left) and operating voltage (right).

Figure B3 shows the sensitivity to variations of a single fitting parameter used in the lifetime model. From the calculated set of parameters (yielding the black solid line, denoted as "Best"), each parameter is modified by an order of magnitude within the bounds for the fit, while the other parameters are fixed. The results show that the changes in k_{QN}, k_{QA}, k_{QB} and k_{QP} result in significant deviations from the measurements. k_{Qext} does not affect $L(t)/L_0$ whereas it strongly influences $\Delta V(t)$, consistent with the data shown in **Fig. B2**.

Note that the initial values (I.V.) chosen for the fitting parameters are set within the upper and lower bounds that are an order of magnitude larger or smaller, respectively, relative to the final parameters providing the best fit (see **Table 6.3**). The fitting parameters with arbitrary I.V. within such boundary conditions (B.C.) converge to the final values reported, while if I.V. of one or more parameters are set outside the given B.C. lead to different values with an unacceptably poor fit to the data.

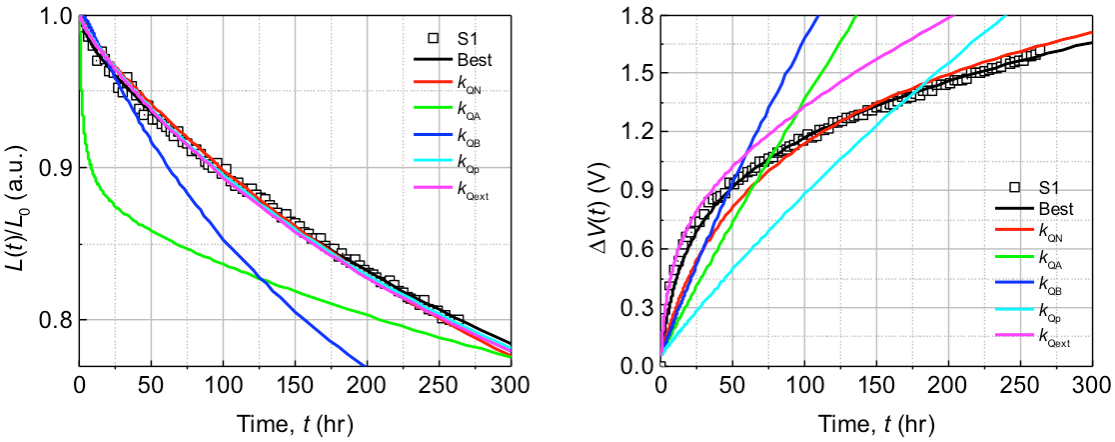

Figure B4. Lifetime model fit by changing a single parameter, while varying others. The squares are data for time evolution of the luminance (left) and operating voltage (right).

We also forced a single parameter to be smaller or larger by an order of magnitude relative to its final value, and the induced discrepancy in the fit was attempted to be compensated by varying the remaining four parameters. **Figure B.4** shows that all the resulting simulations cannot fit the voltage rise, while some of those with changed k_{QN}, k_{Qp} and k_{Qext} are in a reasonable agreement with the luminance degradation. However, considering that these fitting parameters are derived from coupled equations that should predict *both* the lifetime and voltage characteristics, the models that satisfy only one of these two characteristics are not accepted.

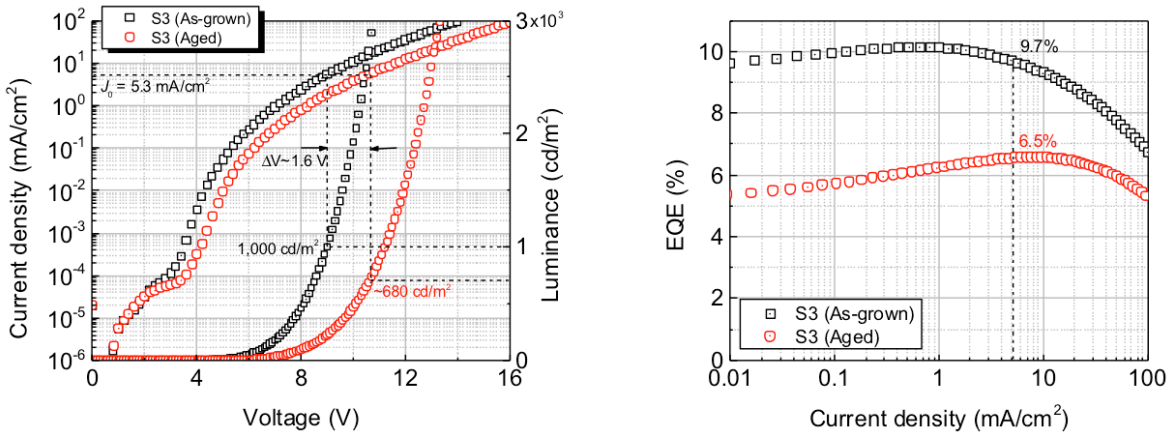

Figure B5. Current density-voltage-luminance and EQE-current density characteristics of as-grown and aged PHOLEDs.

Figure B5 shows the *J–V–L* and EQE–*J* characteristics of as-grown (fresh) and aged managed M3 PHOLEDs. The aged M3 was driven at J_0 = 5.3 mA/cm^2 for ~550 hr, at which point the initial luminance of L_0 = 1,000 cd/m^2 decreases by 32%. The device performance for these devices is summarized in the **Table B1**.

Table B1. EL characteristics of as-grown and aged PHOLED M3

Device	J_0 (mA/cm^2)	t (hr)	CIE*	$V(t)$ (V)	EQE(t) (%)	$L(t)$ (cd/m^2)
M3 (As-grown)	5.29	0	(0.16, 0.30)	9.0	9.7	1,000
M3 (Aged)	5.29	~550	(0.16, 0.30)	10.6	6.5	~680

* Measured at J = 5 mA/cm^2.

The *J-V* characteristics of the aged M3 PHOLED compared to the as-grown device show both parallel translation towards higher voltage and a slight decrease in slope. These trends indicate of the existence of the traps and consequent reduced "effective" mobilities of the materials comprising the devices. For simplicity, extrinsic factors such as degradation of the

electrodes are not considered. In the EQE-*J* characteristics, the reduced efficiency is attributed to nonradiative recombination by the defects at low *J* and the exciton quenching at higher *J*.

REFERENCES

[1] P. Peumans, S. Uchida, and S. R. Forrest, "Efficient bulk heterojunction photovoltaic cells using small-molecular-weight organic thin films," Nature, vol. 425, no. 6954, pp. 158–162, Sep. 2003.

[2] C. W. Tang and S. A. VanSlyke, "Organic electroluminescent diodes," Appl. Phys. Lett., vol. 51, no. 12, pp. 913–915, Sep. 1987.

[3] G. Horowitz, "Organic Field-Effect Transistors," Adv. Mater., vol. 10, no. 5, pp. 365–377, Mar. 1998.

[4] S. M. Sze, Physics of Semiconductor Devices. John Wiley & Sons, 1981.

[5] J. L. Schmit, "Growth, properties and applications of HgCdTe," J. Cryst. Growth, vol. 65, no. 1, pp. 249–261, Dec. 1983.

[6] A. Köhler and H. Bässler, Electronic Processes in Organic Semiconductors: An Introduction. John Wiley & Sons, 2015.

[7] E. A. Silinsh, Organic Molecular Crystals: Their Electronic States. Springer Science & Business Media, 2012.

[8] C.-T. Sah, Fundamentals of Solid-state Electronics. World Scientific, 1991.

[9] F. London, "The general theory of molecular forces," Trans. Faraday Soc., vol. 33, no. 0, p. 8b–26, 1937.

[10] V. Coropceanu, J. Cornil, D. A. da Silva Filho, Y. Olivier, R. Silbey, and J.-L. Brédas, "Charge Transport in Organic Semiconductors," Chem. Rev., vol. 107, no. 4, pp. 926–952, Apr. 2007.

[11] N. Karl, "Charge carrier transport in organic semiconductors," Synth. Met., vol. 133–134, pp. 649–657, Mar. 2003.

[12] P. I. Djurovich, E. I. Mayo, S. R. Forrest, and M. E. Thompson, "Measurement of the lowest unoccupied molecular orbital energies of molecular organic semiconductors," Org. Electron., vol. 10, no. 3, pp. 515–520, May 2009.

[13] M. D. Sturge, "Optical Absorption of Gallium Arsenide between 0.6 and 2.75 eV," Phys. Rev., vol. 127, no. 3, pp. 768–773, Aug. 1962.

[14] J. F. Muth et al., "Absorption coefficient, energy gap, exciton binding energy, and recombination lifetime of GaN obtained from transmission measurements," Appl. Phys. Lett., vol. 71, no. 18, pp. 2572–2574, Nov. 1997.

[15] P. Hervé and L. K. J. Vandamme, "General relation between refractive index and energy gap in semiconductors," Infrared Phys. Technol., vol. 35, no. 4, pp. 609–615, Jun. 1994.

[16] C.-J. Chiang, S. Bull, C. Winscom, and A. Monkman, "A nano-indentation study of the reduced elastic modulus of Alq_3 and NPB thin-film used in OLED devices," Org. Electron., vol. 11, no. 3, pp. 450–455, Mar. 2010.

[17] J. Kim, D. (Dan) Cho, and R. S. Muller, “Why is (111) Silicon a Better Mechanical Material for MEMS?,” in Transducers ’01 Eurosensors XV, Springer Berlin Heidelberg, 2001, pp. 662–665.
[18] B. A. Miller-Chou and J. L. Koenig, “A review of polymer dissolution,” Prog. Polym. Sci., vol. 28, no. 8, pp. 1223–1270, Aug. 2003.
[19] P. E. Burrows et al., “Organic vapor phase deposition: a new method for the growth of organic thin films with large optical non-linearities,” J. Cryst. Growth, vol. 156, no. 1, pp. 91–98, Nov. 1995.
[20] S. R. Forrest, “The path to ubiquitous and low-cost organic electronic appliances on plastic,” Nature, vol. 428, no. 6986, pp. 911–918, Apr. 2004.
[21] B. Song, C. Rolin, J. D. Zimmerman, and S. R. Forrest, “Effect of Mixed Layer Crystallinity on the Performance of Mixed Heterojunction Organic Photovoltaic Cells,” Adv. Mater., vol. 26, no. 18, pp. 2914–2918, May 2014.
[22] B. Song, Q. C. Burlingame, K. Lee, and S. R. Forrest, “Reliability of Mixed-Heterojunction Organic Photovoltaics Grown via Organic Vapor Phase Deposition,” Adv. Energy Mater., vol. 5, no. 8, p. 1401952, Apr. 2015.
[23] R. R. Lunt, B. E. Lassiter, J. B. Benziger, and S. R. Forrest, “Organic vapor phase deposition for the growth of large area organic electronic devices,” Appl. Phys. Lett., vol. 95, no. 23, p. 233305, Dec. 2009.
[24] Y. Sun, M. Shtein, and S. R. Forrest, “Direct patterning of organic light-emitting devices by organic-vapor jet printing,” Appl. Phys. Lett., vol. 86, no. 11, p. 113504, Mar. 2005.
[25] M. Shtein, P. Peumans, J. B. Benziger, and S. R. Forrest, “Direct, Mask- and Solvent-Free Printing of Molecular Organic Semiconductors,” Adv. Mater., vol. 16, no. 18, pp. 1615–1620, Sep. 2004.
[26] G. J. McGraw, D. L. Peters, and S. R. Forrest, “Organic vapor jet printing at micrometer resolution using microfluidic nozzle arrays,” Appl. Phys. Lett., vol. 98, no. 1, p. 13302, Jan. 2011.
[27] M. Pope, H. P. Kallmann, and P. Magnante, “Electroluminescence in Organic Crystals,” J. Chem. Phys., vol. 38, no. 8, pp. 2042–2043, Apr. 1963.
[28] C. W. Tang, S. A. VanSlyke, and C. H. Chen, “Electroluminescence of doped organic thin films,” J. Appl. Phys., vol. 65, no. 9, pp. 3610–3616, May 1989.
[29] M. A. Baldo, D. F. O’Brien, M. E. Thompson, and S. R. Forrest, “Excitonic singlet-triplet ratio in a semiconducting organic thin film,” Phys. Rev. B, vol. 60, no. 20, pp. 14422–14428, Nov. 1999.
[30] M. A. Baldo et al., “Highly efficient phosphorescent emission from organic electroluminescent devices,” Nature, vol. 395, no. 6698, pp. 151–154, Sep. 1998.
[31] C. Adachi, M. A. Baldo, M. E. Thompson, and S. R. Forrest, “Nearly 100% internal phosphorescence efficiency in an organic light-emitting device,” J. Appl. Phys., vol. 90, no. 10, pp. 5048–5051, Nov. 2001.

[32] D. Y. Kondakov, T. D. Pawlik, T. K. Hatwar, and J. P. Spindler, "Triplet annihilation exceeding spin statistical limit in highly efficient fluorescent organic light-emitting diodes," J. Appl. Phys., vol. 106, no. 12, p. 124510, Dec. 2009.

[33] N. C. Giebink et al., "Intrinsic luminance loss in phosphorescent small-molecule organic light emitting devices due to bimolecular annihilation reactions," J. Appl. Phys., vol. 103, no. 4, p. 44509, Feb. 2008.

[34] H. Uoyama, K. Goushi, K. Shizu, H. Nomura, and C. Adachi, "Highly efficient organic light-emitting diodes from delayed fluorescence," Nature, vol. 492, no. 7428, pp. 234–238, Dec. 2012.

[35] H. Nakanotani et al., "High-efficiency organic light-emitting diodes with fluorescent emitters," Nat. Commun., vol. 5, May 2014.

[36] Q. Zhang, B. Li, S. Huang, H. Nomura, H. Tanaka, and C. Adachi, "Efficient blue organic light-emitting diodes employing thermally activated delayed fluorescence," Nat. Photonics, vol. 8, no. 4, pp. 326–332, Apr. 2014.

[37] D. P.-K. Tsang and C. Adachi, "Operational stability enhancement in organic light-emitting diodes with ultrathin Liq interlayers," Sci. Rep., vol. 6, p. 22463, Mar. 2016.

[38] S. Barth et al., "Electron mobility in tris(8-hydroxy-quinoline)aluminum thin films determined via transient electroluminescence from single- and multilayer organic light-emitting diodes," J. Appl. Phys., vol. 89, no. 7, pp. 3711–3719, Mar. 2001.

[39] M. A. Baldo, C. Adachi, and S. R. Forrest, "Transient analysis of organic electrophosphorescence. II. Transient analysis of triplet-triplet annihilation," Phys. Rev. B, vol. 62, no. 16, pp. 10967–10977, Oct. 2000.

[40] K.-H. Kim and J.-K. Song, "Technical evolution of liquid crystal displays," NPG Asia Mater., vol. 1, no. 1, pp. 29–36, Oct. 2009.

[41] M. A. Baldo, S. Lamansky, P. E. Burrows, M. E. Thompson, and S. R. Forrest, "Very high-efficiency green organic light-emitting devices based on electrophosphorescence," Appl. Phys. Lett., vol. 75, no. 1, pp. 4–6, Jul. 1999.

[42] J. Lee et al., "Deep blue phosphorescent organic light-emitting diodes with very high brightness and efficiency," Nat. Mater., vol. 15, no. 1, pp. 92–98, Jan. 2016.

[43] Z. B. Wang et al., "Highly simplified phosphorescent organic light emitting diode with >20% external quantum efficiency at >10,000 cd/m^2," Appl. Phys. Lett., vol. 98, no. 7, p. 73310, Feb. 2011.

[44] Y. Kawamura, K. Goushi, J. Brooks, J. J. Brown, H. Sasabe, and C. Adachi, "100% phosphorescence quantum efficiency of Ir(III) complexes in organic semiconductor films," Appl. Phys. Lett., vol. 86, no. 7, p. 71104, Feb. 2005.

[45] Y. Kawamura, J. Brooks, J. J. Brown, H. Sasabe, and C. Adachi, "Intermolecular Interaction and a Concentration-Quenching Mechanism of Phosphorescent Ir(III) Complexes in a Solid Film," Phys. Rev. Lett., vol. 96, no. 1, p. 17404, Jan. 2006.

[46] A. B. Chwang, R. C. Kwong, and J. J. Brown, "Graded mixed-layer organic light-emitting devices," Appl. Phys. Lett., vol. 80, no. 5, pp. 725–727, Jan. 2002.

[47] H.-H. Chou and C.-H. Cheng, “A Highly Efficient Universal Bipolar Host for Blue, Green, and Red Phosphorescent OLEDs,” Adv. Mater., vol. 22, no. 22, pp. 2468–2471, Jun. 2010.
[48] N. C. Erickson and R. J. Holmes, “Highly efficient, single-layer organic light-emitting devices based on a graded-composition emissive layer,” Appl. Phys. Lett., vol. 97, no. 8, p. 83308, Aug. 2010.
[49] W. Brütting, J. Frischeisen, T. D. Schmidt, B. J. Scholz, and C. Mayr, “Device efficiency of organic light-emitting diodes: Progress by improved light outcoupling,” Phys. Status Solidi A, vol. 210, no. 1, pp. 44–65, Jan. 2013.
[50] Y. Zhang, J. Lee, and S. R. Forrest, “Tenfold increase in the lifetime of blue phosphorescent organic light-emitting diodes,” Nat. Commun., vol. 5, Sep. 2014.
[51] K. Goushi, K. Yoshida, K. Sato, and C. Adachi, “Organic light-emitting diodes employing efficient reverse intersystem crossing for triplet-to-singlet state conversion,” Nat. Photonics, vol. 6, no. 4, pp. 253–258, Apr. 2012.
[52] N. C. Giebink and S. R. Forrest, “Quantum efficiency roll-off at high brightness in fluorescent and phosphorescent organic light emitting diodes,” Phys. Rev. B, vol. 77, no. 23, p. 235215, Jun. 2008.
[53] R. H. Fowler and L. Nordheim, “Electron Emission in Intense Electric Fields,” Proc. R. Soc. Lond. Math. Phys. Eng. Sci., vol. 119, no. 781, pp. 173–181, May 1928.
[54] O. W. Richardson, “Electron Emission from Metals as a Function of Temperature,” Phys. Rev., vol. 23, no. 2, pp. 153–155, Feb. 1924.
[55] W. Schottky, “Vereinfachte und erweiterte Theorie der Randschicht-gleichrichter,” Z. Für Phys., vol. 118, no. 9–10, pp. 539–592, Feb. 1942.
[56] R. L. Martin, J. D. Kress, I. H. Campbell, and D. L. Smith, “Molecular and solid-state properties of tris-(8-hydroxyquinolate)-aluminum,” Phys. Rev. B, vol. 61, no. 23, pp. 15804–15811, Jun. 2000.
[57] Y. N. Gartstein and E. M. Conwell, “High-field hopping mobility of polarons in disordered molecular solids. A Monte Carlo study,” Chem. Phys. Lett., vol. 217, no. 1, pp. 41–47, Jan. 1994.
[58] R. A. Marcus, “Chemical and Electrochemical Electron-Transfer Theory,” Annu. Rev. Phys. Chem., vol. 15, no. 1, pp. 155–196, 1964.
[59] M. A. Baldo and S. R. Forrest, “Interface-limited injection in amorphous organic semiconductors,” Phys. Rev. B, vol. 64, no. 8, p. 85201, Aug. 2001.
[60] P. W. M. Blom, M. J. M. de Jong, and J. J. M. Vleggaar, “Electron and hole transport in poly(p-phenylene vinylene) devices,” Appl. Phys. Lett., vol. 68, no. 23, pp. 3308–3310, Jun. 1996.
[61] P. Mark and W. Helfrich, “Space-Charge-Limited Currents in Organic Crystals,” J. Appl. Phys., vol. 33, no. 1, pp. 205–215, Jan. 1962.

[62] P. E. Burrows et al., “Relationship between electroluminescence and current transport in organic heterojunction light-emitting devices,” J. Appl. Phys., vol. 79, no. 10, pp. 7991–8006, May 1996.
[63] H. Yamamoto, H. Kasajima, W. Yokoyama, H. Sasabe, and C. Adachi, “Extremely-high-density carrier injection and transport over 12000A/cm2 into organic thin films,” Appl. Phys. Lett., vol. 86, no. 8, p. 83502, Feb. 2005.
[64] M. A. Lampert, “Simplified Theory of Space-Charge-Limited Currents in an Insulator with Traps,” Phys. Rev., vol. 103, no. 6, pp. 1648–1656, Sep. 1956.
[65] T. Matsushima and C. Adachi, “High-current Injection and Transport on Order of kA/cm2 in Organic Light-emitting Diodes Having Mixed Organic/Organic Heterojunction Interfaces,” Jpn. J. Appl. Phys., vol. 46, no. 9L, p. L861, Sep. 2007.
[66] W. Shockley and W. T. Read, “Statistics of the Recombinations of Holes and Electrons,” Phys. Rev., vol. 87, no. 5, pp. 835–842, Sep. 1952.
[67] G. A. H. Wetzelaer, M. Kuik, H. T. Nicolai, and P. W. M. Blom, “Trap-assisted and Langevin-type recombination in organic light-emitting diodes,” Phys. Rev. B, vol. 83, no. 16, p. 165204, Apr. 2011.
[68] A. Köhler and H. Bässler, “Triplet states in organic semiconductors,” Mater. Sci. Eng. R Rep., vol. 66, no. 4–6, pp. 71–109, Nov. 2009.
[69] S. Lamansky et al., “Synthesis and Characterization of Phosphorescent Cyclometalated Iridium Complexes,” Inorg. Chem., vol. 40, no. 7, pp. 1704–1711, Mar. 2001.
[70] R. Gómez-Bombarelli et al., “Design of efficient molecular organic light-emitting diodes by a high-throughput virtual screening and experimental approach,” Nat. Mater., vol. 15, no. 10, pp. 1120–1127, Oct. 2016.
[71] H. Yersin, A. F. Rausch, R. Czerwieniec, T. Hofbeck, and T. Fischer, “The triplet state of organo-transition metal compounds. Triplet harvesting and singlet harvesting for efficient OLEDs,” Coord. Chem. Rev., vol. 255, no. 21–22, pp. 2622–2652, Nov. 2011.
[72] J. Gierschner, J. Cornil, and H.-J. Egelhaaf, “Optical Bandgaps of π-Conjugated Organic Materials at the Polymer Limit: Experiment and Theory,” Adv. Mater., vol. 19, no. 2, pp. 173–191, Jan. 2007.
[73] E. Merzbacher, Quantum Mechanics. Wiley, 1998.
[74] S. Lamansky et al., “Highly Phosphorescent Bis-Cyclometalated Iridium Complexes: Synthesis, Photophysical Characterization, and Use in Organic Light Emitting Diodes,” J. Am. Chem. Soc., vol. 123, no. 18, pp. 4304–4312, May 2001.
[75] T. Fleetham, G. Li, and J. Li, “Phosphorescent Pt(II) and Pd(II) Complexes for Efficient, High-Color-Quality, and Stable OLEDs,” Adv. Mater., pp. 1–16, Nov. 2016.
[76] M. A. Baldo, M. E. Thompson, and S. R. Forrest, “High-efficiency fluorescent organic light-emitting devices using a phosphorescent sensitizer,” Nature, vol. 403, no. 6771, pp. 750–753, Feb. 2000.
[77] T. Főrster, “10th Spiers Memorial Lecture. Transfer mechanisms of electronic excitation,” Discuss. Faraday Soc., vol. 27, no. 0, pp. 7–17, Jan. 1959.

[78] D. L. Dexter, “A Theory of Sensitized Luminescence in Solids,” J. Chem. Phys., vol. 21, no. 5, pp. 836–850, May 1953.
[79] Y. Zhang and S. R. Forrest, “Triplet diffusion leads to triplet–triplet annihilation in organic phosphorescent emitters,” Chem. Phys. Lett., vol. 590, pp. 106–110, Dec. 2013.
[80] J. Frey et al., “Structure–property relationships based on Hammett constants in cyclometalated iridium(III) complexes: their application to the design of a fluorine-free FIrPic-like emitter,” Dalton Trans., vol. 43, no. 15, pp. 5667–5679, 2014.
[81] A. B. Tamayo et al., “Synthesis and Characterization of Facial and Meridional Tris-cyclometalated Iridium(III) Complexes,” J. Am. Chem. Soc., vol. 125, no. 24, pp. 7377–7387, Jun. 2003.
[82] J. Li et al., “Synthetic Control of Excited-State Properties in Cyclometalated Ir(III) Complexes Using Ancillary Ligands,” Inorg. Chem., vol. 44, no. 6, pp. 1713–1727, Mar. 2005.
[83] C. Adachi et al., “Endothermic energy transfer: A mechanism for generating very efficient high-energy phosphorescent emission in organic materials,” Appl. Phys. Lett., vol. 79, no. 13, pp. 2082–2084, Sep. 2001.
[84] Y. Seino, H. Sasabe, Y.-J. Pu, and J. Kido, “High-Performance Blue Phosphorescent OLEDs Using Energy Transfer from Exciplex,” Adv. Mater., vol. 26, no. 10, pp. 1612–1616, Mar. 2014.
[85] E. Baranoff and B. F. E. Curchod, “FIrpic: archetypal blue phosphorescent emitter for electroluminescence,” Dalton Trans., vol. 44, no. 18, pp. 8318–8329, 2015.
[86] R. J. Holmes, B. W. D’Andrade, S. R. Forrest, X. Ren, J. Li, and M. E. Thompson, “Efficient, deep-blue organic electrophosphorescence by guest charge trapping,” Appl. Phys. Lett., vol. 83, no. 18, pp. 3818–3820, Oct. 2003.
[87] V. Sivasubramaniam et al., “Fluorine cleavage of the light blue heteroleptic triplet emitter FIrpic,” J. Fluor. Chem., vol. 130, no. 7, pp. 640–649, Jul. 2009.
[88] P. S. Wagenknecht and P. C. Ford, “Metal centered ligand field excited states: Their roles in the design and performance of transition metal based photochemical molecular devices,” Coord. Chem. Rev., vol. 255, no. 5–6, pp. 591–616, Mar. 2011.
[89] T. Sajoto, P. I. Djurovich, A. B. Tamayo, J. Oxgaard, W. A. Goddard, and M. E. Thompson, “Temperature Dependence of Blue Phosphorescent Cyclometalated Ir(III) Complexes,” J. Am. Chem. Soc., vol. 131, no. 28, pp. 9813–9822, Jul. 2009.
[90] N. R. Council, Assessment of Advanced Solid-State Lighting. 2013.
[91] T. W. Dey and E. C. Letter, “Luminaire using a multilayer interference mirror,” US4161015 A, 10-Jul-1979.
[92] R. J. Saccomanno and I. B. Steiner, “Luminaires for artificial lighting,” 7195374, 27-Mar-2007.
[93] B. A. Jacobson, R. D. Gengelbach, N. W. M. JR, L. Roberts, and J. Perry, “Optical system for batwing distribution,” US20090225543 A1, 10-Sep-2009.

[94] M. Kröger, S. Hamwi, J. Meyer, T. Riedl, W. Kowalsky, and A. Kahn, "Role of the deep-lying electronic states of MoO3 in the enhancement of hole-injection in organic thin films," Appl. Phys. Lett., vol. 95, no. 12, p. 123301, Sep. 2009.

[95] J. Qiu, Z. B. Wang, M. G. Helander, and Z. H. Lu, "MoO_3 doped 4,4′-N,N′-dicarbazole-biphenyl for low voltage organic light emitting diodes," Appl. Phys. Lett., vol. 99, no. 15, p. 153305, Oct. 2011.

[96] N. Wang, J. D. Zimmerman, X. Tong, X. Xiao, J. Yu, and S. R. Forrest, "Snow cleaning of substrates increases yield of large-area organic photovoltaics," Appl. Phys. Lett., vol. 101, no. 13, p. 133901, Sep. 2012.

[97] S. r. Forrest, D. d. c. Bradley, and M. e. Thompson, "Measuring the Efficiency of Organic Light-Emitting Devices," Adv. Mater., vol. 15, no. 13, pp. 1043–1048, 2003.

[98] S. Choi, W. J. P. Jr, and B. Kippelen, "Area-scaling of organic solar cells," J. Appl. Phys., vol. 106, no. 5, p. 54507, Sep. 2009.

[99] C. Piliego, M. Mazzeo, M. Salerno, R. Cingolani, G. Gigli, and A. Moro, "Analysis and control of the active area scaling effect on white organic light emitting diodes towards lighting applications," Appl. Phys. Lett., vol. 89, no. 10, p. 103514, Sep. 2006.

[100] J. L. Lindsey, Applied Illumination Engineering. The Fairmont Press, Inc., 1997.

[101] S. Möller and S. R. Forrest, "Improved light out-coupling in organic light emitting diodes employing ordered microlens arrays," J. Appl. Phys., vol. 91, no. 5, pp. 3324–3327, Mar. 2002.

[102] S. Zhang, G. A. Turnbull, and I. D. W. Samuel, "Highly Directional Emission and Beam Steering from Organic Light-Emitting Diodes with a Substrate Diffractive Optical Element," Adv. Opt. Mater., pp. 343–347, 2014.

[103] V. Bulović, V. B. Khalfin, G. Gu, P. E. Burrows, D. Z. Garbuzov, and S. R. Forrest, "Weak microcavity effects in organic light-emitting devices," Phys. Rev. B, vol. 58, no. 7, pp. 3730–3740, Aug. 1998.

[104] R. Cok, "Organic polarized light emitting diode display with polarizer," US20050088084 A1, 28-Apr-2005.

[105] K. Celebi, T. D. Heidel, and M. A. Baldo, "Simplified calculation of dipole energy transport in a multilayer stack using dyadic Green's functions," Opt. Express, vol. 15, no. 4, pp. 1762–1772, Feb. 2007.

[106] T. Sajoto et al., "Blue and Near-UV Phosphorescence from Iridium Complexes with Cyclometalated Pyrazolyl or N-Heterocyclic Carbene Ligands," Inorg. Chem., vol. 44, no. 22, pp. 7992–8003, Oct. 2005.

[107] C. Schildknecht et al., "Novel deep-blue emitting phosphorescent emitter," 2005, vol. 5937, p. 59370E–59370E–9.

[108] M. N. Hopkinson, C. Richter, M. Schedler, and F. Glorius, "An overview of N-heterocyclic carbenes," Nature, vol. 510, no. 7506, pp. 485–496, Jun. 2014.

[109] C.-F. Chang et al., "Highly Efficient Blue-Emitting Iridium(III) Carbene Complexes and Phosphorescent OLEDs," Angew. Chem. Int. Ed., vol. 47, no. 24, pp. 4542–4545, 2008.

[110] Y.-C. Chiu et al., “En Route to High External Quantum Efficiency (~12%), Organic True-Blue-Light-Emitting Diodes Employing Novel Design of Iridium (III) Phosphors,” Adv. Mater., vol. 21, no. 21, pp. 2221–2225, Jun. 2009.

[111] H. Sasabe et al., “High-Efficiency Blue and White Organic Light-Emitting Devices Incorporating a Blue Iridium Carbene Complex,” Adv. Mater., vol. 22, no. 44, pp. 5003–5007, Nov. 2010.

[112] C.-H. Hsieh et al., “Design and Synthesis of Iridium Bis(carbene) Complexes for Efficient Blue Electrophosphorescence,” Chem. – Eur. J., vol. 17, no. 33, pp. 9180–9187, Aug. 2011.

[113] K.-Y. Lu et al., “Wide-Range Color Tuning of Iridium Biscarbene Complexes from Blue to Red by Different N^N Ligands: an Alternative Route for Adjusting the Emission Colors,” Adv. Mater., vol. 23, no. 42, pp. 4933–4937, Nov. 2011.

[114] T. Fleetham, Z. Wang, and J. Li, “Efficient deep blue electrophosphorescent devices based on platinum(II) bis(n-methyl-imidazolyl)benzene chloride,” Org. Electron., vol. 13, no. 8, pp. 1430–1435, Aug. 2012.

[115] S. Lee et al., “Deep-Blue Phosphorescence from Perfluoro Carbonyl-Substituted Iridium Complexes,” J. Am. Chem. Soc., vol. 135, no. 38, pp. 14321–14328, Sep. 2013.

[116] X.-C. Hang, T. Fleetham, E. Turner, J. Brooks, and J. Li, “Highly Efficient Blue-Emitting Cyclometalated Platinum(II) Complexes by Judicious Molecular Design,” Angew. Chem. Int. Ed., vol. 52, no. 26, pp. 6753–6756, Jun. 2013.

[117] T. Fleetham, G. Li, L. Wen, and J. Li, “Efficient ‘Pure’ Blue OLEDs Employing Tetradentate Pt Complexes with a Narrow Spectral Bandwidth,” Adv. Mater., vol. 26, no. 41, pp. 7116–7121, 2014.

[118] N. C. Erickson and R. J. Holmes, “Engineering Efficiency Roll-Off in Organic Light-Emitting Devices,” Adv. Funct. Mater., vol. 24, no. 38, pp. 6074–6080, Oct. 2014.

[119] M. S. Park and J. Y. Lee, “Indolo Acridine-Based Hole-Transport Materials for Phosphorescent OLEDs with Over 20% External Quantum Efficiency in Deep Blue and Green,” Chem. Mater., vol. 23, no. 19, pp. 4338–4343, Oct. 2011.

[120] R. J. Holmes et al., “Saturated deep blue organic electrophosphorescence using a fluorine-free emitter,” Appl. Phys. Lett., vol. 87, no. 24, p. 243507, Dec. 2005.

[121] J. C. Deaton, R. H. Young, J. R. Lenhard, M. Rajeswaran, and S. Huo, “Photophysical Properties of the Series fac- and mer-(1-Phenylisoquinolinato-N^$C^{2'}$)$_x$(2-phenylpyridinato-N^$C^{2'}$)$_{3-x}$Iridium(III) (x = 1−3),” Inorg. Chem., vol. 49, no. 20, pp. 9151–9161, Oct. 2010.

[122] A. B. Tamayo et al., “Synthesis and Characterization of Facial and Meridional Tris-cyclometalated Iridium(III) Complexes,” J. Am. Chem. Soc., vol. 125, no. 24, pp. 7377–7387, Jun. 2003.

[123] J. M. Lauerhaas, G. M. Credo, J. L. Heinrich, and M. J. Sailor, “Reversible luminescence quenching of porous silicon by solvents,” J. Am. Chem. Soc., vol. 114, no. 5, pp. 1911–1912, Feb. 1992.

[124] Y. You and W. Nam, "Photofunctional triplet excited states of cyclometalated Ir(III) complexes: beyond electroluminescence," Chem. Soc. Rev., vol. 41, no. 21, pp. 7061–7084, Oct. 2012.

[125] K. Tsuchiya, E. Ito, S. Yagai, A. Kitamura, and T. Karatsu, "Chirality in the Photochemical mer→fac Geometrical Isomerization of Tris(1-phenylpyrazolato,N,$C^{2'}$)iridium(III)," Eur. J. Inorg. Chem., vol. 2009, no. 14, pp. 2104–2109, May 2009.

[126] E. M. Kober, B. P. Sullivan, and T. J. Meyer, "Solvent dependence of metal-to-ligand charge-transfer transitions. Evidence for initial electron localization in MLCT excited states of 2,2'-bipyridine complexes of ruthenium(II) and osmium(II)," Inorg. Chem., vol. 23, no. 14, pp. 2098–2104, Jul. 1984.

[127] L. Xiao et al., "Recent Progresses on Materials for Electrophosphorescent Organic Light-Emitting Devices," Adv. Mater., vol. 23, no. 8, pp. 926–952, Feb. 2011.

[128] K. S. Yook and J. Y. Lee, "Organic Materials for Deep Blue Phosphorescent Organic Light-Emitting Diodes," Adv. Mater., vol. 24, no. 24, pp. 3169–3190, Jun. 2012.

[129] S. O. Jeon, S. E. Jang, H. S. Son, and J. Y. Lee, "External Quantum Efficiency Above 20% in Deep Blue Phosphorescent Organic Light-Emitting Diodes," Adv. Mater., vol. 23, no. 12, pp. 1436–1441, Mar. 2011.

[130] S. Reineke, K. Walzer, and K. Leo, "Triplet-exciton quenching in organic phosphorescent light-emitting diodes with Ir-based emitters," Phys. Rev. B, vol. 75, no. 12, p. 125328, Mar. 2007.

[131] S.-J. Su, E. Gonmori, H. Sasabe, and J. Kido, "Highly Efficient Organic Blue-and White-Light-Emitting Devices Having a Carrier- and Exciton-Confining Structure for Reduced Efficiency Roll-Off," Adv. Mater., vol. 20, no. 21, pp. 4189–4194, Nov. 2008.

[132] Y. Seino, H. Sasabe, Y.-J. Pu, and J. Kido, "High-Performance Blue Phosphorescent OLEDs Using Energy Transfer from Exciplex," Adv. Mater., vol. 26, no. 10, pp. 1612–1616, 2014.

[133] Q. Zhang, B. Li, S. Huang, H. Nomura, H. Tanaka, and C. Adachi, "Efficient blue organic light-emitting diodes employing thermally activated delayed fluorescence," Nat. Photonics, vol. advance online publication, Mar. 2014.

[134] C.-H. Yang et al., "Deep-Blue-Emitting Heteroleptic Iridium(III) Complexes Suited for Highly Efficient Phosphorescent OLEDs," Chem. Mater., vol. 24, no. 19, pp. 3684–3695, Oct. 2012.

[135] S. Reineke, G. Schwartz, K. Walzer, M. Falke, and K. Leo, "Highly phosphorescent organic mixed films: The effect of aggregation on triplet-triplet annihilation," Appl. Phys. Lett., vol. 94, no. 16, p. 163305, Apr. 2009.

[136] A. B. Padmaperuma, L. S. Sapochak, and P. E. Burrows, "New Charge Transporting Host Material for Short Wavelength Organic Electrophosphorescence: 2,7-Bis(diphenylphosphine oxide)-9,9-dimethylfluorene," Chem. Mater., vol. 18, no. 9, pp. 2389–2396, May 2006.

[137] P. Calcagno, B. M. Kariuki, S. J. Kitchin, J. M. A. Robinson, D. Philp, and K. D. M. Harris, "Understanding the Structural Properties of a Homologous Series of Bis-diphenylphosphine Oxides," Chem. – Eur. J., vol. 6, no. 13, pp. 2338–2349, Jul. 2000.
[138] P. Erk et al., "11.2: Efficient Deep Blue Triplet Emitters for OLEDs," SID Symp. Dig. Tech. Pap., vol. 37, no. 1, pp. 131–134, Jun. 2006.
[139] D. Y. Kondakov, J. R. Sandifer, C. W. Tang, and R. H. Young, "Nonradiative recombination centers and electrical aging of organic light-emitting diodes: Direct connection between accumulation of trapped charge and luminance loss," J. Appl. Phys., vol. 93, no. 2, pp. 1108–1119, Jan. 2003.
[140] N. C. Giebink, B. W. D'Andrade, M. S. Weaver, J. J. Brown, and S. R. Forrest, "Direct evidence for degradation of polaron excited states in organic light emitting diodes," J. Appl. Phys., vol. 105, no. 12, p. 124514, Jun. 2009.
[141] H. Kato and M. Baba, "Dynamics of Excited Molecules: Predissociation," Chem. Rev., vol. 95, no. 7, pp. 2311–2349, Nov. 1995.
[142] H. Yamamoto, J. Brooks, M. S. Weaver, J. J. Brown, T. Murakami, and H. Murata, "Improved initial drop in operational lifetime of blue phosphorescent organic light emitting device fabricated under ultra high vacuum condition," Appl. Phys. Lett., vol. 99, no. 3, p. 33301, Jul. 2011.
[143] H. Kanno, R. J. Holmes, Y. Sun, S. Kena-Cohen, and S. R. Forrest, "White Stacked Electrophosphorescent Organic Light-Emitting Devices Employing MoO3 as a Charge-Generation Layer," Adv. Mater., vol. 18, no. 3, pp. 339–342, Feb. 2006.
[144] Q. Wang and H. Aziz, "Degradation of Organic/Organic Interfaces in Organic Light-Emitting Devices due to Polaron–Exciton Interactions," ACS Appl. Mater. Interfaces, vol. 5, no. 17, pp. 8733–8739, Sep. 2013.
[145] S. J. Blanksby and G. B. Ellison, "Bond Dissociation Energies of Organic Molecules," Acc. Chem. Res., vol. 36, no. 4, pp. 255–263, Apr. 2003.
[146] S.-H. Hwang, Y.-K. Kim, C.-H. Lee, S.-J. Lee, S. Yang, and H.-Y. Kim, "Phenylcarbazole-based compound and organic electroluminescent device employing the same," US20060115680 A1, 01-Jun-2006.
[147] Y. Zhao, J. Chen, and D. Ma, "Ultrathin Nondoped Emissive Layers for Efficient and Simple Monochrome and White Organic Light-Emitting Diodes," ACS Appl. Mater. Interfaces, vol. 5, no. 3, pp. 965–971, Feb. 2013.
[148] N. C. Erickson and R. J. Holmes, "Investigating the Role of Emissive Layer Architecture on the Exciton Recombination Zone in Organic Light-Emitting Devices," Adv. Funct. Mater., vol. 23, no. 41, pp. 5190–5198, Nov. 2013.
[149] C. Coburn, J. Lee, and S. R. Forrest, "Charge Balance and Exciton Confinement in Phosphorescent Organic Light Emitting Diodes," Adv. Opt. Mater., vol. 4, no. 6, pp. 889–895, Jun. 2016.

[150] N. Matsusue, S. Ikame, Y. Suzuki, and H. Naito, “Charge carrier transport in an emissive layer of green electrophosphorescent devices,” Appl. Phys. Lett., vol. 85, no. 18, pp. 4046–4048, Nov. 2004.
[151] S.-B. Lee, T. Yasuda, M.-J. Yang, K. Fujita, and T. Tsutsui, “Charge Carrier Mobility in Vacuum-Sublimed Dye Films for Light-Emitting Diodes Studied by the Time-of-Flight Technique,” Mol. Cryst. Liq. Cryst., vol. 405, no. 1, pp. 67–73, Jan. 2003.
[152] S. A. Bagnich, A. Rudnick, P. Schroegel, P. Strohriegl, and A. Köhler, “Triplet energies and excimer formation in meta- and para-linked carbazolebiphenyl matrix materials,” Philos. Trans. R. Soc. Lond. Math. Phys. Eng. Sci., vol. 373, no. 2044, p. 20140446, Jun. 2015.
[153] D. Y. Kondakov, W. C. Lenhart, and W. F. Nichols, “Operational degradation of organic light-emitting diodes: Mechanism and identification of chemical products,” J. Appl. Phys., vol. 101, no. 2, p. 24512, Jan. 2007.
[154] V. I. Adamovich, M. S. Weaver, and B. W. D’Andrade, “Long lifetime phosphorescent organic light emitting device (OLED) structures,” US8866377 B2, 21-Oct-2014.
[155] R. C. Kwong et al., “High operational stability of electrophosphorescent devices,” Appl. Phys. Lett., vol. 81, no. 1, pp. 162–164, Jul. 2002.
[156] S. Schmidbauer, A. Hohenleutner, and B. König, “Chemical Degradation in Organic Light-Emitting Devices: Mechanisms and Implications for the Design of New Materials,” Adv. Mater., vol. 25, no. 15, pp. 2114–2129, Apr. 2013.
[157] S. C. Xia, R. C. Kwong, V. I. Adamovich, M. S. Weaver, and J. J. Brown, “OLED Device Operational Lifetime: Insights and Challenges,” in Reliability physics symposium, 2007. proceedings. 45th annual. ieee international, 2007, pp. 253–257.
[158] R. Meerheim, B. Lussem, and K. Leo, “Efficiency and Stability of p-i-n Type Organic Light Emitting Diodes for Display and Lighting Applications,” Proc. IEEE, vol. 97, no. 9, pp. 1606–1626, 2009.
[159] M. Furno, R. Meerheim, S. Hofmann, B. Lüssem, and K. Leo, “Efficiency and rate of spontaneous emission in organic electroluminescent devices,” Phys. Rev. B, vol. 85, no. 11, p. 115205, Mar. 2012.